Title
Bandgap Engineering and Doping of CdO

Author
Detert, Douglas Mark

Publication Date
2014

Bandgap Engineering and Doping of CdO

by

Douglas Mark Detert

A dissertation submitted in partial satisfaction of the
requirements for the degree of
Doctor of Philosophy

in

Engineering — Materials Science and Engineering

in the

Graduate Division

of the

University of California, Berkeley

Committee in charge:

Professor Oscar D. Dubón, Co-chair
Dr. Wladyslaw Walukiewicz, Co-chair
Professor Daryl Chrzan
Professor Vivek Subramanian

Spring 2014

Bandgap Engineering and Doping of CdO

Abstract

Bandgap Engineering and Doping of CdO
by
Douglas Mark Detert
Doctor of Philosophy in Engineering — Materials Science and Engineering
University of California, Berkeley
Professor Oscar D. Dubón, Co-chair
Dr. Wladyslaw Walukiewicz, Co-chair

The unique properties of metal-oxide semiconductors make them well suited to a variety of optoelectronic applications. Metal oxides comprise all industrially-relevant transparent conductors (TCs), and there is significant interest in their development as photovoltaic (PV) absorbers, light-emitting diodes, and electrodes in photoelectrochemical (PEC) devices. TCs are heavily-doped, wide-bandgap semiconductors that must simultaneously exhibit high conductivity and high optical transparency across (and beyond) the visible spectral range, but such materials face severe fundamental tradeoffs between transparency and conductivity that preclude the use of TCs in a number of applications that require infrared and near-infrared transparency. High-mobility TC materials such as CdO can acheive a better balance of transparency and conductivity, but their short-wavelength transparency is limited by a low intrinsic direct bandgap of 2.2 eV.

This dissertation explores how the properties of CdO can be tuned by bandgap engineering and doping and discusses their use in TC and photoelectrochemical applications. Alloys of the structurally-mismatched endpoint compounds CdO–ZnO have attracted considerable interest within the field of oxide bandgap engineering as they allow the bandgap of ZnO (3.3 eV) to be tuned across the visible range with the incorporation of Cd into hexagonal ZnO. Little is known about the properties of cubic alloys based on Zn in CdO, however.

The correlated structural, optical, and electrical properties of $Cd_xZn_{1-x}O$ thin film alloys ($0 < x < 1$) grown by pulsed, filtered cathodic arc deposition are presented here. Compositional trends in the intrinsic, carrier-free bandgaps of $Cd_xZn_{1-x}O$ alloys are determined by three complementary techniques: ion-irradiation-induced pinning of the Fermi level at the Fermi-level stabilization energy, X-ray photoelectron spectroscopy, and soft X-ray absorption and emission spectroscopy. The three techniques find consensus in explaining the origin of compositional trends in the optical-bandgap narrowing upon Cd incorporation in wurtzite ZnO and widening upon Zn incorporation in rocksalt CdO. The conduction band minimum is found to be stationary for both wurtzite and rocksalt alloys, and a significant upward rise of the valence band maximum accounts for the majority of these observed bandgap changes.

These band alignment details, combined with the unique optical and electrical properties of the two phase regimes, make $Cd_xZn_{1-x}O$ alloys attractive candidates for PEC water splitting applications. A proposed device structure of a $Cd_xZn_{1-x}O$-Si tandem PEC is presented.

Finally, the unique electrical properties and doping behavior of CdO are examined using simulations based on the amphoteric defect model. The calculated doping and mobility limits are compared with experimental values for Ga-doped CdO.

To my parents, Mark and Mary, for giving me the opportunity to succeed,

and to Liana, for her love and support.

Contents

List of Figures

List of Tables

List of Acronyms & Symbols

Acronyms

ADM	Amphoteric defect model
AZO	Aluminum-doped zinc oxide
CBM	Energy of conduction band minimum
DC	Direct current
EQE	External quantum efficiency
FCA	Free-carrier absorption
FWHM	Full-width at half-maximum
ITO	Tin-doped indium oxide
II-VI	Compound semiconductor composed of group II and VI elements
III-V	Compound semiconductor composed of group III and V elements
IR	Infrared
MOCVD	Metalorganic chemical vapor deposition
PEC	Photoelectrochemical (device)
PFCAD	Pulsed, filtered cathodic arc deposition
PL	Photoluminescence
PLD	Pulsed laser deposition
PV	Photovoltaic (device)
RBS	Rutherford backscattering spectrometry
RF	Radio-frequency
RS	Rocksalt phase
SXE	(Soft) X-ray emission spectroscopy
TC	Transparent conductor
TCO	Transparent conducting oxide
TEY	Total electron yield
TFY	Total fluorescence yield
VBM	Energy of conduction band maximum
VCA	Virtual crystal approximation
WZ	Wurtzite phase
XAS	(Soft) X-ray absorption spectroscopy
XPS	X-ray photoelectron spectroscopy

XRD	X-ray diffraction

Symbols

α	Energy-dependent optical absorption coefficient
α_0	Energy-independent optical absorption constant
a_B	Bohr radius
a_H	Bohr radius of hydrogen
b	Bowing parameter
β	Full-width half-maximum of X-ray diffraction peak (in radians)
Δ	Gaussian function width parameter
E_c	Energy above conduction band minimum
ΔE_{CBM}	Energy offset in conduction band minima
E_A	Electron affinity
E_b	Binding energy (XPS)
E_{BM}	Burstein-Moss shift
E_d	Donor energy level
E_F	Fermi level
E_f	Defect formation energy
E_{f_o}	Defect formation energy at $\mathrm{E_{FS}}$
$E_{f_{AA}}$	Formation energy of native acceptor-like point defects
$E_{f_{DD}}$	Formation energy of native donor-like point defects
E_{KE}	Kinetic energy (XPS)
E_{e-e}	Bandgap renormalization from electron-electron interactions
E_{FS}	Fermi stabilization energy
E_g	Carrier-free, intrinsic (direct) bandgap
E_g^{ind}	Indirect bandgap
E_g^{dir}	Direct bandgap
E_g^o	Burstein-Moss-corrected bandgap (uncorrected for renormalization or valence-band-dispersion effects)
E_g^{opt}	Apparent bandgap from optical absorption
$E_{\mathrm{ion}-e}$	Bandgap renormalization from ion-electron interactions
E_P	Interaction parameter (Kane's $k \cdot p$ model)
$E_{\mathrm{renorm.}}$	Bandgap renormalization energy
E_{vac}	Vacuum energy level
E_{vb}	Blueshift in optical absorption edge due to valence band dispersion away from Γ point
ϵ_0	Vacuum permittivity
ϵ_r	Static dielectric constant (relative, static permittivity)
ϵ_{inf}	High-frequency dielectric constant
$\hbar$	Planck constant
$h\nu$	Photon energy

k	Reciprocal space wavevector
k_F	Wavevector at the Fermi level
k_B	Boltzmann constant
λ	Photon wavelength
λ_F	Thomas Fermi screening parameter for bandgap renormalization
m_o	Free electron mass
m_e^*	Band-edge effective electron mass
m^*	Average effective mass of conduction electrons
μ	Electron mobility
μ_{AD}	Alloy-disorder-limited mobility
$\mu_{\mathrm{Acousticphon.}}$	(Deformation potential mode) acoustic phonon scattering-limited mobility
$\mu_{\mathrm{Opticalphon.}}$	Optical phonon-limited mobility
$\mu_{\mathrm{Piezoelectric}}$	(Piezoelectric-mode) acoustic phonon scattering-limited mobility
μ_{Total}	Total electron mobility
M_{Element}	Molar mass of element
N_i	Equivalent total number of singly ionized point defects
N_{Avogadro}	Avogadro's number
N_D	Number of acceptors from impurities
N_D	Number of donors from impurities
N_{AA}	Number of native acceptor-like point defects
N_{DD}	Number of native donor-like point defects
N_{s}	Number density of lattice sites in a crystal
n	Free electron concentration
Φ_{det}	Work function of XPS detector
Φ_s	Work function of sample
R_s	Sheet resistance (in $\Omega/\Box$)
$R(E)$	Reflectance as a function of photon energy E
$T(E)$	Transmittance as a function of photon energy E
ρ	Resistivity
ρ_{Material}	Density of material
τ	Scattering lifetime, crystallite size (X-ray diffraction)
θ	Compensation ratio
V_{CBM}	Alloy disorder (conduction band) potential term
ω_p	Plasma frequency
Ω	(Real space) unit cell volume
x	Fraction of cation substitution in a ternary alloy, e.g. $\mathrm{A}_x\mathrm{B}_{1-x}\mathrm{C}$
ξ_o,$\xi(E_F)$	Dopant activation factor, Fermi-level-dependent function

Acknowledgments

I have many people to thank for their support, encouragement, technical guidance, and friendship over the course of my graduate school career.

I wish to thank my advisor, Professor Oscar Dubón, whose genuine dedication to his students has helped me grow as a scientist and as a person over the last six-and-a-half years. Oscar's mentorship has been invaluable in helping me successfully navigate all aspects of graduate school.

As well, I am incredibly fortunate to have had the chance to work with Drs. Kin Man Yu and Wladek Walukiewicz of the Solar Energy Materials Research Group at LBL. I thank them for welcoming me into their group, inspiring me, mentoring me, and encouraging me to work efficiently and carefully to produce the work contained within this dissertation. Working with Kin and Wladek has been an extreme pleasure and I hope to always work in an environment as fun and engaging as that which they have fostered in their group. I would also like to acknowledge the other members of my committee, Professor Daryl Chrzan and Professor Vivek Subramanian, for their helpful comments during my preparation of this dissertation. As well, I would like to thank Professor Ron Gronsky for his many years of advice and mentorship.

I am indebted to Dr. Marie Mayer for her generous (and excellent) advice, encouragement, and enthusiasm. Thanks to Kyle Tom for his invaluable contributions over the past two years to my dissertation work. I would like to thank Professors Eugene Haller and Junqiao Wu and all of the Dubón, Haller, Wu, and Solar EMAT group members and visiting researchers with whom I have worked, including Dr. Joe Wofford, Dr. Rouin Farshchi, Dr. Peter Stone, Dr. Alejandro Levander, Dr. Derrick Speaks, Dr. Greg Brown, Alex Luce, Kevin Wang, Paul Rogge, Grant Buchowicz, Dr. Devesh Khanal, Dr. Holland Smith, Dr. Nate Miller, Dr. Rob Broesler, Dr. Karen Bustillo, Erin Ford, Jose Fonseca Vega, Maribel Jaquez, Chris Francis, Min Ting, Matt Beres, Dr. Lothar Reichertz, Stella Zhao, Patricia Yen, Dr. Guibin Chen, Laura Sobra, and Sylwia Grankowska. Thank you as well to my scientific collaborators outside the group, including Dr. Jonathan Denlinger, Dr. Sunnie Lim, Dr. Andre Anders, Dr. Corsin Battaglia. As well, I am grateful to Drs. Petra Specht and Christian Kisielowski for their support and mentorship of my masters work in electron microscopy. Thank you to David Hom for his administrative prowess, friendship, and support, and to Jeff Beeman for his technical wizardry and for being a good-humored office-neighbor.

I am thankful to all of my friends and to my family. My parents, Mark and Mary, have always fostered my love of learning, providing encouragement and emotional support every step of the way for as long as (and longer) than I can remember. Thank you to my sister, Laura, for sharing my sense of humor and for being a good friend.

And finally, thank you to Liana, my fiancée and partner of fourteen years, for her love and unwavering support.

Chapter 1

Introduction

1.1 Oxide semiconductors for energy applications: Motivation and overview

Historically, the development of oxide-based semiconductors for optoelectronic applications has lagged behind that of traditional III-V materials, which include III-arsenides, III-phosphides, and (more recently) III-nitrides [1]. As the field of research into the properties and processing of III-nitride-based materials has matured, it has paved the way for commercially successful technologies such as high-intensity blue and violet light-emitting diodes (LEDs), which complemented existing red- and green-light emitters to make a complete set of primary color LEDs for energy-efficient solid state lighting and laser diode applications [2]. It is also possible to tune the bandgap of III-V nitride materials themselves across the visible range by alloy engineering, offering the promise of complete-spectrum photovoltaics for solar energy harvesting. While interest in III-V materials has dominated compound semiconductor research, notable successes in the development of II-VI technologies include $\mathrm{Mg_xCd_{1\text{-}x}Te}$ infrared detectors [1, 3], ZnSe-based emitters [4] and CdTe-based PVs [5].

In recent years there has been a marked increase in the study of the properties, processing, and device application potential of II-VI oxides materials. The majority of this attention has centered on ZnO (E_g = 3.37 eV) thin films and nanostructures due to the high value of its exciton binding energy (60 meV, compared to 25 meV in GaN), which contributes to its excellent emission behavior and the prospect of room-temperture excitonic devices [6, 7, 8]. There are significant challenges to the development of oxide-based devices, however. Most importantly, the lack of reproducible *p*-type conductivity in ZnO increases the need to understand how its electronic structure, native defects, and unintentional impurities affect its electrical behavior. Secondly, there remains much to be learned about the basic properties of ZnO-based alloys—$\mathrm{Mg_xZn_{1\text{-}x}O}$ and $\mathrm{Cd_xZn_{1\text{-}x}O}$—that will likely serve as the foundational materials for bandgap engineering strategies to enable the operation of oxide optoelectronics over a broad spectrum of wavelengths [8]. Chapters 4 and 5 of this dissertation address this latter point, elucidating the properties of $\mathrm{Cd_xZn_{1\text{-}x}O}$ thin films over the full composition range and connecting this behavior with fundamental changes in their electronic structure.

In general, oxide-based semiconductors (including metal oxides that are not II-VIs) enable and have the potential to enable novel technologies beyond conventional optoelectronic applications discussed above. There has been significant progress in developing transparent thin-film-transistors based on amorphous metal oxides which may revolutionize display and flexible electronics technologies [9]. As will be explored in the following sections and throughout this dissertation, metal oxides are the only viable materials for transparent conductor applications and their electrochemical stability enables their use in potential photoelectrochemical (PEC) applications, including devices that use sunlight to split water to produce hydrogen fuel [10].

1.2 Transparent conductors

Transparent conductors (TCs) are a class of materials defined by their unique combination of optical and electrical properties: they exhibit both high electrical conductivity and good optical transparency across, and often beyond, the visible spectrum [11, 12, 13, 14, 15]. There are countless materials that satisfy only one of these criteria—most metals are good conductors and common materials such as glass, quartz, sapphire, poly(methyl methacrylate) are quite transparent in the visible spectrum—but there are astonishingly few materials which satisfy both criteria simultaneously. Making a metal transparent is nearly impossible[1], but in select cases it is possible to tune the electrical properties of wide-bandgap semiconductors—particularly oxide semiconductors—to realize conductivity that is good enough for device applications. Finding candidate materials that can achieve this combination of properties is so difficult that, in practice, there are very few industrially relevant TCOs, all with severe limitations that restrict their use to select applications.

TCs are used in a wide range of applications, from "low tech" oven door windows and freezer case window defrosters to more "high tech" examples where they serve as front electrodes for flat-panel displays and thin film photovoltaic (PV) devices, and smart window applications windows [11, 18]. The first widespread use of TCs was their application as glass coatings for airplane windows in WWII, which enabled window defrosting (via resistive heating) at high altitudes and, in turn, enabled bombing from great heights [11]. The recent surge in the manufacturing of handheld devices and the development of fully transparent electronics has sparked significant research interest in finding new, high-performance (and/or earth-abundant) TCO materials to meet this growing demand [11, 18].

The exact combination of conductivity and transparency that is required of a TC depends on the requirements of its specific intended application. While for some energy-related applications it is desirable to have TCs with high visible transparency and low infrared (IR) transparency, as in the case of thermally insulating windows, in other applications broadband visible and IR transparency is desired [11, 12, 13]. The latter case is true for many

---

[1] Except as a result of reduced dimensionality, as is the case with ultrathin metal films [16] or metal nanofiber mesh networks [17].

photovoltaic (PV) applications, where a TC that serves as top electrode should achieve low resistivity ($\rho < 10^{-4}\ \Omega\ \text{cm}^{-1}$) while maximizing its transparency for all photons with energies above the band gap [13, 19] of the absorber layer(s). In other cases, where thickness must be minimized, such as in the case of display applications, the conductivity is of paramount importance [11]. It is important to note that for many PV technologies, such as multijunction cells and Si, metal pattering must be used in place of TCOs altogether [20].

Transparent conducting oxides (TCOs) are a subset of TCs comprising semiconducting metal-oxides that have sufficient visible transparency (i.e. direct bandgap $E_g \sim 2-4$ eV) and low resistivity due to heavy doping. This doping, typically n-type, arises either unintentionally (as the result of native defects) or deliberately (through the addition of impurity atoms) [18]. Familiar examples of TCOs include a non-stoichiometric combination of In_2O_3 and SnO_2 (yielding “ITO”), as well as F-doped SnO_2 (“FTO”) and Al-doped ZnO (“AZO”) [13]. While these materials generally offer suitable resistivity and visible transparency for many applications, as will be discussed in the following sections they are limited in performance by fundamental tradeoffs in their electrical and optical properties.

Given that the field of candidate TCO materials is so small, it is logical to question what it is about metal oxides—and only a select few of them—that allows them to achieve this balance of transparency and conductivity. The transparency criteria is easy to achieve: metal oxides tend to have wide bandgaps and in their undoped form they tend to be transparent to near-IR, IR, and visible light up to the bandgap energy. What sets some metal oxides apart from their peers, however, is their ability to be heavily doped (beyond 1×10^{21} cm^{-3}, up to several at.%) and their moderate electron mobilities even in the presence of high numbers of ionized impurities and grain boundaries [21]. The origin of their excellent doping behavior will be explained in Section 2.1.1 and further explored (for the specific case of doped CdO) in Chapter 7.

Although there is significant interest in other, non-oxide TCs (including metal nanowire mesh films [22], carbon nanotube films [23], and graphene [24] with low resistivities), the sheet resistance

$$R_s = \rho/t \text{ (in } \Omega/\square), \tag{1.1}$$

(where t is the thickness of a uniform film) values of these ultrathin materials make them unsuitable for use in most large-area devices. Nonetheless, given the strong propensity for most oxide-based TCs to exhibit n-type conductivity, non-oxide semiconductors may hold the key to developing p-type TCs. Such is the case with carbon-based TCs such as single-walled carbon nanotube films, which have been shown to exhibit p-type transport and modest sheet resistance ($R_s = 30\ \Omega/\square$) even when non-maximally doped [25]. The conductivity of other, oxide-based, p-type TCs such as $CuAlO_2$ [26] and NiO [27] is limited by their low hole mobilities and low doping limits. The challenge of achieving p-type TCOs is rooted in the more general challenge of engineering p-type conductivity in oxide materials as a whole, which remains a critical hurdle in the development of oxide-based electronics [28].

1.3 Balancing conductivity and transparency in TCOs: Fundamental tradeoffs

As noted in the previous section, the dearth of good TCOs results from the difficult engineering challenge of creating materials that simultaneously exhibit good transparency and conductivity. The remainder of this chapter will focus on explaining this problem from the point of view of the interdependency of the fundamental electrical and optical processes in semiconductor materials.

1.3.1 Conductivity

Historically, the primary challenge in increasing the performance of semiconductor TCOs has centered on increasing the conductivity of wide-bandgap semiconductors. The conductivity (σ) of a degenerately doped n-type semiconductor is given by

$$\sigma \approx ne\mu \tag{1.2}$$

where n is the concentration of conduction electrons (in cm^{-3}), e is the electron charge, and μ is the electron drift mobility (in cm^2/Vs). The contribution to the total conductivity due to holes can be ignored, given the extremely low concentration of free holes in heavily-doped n-type materials [29]. The total ρ resistivity is defined as $\rho = 1/\sigma$.

Electron mobility in TCOs

The total electron mobility is given by

$$\mu = \frac{e\tau_s}{m^*} \tag{1.3}$$

where τ_s is the effective scattering lifetime and m^* is the average effective mass of the conduction electrons. The effective scattering lifetime is the combined result[2] of multiple scattering mechanisms–scattering by phonons, by neutral and charged point defects, and by extended structural defects such as grain boundaries and dislocations. In general, strategies to enhance the mobility of materials therefore involve minimizing possible sources of scattering. Chemical and structural imperfections alike can be reduced by optimizing growth parameters to create materials with fewer or more benign defects [29]. However, increasing the conductivity by improving μ is not straightforward and practically very difficult. Improvements in materials quality are often difficult to achieve within the limitations of commonly-used and industrially-relevant growth techniques, and an improvement in μ is, by itself, not sufficient to achieve the degree of conductivity needed for TCO applications. It has been shown

---

[2] Conventionally, the reciprocal of the total scattering lifetime (and thus total mobility limit) is commonly found by adding the reciprocal individual lifetimes, a technique known as Matthiessen's rule.

that high-mobility (440 cm^2/Vs) transport is possible in ZnO thin films grown by epitaxial methods with post-growth annealing at temperatures near 1000° C, but this processing also reduces the electron concentration to $n \sim 10^{16}$ cm^{-3} [30]. Manufacturing processes for display, window, and PV applications often place strict limits on the TCO deposition temperature, however, further limiting the available parameter space in which μ can be optimized. For all TCO processing methods, the maximum conductivity will be achieved by optimizing the growth parameters and post-deposition thermal treatment to enhance structural quality, choosing appropriate dopants, and controlling the (unintentional) impurity content in the films [21]. An excellent review of the conductivity mechanisms in TCO materials is given in the article by King and Veal [31].

As a result of the processing constraints mentioned above, TCO materials typically exhibit polycrystalline microsctructures with grain sizes < 100 nm. Despite the presence of a high degree of local and extended structural disorder, electronic conduction in TCO materials is not chiefly limited by these defects except at low doping levels. Scattering from grain boundaries in lightly doped, polycrystalline semiconductors is typically modeled such that defects along internal surfaces introduce regions of charge depletion near the grain boundaries. The trapping of charges at these defects gives rise to potential barriers for conduction electrons which must be overcome by thermionic emission or by tunneling [32]. In heavily doped TCOs, however, the carrier lifetime—and thus total carrier mobility—is limited by the scattering of electrons from ionized impurities and optical phonons and not by grain boundaries [33]. Several mechanisms contribute to this behavior. First, ionized impurities—either from native defects or intentional dopants—are present in such great numbers that Coulombic scattering from these defects gives rise to a mean free path of electrons that is much smaller (typically a few nanometers) than the diameter of the grains [34]. Second, the Fermi level in heavily doped samples is higher[3] than the barriers introduced by grain boundaries, although the threshold concentration for this effect depends on the specific defect chemistry at grain boundaries for different materials. For example, for ITO the threshold concentration above which grain boundary scattering is no longer dominant has been observed to be $n \sim 10^{19}\,\text{cm}^{-3}$ while for ZnO this transition occurs at $n \sim 3 \times 10^{20}\,\text{cm}^{-3}$ [35, 36]. In transparent electronics applications where maximal conductivity is not desired, grain boundary scattering mechanisms can play a significant role.

The relative insensitivity of the conductivity of TCO materials to structural disorder is also a consequence of the nature of the conduction bands of common TCOs (such as In_2O_3, although not ZnO), which are derived primarily from s-states of octahedrally-coordinated metal cations [37, 38]. Even when there is moderate structural disorder, good conductivity can persist as long as these cation octahedra form a continuous network of shared edges. As well, the spherical symmetry of these s states facilitates the formation of these slightly disordered networks. Such effects also explain why it is possible to create amorphous TCOs with moderate conductivity [37, 38].

---

[3] Using ZnO as an example, electron concentrations of 10^{20} to $10^{21}\,\text{cm}^{-3}$ give rise to Fermi levels of $\sim 300\,\text{meV}$ to $1.3\,\text{eV}$.

Doping of TCOs

A perfectly stoichiometric, intrinsic semiconductor with a band gap suitable for TCO applications will have poor conductivity because the only electrons available for conduction are those that are thermally promoted across the bandgap. In order to increase the conductivity of the material, it is necessary to increase the number of charge carriers, n, by doping. In TCOs, this doping is typically achieved by the (often) unintentional creation of native point defects (generally in the form of anion vacancies, although there is ample evidence that the role of such defects is not always straightforward [31]) and by the intentional addition of impurities. A simple model for unintentional doping by oxygen vacancies is given (using Kröger-Vink notation) by the defect reaction [37, 39]

$$\mathrm{O}_{\mathrm{O}}^{\mathrm{x}} \Longleftrightarrow \frac{1}{2}\mathrm{O}_2(\mathrm{g}) + \mathrm{V}_{\mathrm{O}}^{\bullet\bullet} + 2e'. \tag{1.4}$$

The doubly-charged vacancy site will contribute strongly to ionized impurity scattering, the strength of which depends on the square of the charge. As noted by Mason et al. [39], cation interstitials would also serve as donors in the case of rocksalt oxides (such as CdO), although they are unlikely to be prevalent. As will be discussed in Section 2.1.1 this tendency for native point defects to behave as donors is in itself a good indication that it will tolerate a high degree of intentional n-type doping.

Figure 1.1, modeled after Ref. [40], presents a historical overview of the resistivity of industrially-relevant TCOs. The decreasing resistivity for each major family of TCOs (SnO_2, In_2O_3, ZnO, and most recently, CdO) has come about by optimizing the doping and growth parameters of the materials, and only recently have resistivities below $10^{-5}\ \Omega\,\mathrm{cm}^{-1}$ been consistently reported, a result of the emerging research interest in doped CdO films [41, 42, 43, 44, 19].

Typical doping strategies for TCOs involve aliovalent substitution of both cations (e.g. Sn in In_2O_3) and anions (e.g. F in SnO_2) [45]. The role and relative importance of hydrogen as a shallow donor in many TCOs is still the subject of much investigation and debate, although one hypothesis is that in certain materials, such as ITO, hydrogen contamination can account for the majority of n-type behavior. Because controlling hydrogen contamination in materials is experimentally quite difficult, the strongest evidence in support of such claims comes from electronic structure calculations [46, 47, 31].

Substitutional incorporation of impurities such as Al in ZnO and Sn in In_2O_3 can modulate the conductivity over several orders of magnitude, but due to the low electron mobilities commonly seen in the typical TCOs (AZO, ITO: $\mu \sim 50\ \mathrm{cm}^2/\mathrm{Vs}$), heavy doping is required. Electron concentrations of $n = 1 \times 10^{21}\ \mathrm{cm}^{-3}$ are required to fulfill a maximum resistivity requirement of $\rho < 10^{-4}\Omega\ \mathrm{cm}^{-1}$.

At high doping levels electrically active, native point defects are predominately acceptor-like in nature and heavily compensate any additional intentional dopants, limiting the maximum value of n. This behavior ultimately determines the “doping limit” of TCOs. These compensating defects similarly decrease the total mobility μ through ionized impurity scattering, as this contribution depends on the total number of (both positive and negative)

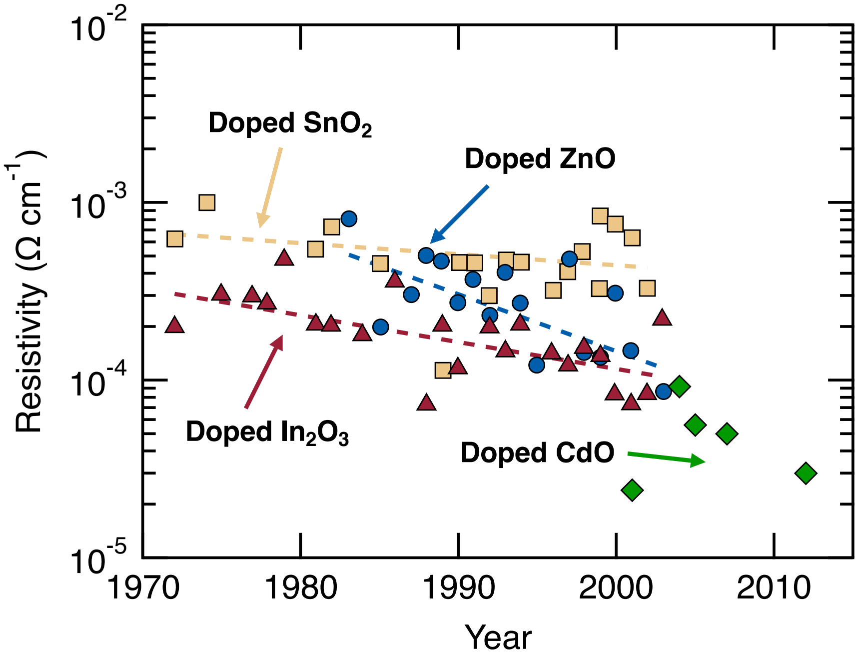

Figure 1.1: Resistivity of TCOs over time, 1970-present. Figure modeled after Ref. [40], with additional data for CdO from Refs. [19, 41, 42, 43, 44].

ionized scattering centers by

$$\mu_{\text{ion. imp.}} \propto \frac{1}{N_i}. \tag{1.5}$$

As will be explored in depth in Chapter 7, in the case of CdO the interplay between native defects and intentional doping is not straightforward, and for certain ranges of doping concentrations it is possible to reduce the effective number of ionized centers by doping with impurity elements.

1.3.2 Optical processes in TCOs affecting transparency

The presence of a large number of free carriers, along with a correspondingly large (or larger) concentration of ionized scattering centers, has three major effects on the transparency of a semiconductor: at short wavelengths (high-energies) the transparency is enhanced by a blueshift in the absorption edge due to carrier filling of the conduction band, known as the Burstein-Moss effect [48, 49]; at long wavelengths (low energies) the infrared (IR) and near-IR transparency is degraded by two mechanisms, plasma reflection and free carrier absorption. Each of these effects is explored in more detail in the following sections and illustrated in Figure 1.2.

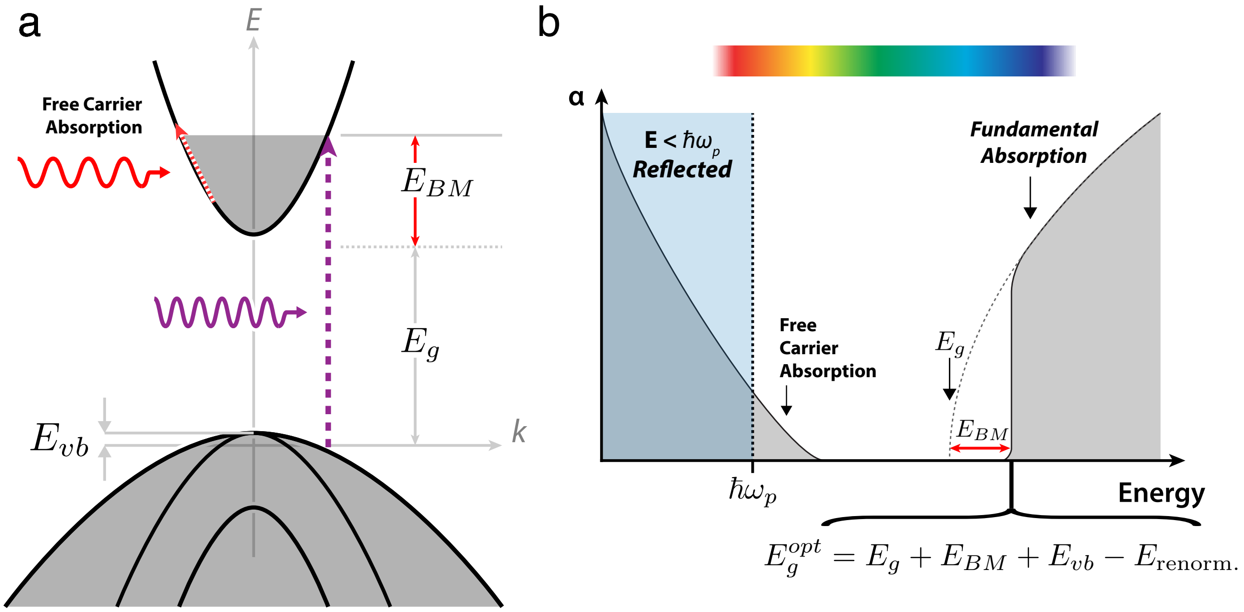

Figure 1.2: Optical processes in heavily doped semiconductors affecting transparency. The effects of free carriers are illustrated in (a) the bandstructure and (b) the absorption spectrum as a function of energy for a heavily-doped, direct-bandgap semiconductor or TCO. Carriers induce blue shifts in the direct-bandgap absorption edge by two processes. Carrier filling of the conduction band (known as the Burstein-Moss effect, indicated by E_{BM}) increases the energy of the lowest unoccupied states, and since direct transitions no longer occur at the Γ point (where $k = 0$), the dispersion of the valence band (in typical semiconductors) increases the energy of the transition by E_{vb}.

The Burstein-Moss shift

The short-wavelength (high energy) transparency limit for TCOs is determined not only by the fundamental bandgap of the semiconductor, as would be expected for any semiconductor material, but also by the number of electrons in its conduction band. At high electron concentrations (typically $n > 10^{19}$ cm^{-3}), carrier-filling of the conduction band results in a blue shift in the absorption edge, as the lowest unoccupied conduction band states are no longer found at the band edge but are instead shifted by the value of the Fermi level with respect to the conduction band minimum (CBM). The short-wavelength (high energy) transparency is therefore enhanced by this filling, known as the Burstein-Moss effect [48, 49].

The Fermi level for non-degenerately doped semiconductors lies in the band gap, but for heavily doped n-type materials, the Fermi level moves toward and eventually into the conduction band. In this state the semiconductor is considered to be "degenerately" doped. The Burstein-Moss shift in the absorption edge E_{BM} is calculated as the Fermi level E_F that results from a carrier concentration n and can be found by the Fermi integral over the conduction band states

$$n(E_F) = \frac{1}{3\pi^2} \int_0^\infty \frac{\exp\left(z - \frac{E_F}{k_B T}\right)}{\left[1 + \exp\left(z - \frac{E_F}{k_B T}\right)\right]^2} k^3(z)\, dz, \tag{1.6}$$

where $z = E/k_B T$ is the reduced energy with respect to the conduction band minimum ($E \equiv 0$) and $k(z)$ is found by solving the conduction band dispersion relation $E(k)$ for $k(E)$ [50, 51, 52]. Equation 1.6 is greatly simplified for the common case of degenerately-doped semiconductors, where

$$n(E_F) = \frac{1}{3\pi^2} k_F^3, \tag{1.7}$$

and even further for materials whose band edges have simple parabolic dispersion relations following

$$E_F(k) = \frac{\hbar^2 k_F^2}{2m_e^*}, \tag{1.8}$$

such that solving for k_F, substituting Equation 1.8 into 1.7, and solving for E_F yields the familiar result [53]

$$E_F = \frac{\hbar^2}{2m_e^*}(3\pi^2 n)^{2/3}. \tag{1.9}$$

As will be seen in Section 2.1.2, however, for *nonparabolic*-band semiconductors such as CdO any many other TCOs such as SnO_2 the full integral expression in Equation 1.6 must be used to calculate band filling [54].

In Figure 1.2 the carrier-shifted absorption edge E_g^{opt} seen in optical absorption experiments is

$$E_g^{opt} = E_g + E_{BM} + E_{vb} - E_{\text{renorm.}} \tag{1.10}$$

and includes additional factors of smaller total magnitude, including a slight blueshift E_{VB} due to the dispersion of the valence band and off-Γ-point absorption (in most TCOs, but not CdO, as discussed in Section 2.1.2) and a slight redshift due to bandgap renormalization effects from electron-electron and electron-ion interactions (not shown, but discussed in detail in Section 4.5.1 and Refs. [50, 51, 52]). Experimentally, it is possible to determine the intrinsic bandgap E_g of TCOs from optical absorption experiments given the electron concentration, provided sufficient knowledge of the band structure and other materials parameters. These procedures are discussed in greater detail in Sections 4.5.1 and A.4.

In contrast to the free-carrier effects discussed in the following sections, the Burstein-Moss shift is not a tradeoff between conductivity and transparency but rather a uniquely synergistic effect and one that will prove critically important for materials such as CdO (presented in more detail in Section 2.1), where carrier filling ($> 10^{21}$ cm^{-3}) can increase the absorption edge by nearly 1 eV relative to the intrinsic gap of ∼2.2 eV [19].

Plasma reflection

Plasma reflection arises from the collective oscillation of free charge carriers in response to electromagnetic waves. This light-matter interaction induces fluctuations in charge density around fixed ion cores and in all conductive materials is sensitive to the total number of electrons as well as their effective mass. The plasma edge serves as the long-wavelength (low energy) limit to the transparency in a TCO and is indicated in Figure 1.2 by the shaded area at low energy on the absorption plot. The energy of this edge is defined in terms of the plasma frequency ω_p such that photons below $E = \hbar\omega_p$ are reflected from the film surface. According to the Drude model of free electrons (which can be applied to TCOs given their high doping levels) for a semiconductor with electron concentration n this frequency is given by

$$\omega_p = \sqrt{\frac{ne^2}{\epsilon_0 \epsilon_\infty m^*}} \tag{1.11}$$

where ϵ_0 is the vacuum permittivity and ϵ_∞ is the high-frequency dielectric constant, and m^* is the effective mass of conduction electrons in the material [55]. Using this analysis, it is possible to estimate the electron concentration and effective mass from optical absorption spectroscopy. Examples of this analysis, along with a discussion of its assumptions, can be found in Refs. [56, 55, 57]

For metals[4] (where $n > 10^{22}$ cm^{-3}) this energy lies in the UV and thus reflects visible light. A typical value of $\hbar\omega_p$ for TCOs such as AZO and ITO (with $n \sim 10^{21}$ cm^{-3}) is around 1 eV [19] [56]. Plasma reflection, along with free-carrier absorption (discussed in the next section), ultimately prevents the use of TCOs in PV technologies that rely on low-gap absorbers (including crystalline Si).

Free carrier absorption

As illustrated in Figure 1.2, indirect transitions of free electrons within the conduction band, known as free carrier absorption (FCA), significantly degrade the transparency, particularly in the near-IR and long-wavelength visible spectrum [59, 60, 61]. The momentum change required for these indirect transitions is supplied by scattering from ionized impurities and optical phonons—the same scattering mechanisms that limit electrical transport. For this reason, the free carrier absorption coefficient is inversely proportional to the mobility μ and, by Equation 1.5, directly proportional to the total number of ionized impurities N_i. For TCOs, where $n \sim 10^{20} - 10^{21}$ cm^{-3}, both optical phonon scattering and ionized impurity scattering contribute to the overall FCA coefficient, although at the higher end of this range of doping the behavior is dominated by ionized impurity scattering [19]. For p-type TCOs, FCA will be enhanced by the typically high density of states in the valence band, further limiting their performance.

---

[4] Copper and gold also have strong interband transitions in the visible spectrum, further affecting their optical properties [58].

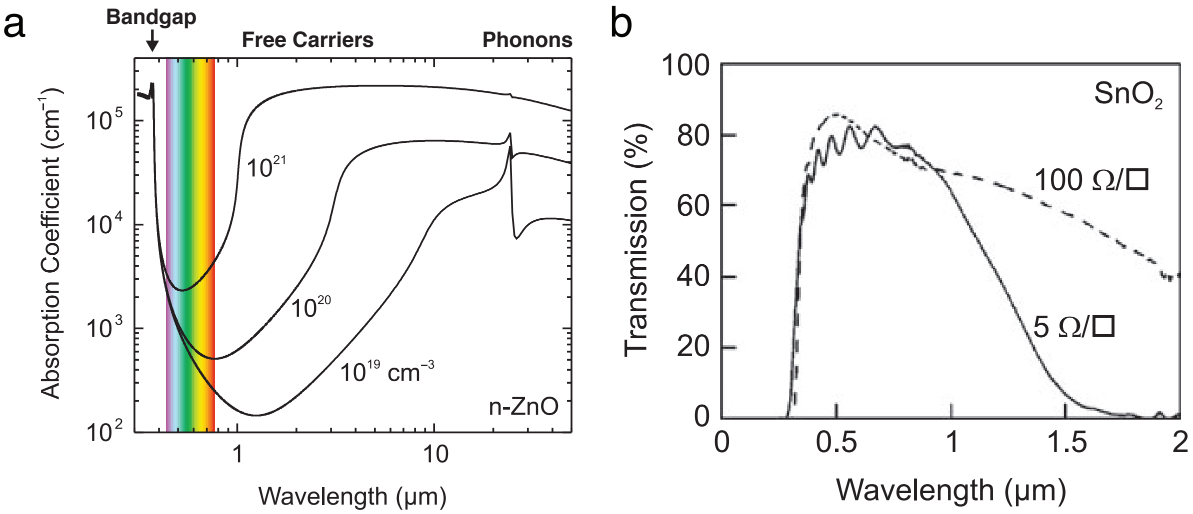

Figure 1.3: Examples of transparency-limiting effects in TCOs, adapted from Grundmann [15]. (a) Increased doping leads to a dramatic increase in the absorption in the visible spectrum and at longer wavelengths. Beyond $\lambda = 10$ μm, phonon-related absorption processes contribute to the absorption spectrum. (b) The tradeoff between conductivity (shown here in terms of different values of R_s) and transparency is evident at long wavelengths for SnO_2. Free carrier effects limit the transparency at long wavelengths ($\lambda > 1$ eV). (Original source for (b) is Ref. [45].)

The overall effects of free carrier absorption can be seen in Figure 1.3a, where the total absorption coefficient for Al-doped ZnO is modeled for three different carrier concentrations, $10^{19} - 10^{21}$ cm^{-3}. The additional transparency-limiting effect of the plasma edge is independent of the absorption processes and therefore does not factor into this figure. In Figure 1.3b, the transmission spectra of doped SnO_2 films with different sheet resistances reveals the combined effects of free carrier absorption and plasma reflection.

In both the plasma reflection and FCA processes, a large electron concentration n contributes to degraded IR and near-IR transparency. Given that all commonly-used TCOs require high n due to the limited mobilities of their base materials, they are not suitable for any application that demands broad-spectrum transparency, including single junction PVs with low-gap absorber layers, such as Si (1.1 eV) or multijunction cells that include a low-gap layer such as Ge (0.6 eV). If transparency is required, current collection is achieved by placing opaque, metal busbars on the top surface of the cell to improve conductivity, which in turn limits device efficiency [20]. Because of this fundamental tradeoff between electrical conductivity and IR optical transparency, these applications will require TCOs with higher mobiilties. CdO, discussed in detail in Chapter 2 is one such high-μ material that could be used as the basis for broad-spectrum TCOs, but further work is necessary to see if its moderately low bandgap of only ~ 2.2 eV can be tuned to provide better visible-and UV-spectrum transparency.

1.4 This dissertation

The remainder of this document is organized as follows: Chapter 2 provides an overview of the materials properties of CdO, a candidate material for high-mobility TCOs; a discussion of previous investigations related to bandgap engineering of pseudobinary alloys within the CdO-MgO-ZnO system; and an overview of the amphoteric defect model, a critical framework for understanding the electrical behavior of native defects in the materials investigated in this dissertation. Chapter 3 describes the plasma deposition method used to synthesize the thin film $Cd_xZn_{1-x}O$ alloys investigated in this work and provides results for the basic compositional and thickness analysis of the films. The correlated structural, electrical, and optical properties of $Cd_xZn_{1-x}O$ are characterized and reported in Chapter 4 and the compositional trends in the intrinsic, carrier-free bandgaps of the alloys are determined. In Chapter 5 the natural band alignment of $Cd_xZn_{1-x}O$ alloys is investigated by three complementary techniques, revealing the origin of the bandgap trends in terms of the independent movement of the conduction and valence bands with alloy content. Chapter 6 discusses the implications of these band alignment results with respect to the design of a novel $Cd_xZn_{1-x}O$-based photoelectrochemical device for water splitting. In Chapter 7, calculations based on the amphoteric defect model are used to model the interplay between native defects and intentional impurity dopants in Ga- and In-doped CdO, elucidating the connection between doping and mobility.

Chapter 2

Background

2.1 CdO: A high mobility transparent conductor

CdO was the earliest known example of a TCO, as its conductive properties were first noted by Badeker in 1907 [62]. Its utility, however, was eclipsed by other, less toxic materials, including ITO, FTO, and AZO, which were sufficient to meet the application demands of TCOs during the 20th century. The emerging need for high mobility TCOs in PV and other applications, however, requires new materials that can achieve an overall better compromise between transparency and conductivity, and CdO has been identified as a suitable candidate [19, 41, 42, 51, 63, 64]. After more than a decade of renewed interest in CdO there is much that is now known about its fundamental electrical and optical properties. The significant challenge that now must be overcome is to learn how its basic electrical and optical properties can be tuned, through doping and bandgap engineering, to produce materials tailored to suit specific applications.

This chapter offers an overview of the unusual properties of CdO, starting with a brief primer (Section 2.1.1) on the amphoteric defect model (ADM)—an essential framework needed to understand the electrical behavior of materials such as CdO and the basis of the irradiation experiments described in Section 5.2. Subsequent sections summarize the previous investigations of the band structure of CdO (Section 2.1.2) and its electrical and optical properties (Section 2.1.3). Finally, as a prelude to the experimental work and analysis presented in Chapters 4, 5, and 6, Section 2.2 introduces the concept of bandgap engineering and Section 2.3 presents a summary of previous work on CdO–ZnO–MgO pseudobinary alloys.

2.1.1 Unintentional conductivity in CdO: Native defects & the amphoteric defect model

As will be presented in more detail in Section 2.1.3 and as is generally the case with TCO materials, as-grown, nominally undoped thin films of CdO exhibit unintentional *n*-type conductivity, with typical electron concentrations above $\sim 10^{20}$ cm^{-3}. The origin of this behavior is well explained by the amphoteric defect model (ADM) developed by Walukiewicz [65, 66]. A straightforward but powerful theory, the ADM concept relates the electrical behavior of native point defects in a semiconductor to the natural band offsets of the host material [65, 66].

The central principle of the ADM framework is that the formation energies of electrically active native point defects in a semiconductor depend on the position of its Fermi level with respect to a universal stabilization energy E_{FS} that is common to all semiconductors. For a given temperature, the equilibrium concentration c of a given defect depends on its formation energy E_f such that the

$$c = N_{\mathrm{sites}} \exp\left(\frac{-E_f}{k_B T}\right). \tag{2.1}$$

If the Fermi level E_F is below E_{FS}, the formation of native donors will be favored, causing E_F to rise closer to E_{FS}; if E_F is above E_{FS}, native acceptors will be favored, reducing E_F. In other words, if E_F is out of equilibrium with E_{FS} the formation of compensating native defects that move E_F into alignment with E_{FS} will be favored. By extension, if intentional dopants are added to move the Fermi level the corresponding formation energy of compensating defect species will be reduced. This behavior leads to the ultimate doping limits in a semiconductor material [67]. The case of doping limits in CdO will be explored using this framework in Chapter 7.

The utility of this model stems from the observation that E_{FS} is not dependent on the band structure of a given material, but rather is universal to all semiconductors and located ~ 4.9 eV below the vacuum level with respect to the vacuum energy E_{vac}. The universality of E_{FS} makes it a convenient reference point for the alignment of the band edges of different semiconductors. In Appendix A.1, these band alignments are compiled for a wide range of oxide and non-oxide semiconductors.

Figure 2.1 provides an overview of the ADM and illustrates the difference between the expected native defect behavior of conventional semiconductor and a metal oxide semiconductor like CdO. In the case of a typical semiconductor, the band offsets of which are shown in Figure 2.1a, E_{FS} falls within the bandgap. The formation energies for two native defects—one donorlike and one acceptorlike—for this conventional semiconductor are plotted in Figure 2.1b. The slope of the formation energy line for each defect is proportional to its charge state. This two-defect-species model is a simplification of a real system, where similar defects and defect complexes of other charge states (and thus slopes) will add complexity to the picture. The maximum point, where defect behavior shifts from donorlike to acceptorlike, is the position of E_{FS}. In this way E_{FS} can be thought of as the average energy of native defects, and is sometimes referred to as the "Charge Neutrality Level." In this conventional case, E_F would be stabilized in the middle of the bandgap. Provided that the appropriate dopants can be found, then, this material could be doped both n-type and p-type, although its doping limit for either type would be relatively low. In the case of a typical metal oxide semiconductor, E_{FS} lies near or above the conduction band minimum (CBM) and the system

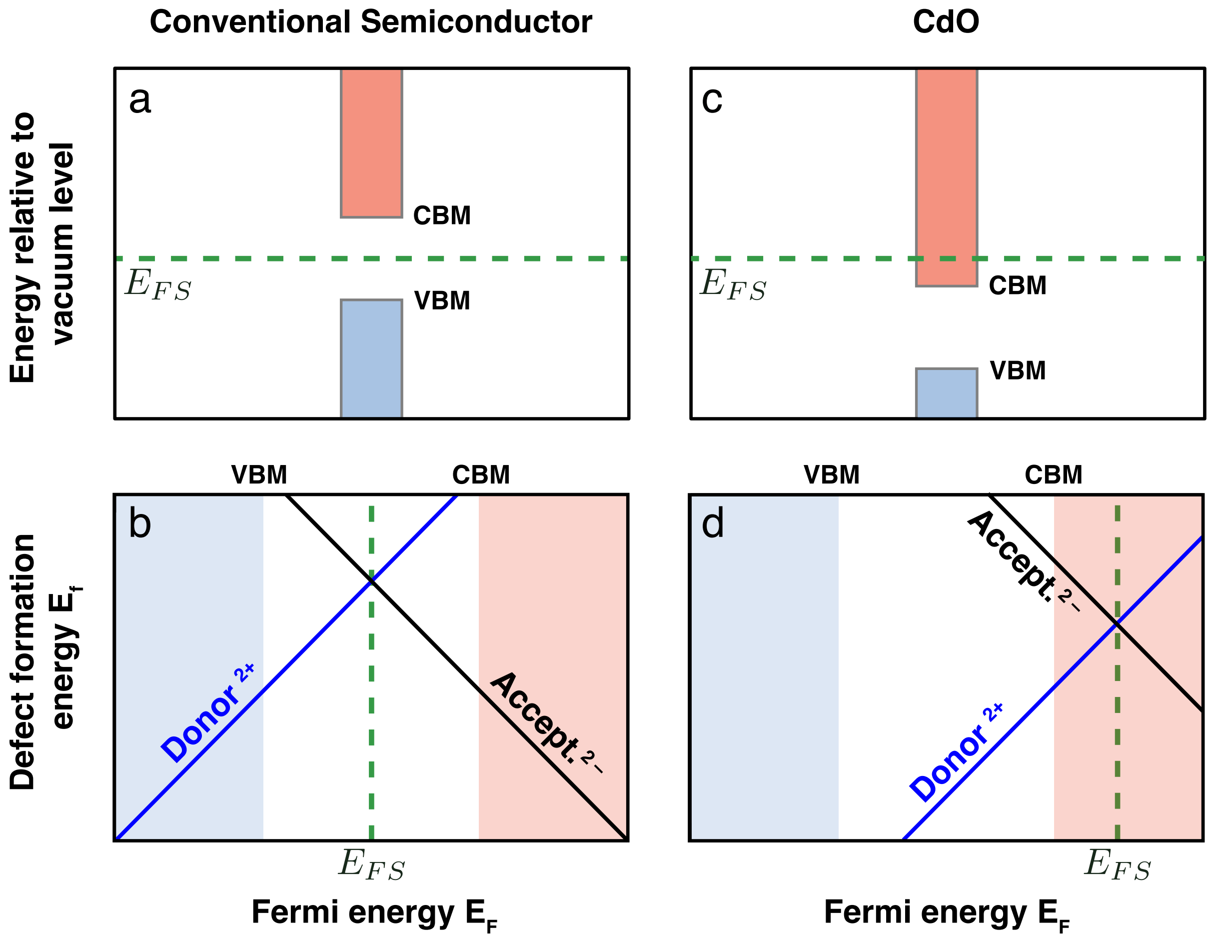

Figure 2.1: Band alignments with respect to the Fermi-level stabilization energy E_{FS} along with Fermi-level-dependent defect formation energies for native donors and acceptors (indicated with charge states of 2^+ and 2^-, respectively). (a) The band alignment of a conventional semiconductor results in E_{FS}, the average energy of native defects, in the bandgap. (b) The formation energy of compensating defects decreases as the Fermi level moves away from E_{FS} and the middle of the gap in this prototypical example, leading to low n-type and p-type doping limits. (c) In CdO, E_{FS} lies above the conduction band. (d) Native donors are thermodynamically favored up to the point where $E_F = E_{\mathrm{FS}}$. Figure modeled after Ref. [68].

is stabilized by high values of E_F. In the case of CdO, shown in Figures 2.1c and 2.1d, E_{FS} lies ~ 1 eV above the CBM [51]. The thermodynamic driving for the creation of unintended native donors is very strong when the Fermi level is near the middle of the gap, and as such nominally undoped CdO films exhibit unintentional n-type conductivity. The fabrication of intrinsic or p-type CdO is therefore predicted to be infeasible. In the case of InN, a material with a smaller bandgap (0.7 eV) and similar absolute positioning of its CBM (defined as the electron affinity E_A), p-type conductivity has been realized[1] through the careful application of nonequilibrium growth methods [71].

A corollary of this concept is that the intentional generation of point defects by particle- and γ-ray irradiation will stabilize the Fermi level at this universal level, saturating the carrier concentration. The genesis of the ADM concept is rooted in observations of such intentional defect generation in a variety of materials [65, 66]. As long as the density of states of the semiconductor is known and this concentration is high enough to measure, the value of E_{FS} relative to the band edges can be determined. By extension, this establishes the values of the band extrema on an absolute scale. For materials in which the stabilized Fermi level causes it to be n-type, the electron affinity E_A is the sum of the Fermi level with respect to the CBM plus the value of E_{FS} below the vacuum level (4.9 eV); for p-type materials, E_{FS} is found with respect to the valence band maximum (CBM). In Chapter 5, this approach will be used to determine the electron affinities and band offsets of $\mathrm{Cd_xZn_{1\text{-}x}O}$ alloys.

The origin of this universality arises from the donor character of these simple, native point defects. At low concentrations, vacancies and interstitials are highly localized in real space and extended in k space. Their position in the band structure does not follow the positions of the band extrema, such as is the case with shallow, hydrogenic dopants; rather, their position is derived from the conduction and valence band density of states averaged over the entire Brillouin zone. When averaged over reciprocal space the total densities of states of most semiconductors looks quite similar, which results in a constant position of E_{FS}. For most semiconductors, the low-density-of-states features that typically comprise the band extrema points protrude somewhat evenly from these high density-of-states regions and E_{FS} is located in the bandgap. If one of these band extrema points protrudes significantly away from the high-density-of-states regions, E_{FS} can be located significantly closer to, or inside, the band. The conduction band of CdO (see Section 2.1.2) exhibits this behavior. The positioning of localized cation d levels is similarly insensitive to the positioning of band extrema, and as such their energy levels can be plotted on same universal plot in Appendix A.1 [67].

Another aspect of the ADM framework that is relevant to TCO materials is that it can be used, to a first approximation, to predict band bending and charge accumulation at external surfaces and extended internal defects such as dislocations [72, 73, 74]. Surfaces, barring any reconstruction effects, are essentially disruptions to the perfect 3-dimensional lattice, with a high concentration of broken bonds, and as such can be considered highly defective. The Fermi level will therefore tend to stabilize at E_{FS} at surfaces. For most semiconductors, this results in charge depletion at the surface and upward band bending; for metal oxides, where E_{FS} is located near or above the CBM, the stabilization of E_F results in surface electron accumulation[2] [68, 72]. For this reason, high-E_A materials such as CdO [68, 72, 73] and

---

[1] The surfaces of such p-type films exhibit n-type surface inversion layers due to Fermi-level pinning at the surface [69, 70].

[2] It is worth noting that absolute reference levels such as E_{FS} or E_{vac} are similarly affected by the electrostatic forces of charge accumulation and depletion.

InN [69, 70, 74] exhibit considerable surface accumulation. Irradiation or doping that moves E_F into alignment with E_{FS} would therefore establish a “flat band” condition at the surface.

The role of hydrogen

First-principles calculations reveal that doping may, additionally, be affected by a universal hydrogen donor/acceptor level in the vicinity of E_{FS} [75]. Such studies claim, for example, that oxygen vacancies behave as deep donors in ZnO and therefore cannot be responsible for its unintentional n-type conductivity; instead, hydrogen donors are the culprit. Validating such simulations remains a challenge, however: the concentration of interstitial hydrogen in semiconductors is extremely difficult to control and unstable at room temperature, casting doubt on its role. Detecting substitutional hydrogen on oxygen vacancy sites is similarly tricky. It may be possible to use vibrational spectroscopy to detect its presence, but direct measurements are inconclusive and instead these approaches rely on introducing additional nitrogen as a passivation species [46]. Despite these strong claims by first-principles simulations, whether unintended hydrogen incorporation plays an additional role in n-type conductivity remains an open question yet to be validated by experiment. Overall, the concept of a universal doping level for hydrogen is complementary to that of the ADM framework, which is valid for native point defects.

2.1.2 Band structure of CdO

The band structure of CdO contains many features that set it apart from other, more conventional semiconductors such as GaAs, and these peculiarities give rise to many of its unique properties. Several of the properties discussed in this section—high electron affinity, low conduction band effective mass, $p-d$ interactions affecting its valence band structure—are also seen to a lesser extent in wurtzite (WZ) ZnO and other common TCOs. Detailed studies of the band structure of CdO have been carried out using first principles calculations [47, 63, 76, 77, 78, 79, 80, 81, 82] as well as spectroscopic [72, 80, 82, 83] and other experimental methods [51, 57, 84].

In a conventional semiconductor, including ZnO, the states near the band edges can be described by parabolic dispersion relations[3]. The same is not true for materials in which there is a high degree of interaction between the conduction band and valence band extrema, and as a result such bands are treated as *nonparabolic*. This effect is strongest in narrow gap semiconductors (InSb, HgTe), but applies to the case of CdO and many TCO materials as well. The dispersion relation for the conduction band is determined by Kane’s $k \cdot p$ model

$$E(k) = \frac{\hbar^2 k^2}{2m_o} - \frac{E_g}{2} + \sqrt{\left(\frac{E_g}{2}\right)^2 + \frac{E_g \hbar^2 k^2}{2m_e^*}}, \tag{2.2}$$

---

[3] At extremely high doping levels and high electric fields, slight nonparabolicity is observed in the conduction band of ZnO[85, 86, 7]

The first term in Equation 2.2 represents the parabolic contribution, but with the electron rest mass m_o; the band-edge effective mass m_e^* is included under the radical. The strength of the nonparabolicity is determined by the direct bandgap E_g terms. An important consequence of this effect is that band filling calculations to determine the Fermi level (and equivalently, the Burstein-Moss shift) in nonparabolic-band materials require the use of Equation 1.6 found in Section 1.3.2.

In contrast to parabolic-band semiconductors, where the effective mass of conduction electrons is proportional to $1/(d^2E/dk^2)$, in the nonparabolic case the curvature is not constant and a new, k-dependent effective mass for conduction electrons can be defined as

$$m^*(k) = \frac{\hbar^2 k}{dE(k)/dk}. \tag{2.3}$$

For degenerate doping levels, where the value of k at the Fermi level $k_F \neq 0$, the effective mass of conduction electrons $m^*(k)$ is greater than the band edge effective mass m_e^* [55, 54].

Details of the band structure of rocksalt (RS)-phase CdO are presented in Figure 2.2. The band structure calculated by density functional theory (DFT) in Ref. [63] is shown on the left in Figure 2.2a, and, as is discussed below, is modified to include the absolute energy scale. Figure 2.2b shows the corresponding k-space diagram of the FCC Brillouin zone for RS-CdO, with the high-symmetry directions from Figure 2.2a indicated. Qualitatively, the general features of this band structure are supported by other calculations and by experiment[4].

As stated previously, the conduction band dispersion of CdO is described by Equation 2.2. Experimental determination of the band-edge effective mass suggests that $m_e^* \approx 0.22m_o$ [87]. The electron affinity E_A of CdO was reported by Speaks et al. [51] to be 5.9 eV—the highest of all known semiconductors. This result is included in Figure 2.2, establishing the absolute energy scale and the position of the band edges with respect to E_{FS}. As discussed in 2.1.1 and simulated in Chapter 7, this extreme positioning of the CBM has profound effects on the electrical behavior and doping limits of CdO. By extension, tuning the energy of the band extrema can, at least in theory, change these limits. Chapter 5 presents experimental evidence and a thorough discussion of how the band offsets of $\mathrm{Cd_xZn_{1\text{-}x}O}$ change with alloy composition.

The valence band maximum occurs at the L symmetry point, giving rise to an indirect bandgap of $\sim$ 1.1 eV. Despite the presence of this low-energy, indirect bandgap, as will be discussed in Section 2.1.3 indirect transitions are not typically observed in thin film CdO samples. E_g^{opt} corresponds to the onset energy for direct-gap transitions observed in optical absorption experiments. The intrinsic, carrier-free bandgap E_g^{dir} is found by correcting for the Burstein-Moss shift E_{BM} and renormalization effects (Sections 1.3.2 and 4.5.1). The upward dispersion of the valence band at the Γ point depicted in this calculation has a negligible effect on E_g^{opt}. As illustrated by the additional band structure details near the Γ-point shown in Figure 2.2c, the upward dispersion away from the Γ point occurs in both the L and K directions, but not the X direction. This negative valence band dispersion

---

[4] Refer to the first paragraph of Section 2.1.2 for references.

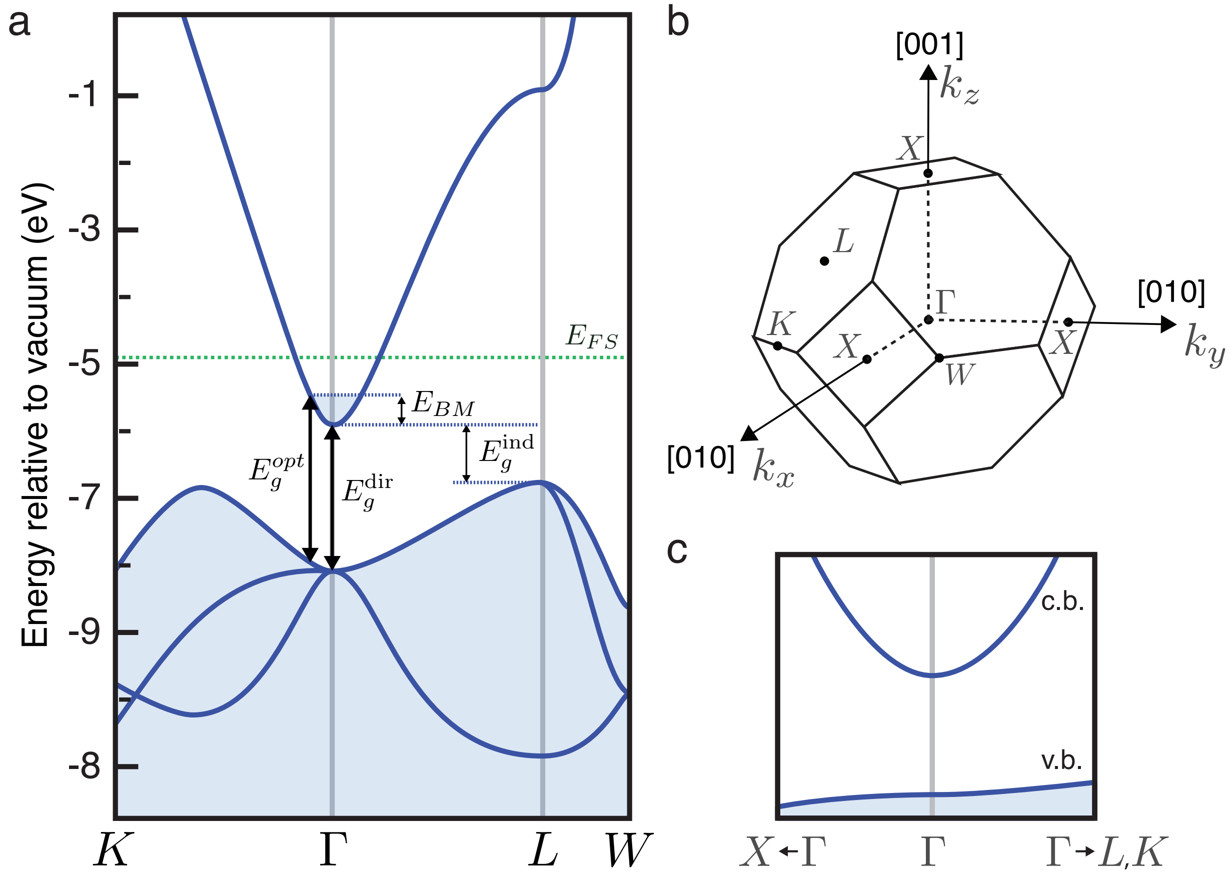

Figure 2.2: Band structure of RS-CdO. (a) The DFT-calculated band structure of CdO. The shaded area represents the band filling that accompanies a typical electron concentration of 2×10^{20} cm^{-3}. The absorption edge E_g^{opt}, Burstein-Moss shift E_{BM}, intrinsic direct bandgap E_g^{dir} (~ 2.2 eV), and indirect bandgap E_g^{ind} (~ 1.1 eV) are indicated, along with the Fermi-level stabilization energy E_{FS}, following the absolute energy scale determined by Ref. [51]. Modeled after Ref. [63]. (b) FCC Brillouin zone for RS-CdO with high symmetry directions marked, along with (c) additional band structure details near the Γ point, modeled after Refs. [68] and [76].

suggests that photo-generated holes would easily and quickly relax to the L point, increasing carrier lifetimes. Preliminary lifetime measurements (not shown) suggest that this is true for indirect CdO and RS-$\mathrm{Cd_xZn_{1\text{-}x}O}$ alloys.

Effect of Cd d states on the valence band structure

The origin of this unique valence band structure is the result of the interaction between cation d levels and oxygen anion p levels that make up the valence band edge. It is conventionally thought that the VBM offsets among III-V and II-VI compounds that share a common anion are small in energy, based on the model that the valence bands of these materials are primarily made up of p-state wavefunctions contributed by the anion species [88, 79].

This general trend can be seen in the band offset diagram of semiconductors in Appendix A.1, where the VBMs of oxide semiconductors are very low in energy compared to those of other compound semiconductors. Similarly, VBM energies of common-cation III-V and II-VI compounds are sensitive to the p orbital energy of the anions, such that the VBM moves to lower binding energy (closer to E_{vac}) with higher atomic number of the anion, (e.g. the ranking of the VBM energies II-chalcogenides from low-energy (high binding energy) to high-energy (low binding energy) tends to follow II-O<II-S<II-Se<II-Te).

This is only a general trend, however, and it cannot explain the (sometimes large) variation in the VBMs among members of a common-cation group. The position of the valence band maximum in II-VI and III-V semiconductor compounds has also been shown to be sensitive to coupling between anion p states and cation d states [47, 79].

In the case of CdO, the $4d$ bands of Cd ([Kr]$4d^{10}5s^2$) located $\sim 9-10$ eV below the VBM hybridize with the $2p$ states of O ([He]$4s^2 2p^4$) that are the primary components of the matrix states of the valence band [82, 81, 89]. Core-level photoemission measurements are used to confirm the position of these shallow core levels [90, 82, 72, 72, 77]. The proximity of these Cd$4d$ states to the valence band edge results in $p-d$ repulsion between them, and a rise in the VBM away from the Γ point, where it is specifically forbidden by symmetry. Similar $p-d$ repulsion behavior from Zn$3d$ electrons contributes to the relatively flat valence band and large hole-effective-mass in ZnO [77, 81].

2.1.3 Electrical and optical properties of CdO

Only a few scattered experimental reports on the electrical and optical properties of CdO appeared over the latter half of the 20th century [91, 92], but since the start of the new millennium interest in its properties has expanded considerably [19, 21, 41, 42, 64, 84, 93, 94, 95]. Early reports on the transport properties of annealed CdO single-crystals demonstrated its excellent carrier mobility, finding that $\mu > 200$ cm^2/Vs at carrier concentrations below $\sim 10^{19}$ cm^{-3} [91], considerably higher than the mobility reported for post-growth-annealed single-crystal thin films [64]. The dependence of oxygen vacancies and native defects on the conductivity was clear in even in early bulk crystal studies [91].

Figure 2.3 summarizes the recent work by Yu et al. [19] on Ga- and In-doped CdO films grown by pulsed laser deposition (PLD). As indicated by the mobility vs. concentration plot in Figure 2.3a, doping by Ga or In enhances the mobility. While as-grown, nominally undoped films show $\mu \sim 100$ cm^2/Vs, Ga-doped films show $\mu \sim 100$ cm^2/Vs. This increase in mobility by impurity doping is counterintuitive—normally the addition of dopants increases the total scattering contribution by ionized impurity scattering—but such results can be understood within the ADM framework. As will be discussed in Chapter 7, where the mobility and concentration will be modeled for doped CdO samples, the interplay between native defects and intentional dopants can account for this behavior. An indication of this is given

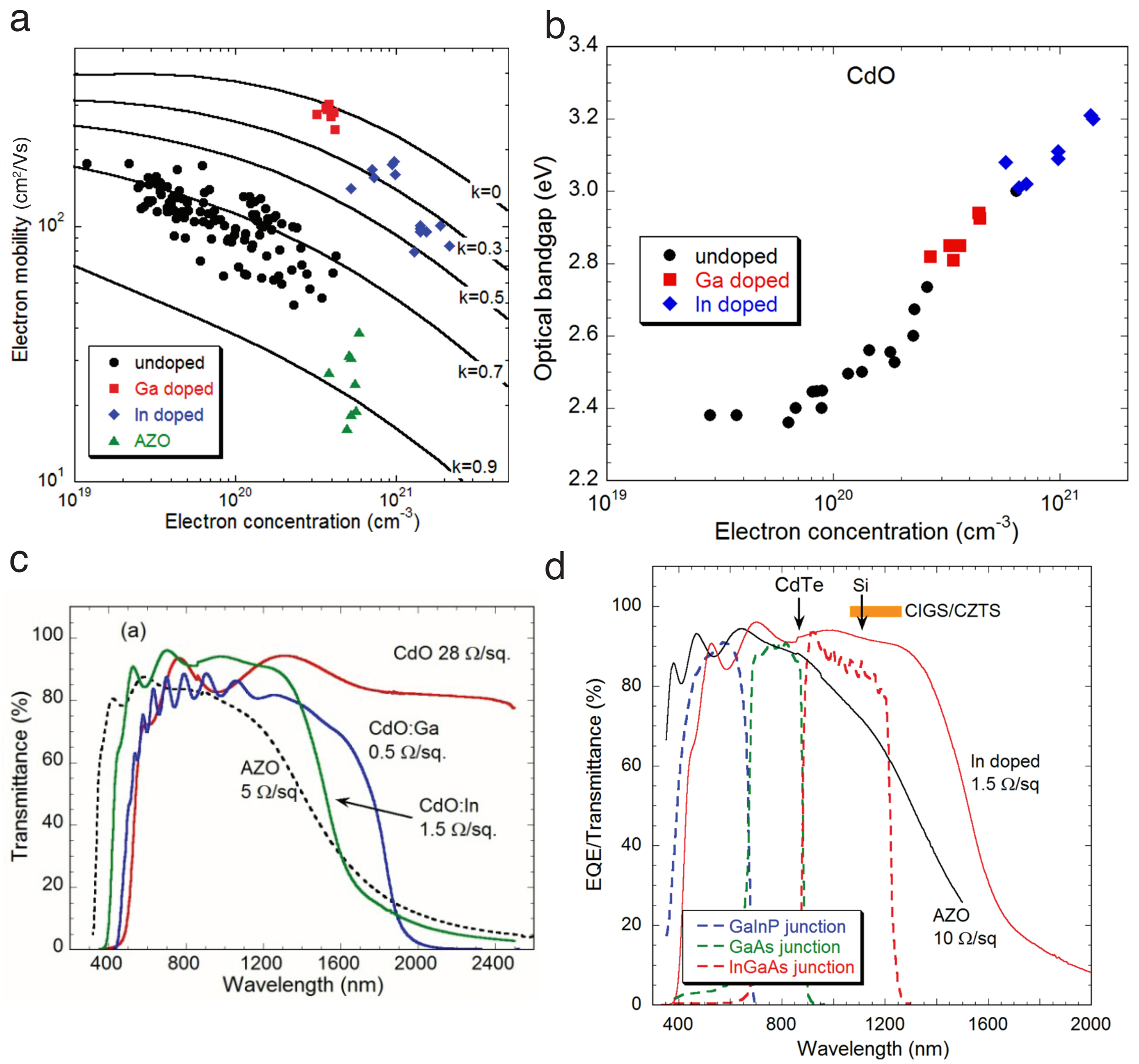

Figure 2.3: Summary of electrical and optical properties of nominally undoped and doped-CdO. (a) The electron mobility vs. concentration are plotted for nominally undoped and impurity-doped CdO thin films, with calculated curves based on the compensation ratio. The increase in mobility upon Ga- and In-doping will be explored in Chapter 7. (b) E_g^{opt} for different doping levels up to $n > 10^{21}$ cm^{-3}. The total Burstein-Moss shift is ~ 1 eV. (d) Different doping levels, indicated by values of R_s, indicate that it is possible to make moderately conducting CdO with an IR transparency cutoff > 2500 nm. (c) High-mobility, In-doped CdO is an ideal TCO for low-bandgap absorbers, but its low fundamental gap limits short-wavelength transparency. Figures (a), (b) and (d) are from Yu et al. [19], (c) is courtesy of K.M. Yu.

by the compensation ratio curves, calculated by the same procedure used in Chapter 7, suggesting that doped CdO may have fewer compensating defects than the nominally undoped case. By comparison, the substantial role of mobility-limiting ionized impurities can be seen by this high compensation ratio.

Figure 2.3b demonstrates that the low-m_e^* of the conduction band of CdO results in significant Burstein-Moss shift in E_g^{opt}. At $n > 10^{21}$ cm^{-3}, the total shift relative to the intrinsic direct band gap E_g^{dir} is ~ 1 eV, and $E_g^{opt} \sim 3.2$ eV. The effects of this doping on transparency are seen in Figure 2.3c, where doping can produce either a material with excellent IR transparency (> 2500 nm) and moderate sheet resistance ($R_s = 28\,\Omega/\square$), or a material with more limited IR transparency, but still with better transparency and sheet resistance than AZO.

In Figure 2.3d, the transmission spectra of doped CdO films are overlaid with the external quantum efficiency (EQE) for a multijunction solar cell. The bandgaps of other PV absorber layers are indicated as well. In contrast to AZO, the long-wavelength transparency of which is limited by significant free carrier absorption, for In-doped, high-mobility CdO the FCA cutoff occurs at longer wavelengths, suggesting that it may be an ideal TCO for Si and other low-bandgap absorbers. The critical shortcoming of CdO, however, is that its high-energy transparency limit, even with $E_g^{opt} \sim 3.2$ eV, is too low for full-spectrum PV applications such as the multijunction cell indicated. Alloy engineering of CdO, a concept introduced in Section 2.2 and explored experimentally in Chapters 4 and 5, may indeed overcome this by increasing the fundamental bandgap.

2.2 Bandgap engineering of semiconductor alloys

The successful development and widespread adoption of any individual semiconductor materials system for optoelectronic device applications depends on how well its optical, electrical, and structural properties can be controlled. The physical design of such devices is simultaneously guided by detailed knowledge of the electronic structures of the constituent materials, such that electric fields at interfaces are tailored to guide the movement and confinement of charge carriers in the device. Strain, doping, optical properties, and composition must all be carefully managed carefully to produce a functional device.

Alloy engineering can be used to vary all of these properties, although not independently and generally not linearly. A general approach to predicting how the properties of semiconductor alloys will vary with composition is to use the Virtual Crystal Approximation (VCA), which replaces the atomic potentials at every site in the alloy with that of an average, effective potential. Under this model, the lattice constant of a compound semiconductor alloy $\mathrm{A_xB_{1\text{-}x}C}$ can be estimated to vary linearly between those of the two endpoint compounds AC and BC, and in practice this trend is observed in real systems. Provided that the two endpoints compounds are fully miscible, the lattice expansion or compression follows this linear trend, known as Vegard's law. Optical and electrical properties, however, deviate significantly from this linear, weighted average approach. Even within the VCA framework, for example, a nonlinear trend in the bandgap is expected [15, 96].

Empirically, the bandgap of a compound semiconductor alloy $A_xB_{1\text{-}x}C$ tends to follow a quadratic dependence[5] x such that

$$E_g^{(\mathrm{A_xB_{1-x}C})} = xE_g^{(\mathrm{AC})} + (1-x)E_g^{(\mathrm{BC})} - bx(1-x) \tag{2.4}$$

where b is a fitting term known as the bowing parameter. Random and non-random alloy variations contribute to potential fluctuations in the conduction and valence band edges, leading to bandgaps that are lower than expected. The strength of this bowing behavior therefore depends partially on the relative band offsets of the conduction band minima and valence band maxima of the endpoint alloys. Alloy systems with regions of immiscibility are also seen to exhibit a high degree of bandgap bowing. While the bandgap bowing parameter is a useful indicator for estimating the strength of alloy disorder effects and bandgap trends, however, it is only a rough empirical guide and its exact value should not be overanalyzed. Indeed, in alloys such as AsGaAs and AlInP, complex bowing behavior is observed [96]. A general reference for the properties of compound semiconductor alloys can be found in Ref. [97].

The electrical mobility is another important property that is sensitive to band edge potential fluctuations, and therefore exhibits similar bowing behavior. For n-type conductivity, which is affected by fluctuations in the CBM, the component of the total mobility due to alloy disordering is

$$\mu_{\mathrm{AD}} = \frac{\hbar^3 \pi e}{m^* k_F \left|V_{\mathrm{CBM}}\right|^2 x(1-x)} \tag{2.5}$$

where Ω is the (real space) unit cell volume and where the potential term

$$\left|V_{\mathrm{CBM}}(x)\right| = \left|\frac{dE_{\mathrm{CBM}}}{dx}\right| \tag{2.6}$$

is the change in the band edge potential with x. As in the case of bandgap bowing discussed above, to a first approximation $V_{\mathrm{CBM}} = \Delta E_{\mathrm{CBM}}$, the absolute difference in potential of conduction band minima of the endpoint alloys. For p-type materials this term describes fluctuations in the VBM [98]. Although isovalent cation substitution in an alloy such as $A_xB_{1\text{-}x}C$ should not directly affect the doping properties of the material, the band offsets play a critical role in determining the electrical behavior of amphoteric native defects, as discussed in Section 2.1.1, and as such alloying may change both the unintended native conductivity and doping limits of materials.

In order to understand the behavior of semiconductor alloys it is therefore critical to study the compositional trends in the structural, electrical, optical properties as well as changes in band edge energies with composition. In Chapters 4 and 5, these trends are investigated for the specific case of $Cd_xZn_{1\text{-}x}O$ alloys.

---

[5] A significant counterexample to this quadratic bowing behavior is the bandgap reduction observed in highly-mismatched alloys (formed by anion substitution), in which the negative deviation is better modeled by the quantum-mechanical anticrossing of impurity states with the band edges.

Table 2.1: Basic properties of CdO, MgO, and ZnO. Compiled from Refs. [7] and [84].

	Crystal structure	Lattice parameter (Å)	Indirect bandgap (eV)	Direct bandgap (eV)	Electron affinity (eV)
CdO	Rocksalt	$a = 4.696$	~ 1.1	~ 2.2	5.9
ZnO	Wurtzite	$a = 3.24, c = 5.20$	–	3.3	4.9
MgO	Rocksalt	$a = 4.24$	–	7.7	~ 0

2.3 Bandgap engineering of CdO–ZnO–MgO pseudobinary alloys

The CdO–ZnO–MgO alloy system is the II-VI analog of the well-studied InN–GaN–AlN system, as discussed in Chapter 1. Unlike the binary compounds of the III-N system, however, the components of the II-O system are structurally mismatched. The phase stability of II-O ternary alloys is therefore an area of significant interest. As well, bandgap trends across the composition do not connect from endpoint to endpoint, with discontinuities at composition points of phase instability.

The equilibrium crystal structures of II-O materials are summarized in Table 2.1, along with their basic structural and optical properties. CdO and MgO both exhibit cubic rocksalt crystal structures, while ZnO exhibits a hexagonal wurtzite structure. The majority of II-O bandgap engineering studies are focused on alloys of ZnO, given its excellent optical properties and near-visible bandgap (3.3 eV). By alloying ZnO with higher-gap MgO ($\sim$ 7.7 eV) and lower-gap CdO ($\sim$ 2.2 eV), it is possible to tune the luminescence and absorption of ZnO. The properties of these alloys are summarized briefly in the following sections.

Figure 2.4a summarizes the present state of band structure engineering for the CdO–ZnO–MgO alloy system in terms of a bandgap vs. lattice parameter plot that is conventionally drawn for alloy engineering systems. As noted above, two of the three pseudobinary alloys are structurally mismatched, and thus no continuous bandgap trends should be expected. Table 2.1 also presents the values of the electron affinity for each II-O material. From this information and the bandgap values, it is possible to construct the band offset diagram for II-O materials shown in Figure 2.4b. The offsets of Si are included for reference. The CBM of MgO has been reported to be near or above E_{vac}, and its ionization potential (VBM) has been observed to be $\sim$ 6.9 eV [103, 104]. The $\sim$ 1 eV offset between the CBM of ZnO and CdO suggests that band gap reduction may be accommodated by both the conduction band and the valence band, but again caution must be observed in comparing the two endpoints of dissimilar structure.

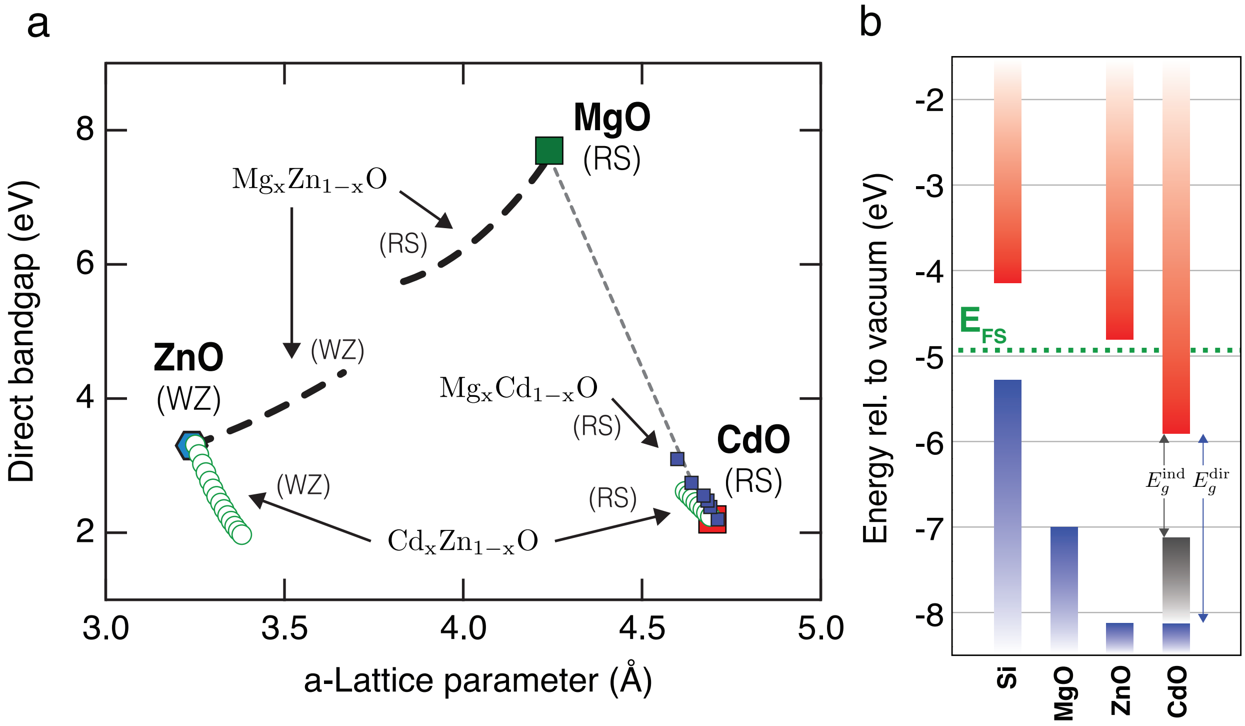

Figure 2.4: Bandgap engineering of CdO–ZnO–MgO. (b) The bandgap trends between structurally mismatched binary endpoints need not connect, as seen for the cases of CdO–ZnO alloys (green circles), or MgO–ZnO (thick dashed line). RS-$Mg_xCd_{1-x}O$ alloys (thin dashed line) are predicted to form across the entire CdO–MgO composition range, but solubility issues prevent good incorporation of Mg in CdO (data: blue squares). $Cd_xZn_{1-x}O$ data is calculated from Refs [99, 100], $Mg_xZn_{1-x}O$ trends are summarized from Ref. [6], and $Mg_xCd_{1-x}O$ data is from Ref. [101]. (b) Band offsets of ZnO [102] and CdO [51], along with Si for comparison [75]. As discussed in Section 2.1.2, the VBM of CdO is $\sim$ 1.1 eV higher than the valence band position at the Γ point. There is a $\sim$ 1 eV CBM offset between CdO and ZnO.

2.3.1 $Mg_xZn_{1-x}O$

The study of $Mg_xZn_{1-x}O$ alloys is motivated both by the prospect of tuning the emission and absorption of ZnO and by the need for materials with higher conduction band potentials, which are used to create quantum confinement in heterostructures. In a $Mg_xZn_{1-x}O$ / ZnO / $Mg_xZn_{1-x}O$ heterostructure, carriers in ZnO can be confined in a potential well between two barrier layers [6]. The device structure is critical for design of LEDs and lasers. In the case of Mg incorporation in WZ-ZnO shown in Figure 2.4a, the bandgaps and lattice parameters of WZ-$Mg_xZn_{1-x}O$ (thick dashed line, adapted from summarized data in Ref. [6]) coincidentally both trend toward those of the RS-MgO endpoint, but at high Mg concentration the WZ phase is unstable and the system separates into RS and WZ phases for the middle part of the composition range. Successful *p*-type doping by native defects [105] and impurity doping by nitrogen [106] have been reported in $Mg_xZn_{1-x}O$ as well, in both cases perhaps due to an increase in the VBM suppressing the formation of native donors.

2.3.2 $Mg_xCd_{1-x}O$

There have been very few experimental reports of $Mg_xCd_{1-x}O$ films, in part because II-O bandgap engineering efforts are focused on the modification of ZnO. Nonetheless, $Mg_xCd_{1-x}O$ films may play an important role in TCO applications, as the MgO–CdO alloy system offers structurally matched, RS-phase endpoint binary compounds and an opportunity to increase the fundamental bandgap of CdO. In the case of $Mg_xCd_{1-x}O$ films, as shown in Figure 2.4a, the cubic RS equilibrium phase is expected for all alloys, but structural stability of these alloys—driven in part by the extreme differences in ionic radii of the cation species—results in poor incorporation of Mg into CdO [107, 108, 101]. Experimental data (blue squares) calculated from Ref. [101] are shown. While the bandgap increase is significant, the conductivity of such films decreases dramatically with Mg incorporation, a result of alloy disorder scattering limiting the mobility and a rise in the CBM above E_{FS} decreasing the concentration of native donors.

2.3.3 $Cd_xZn_{1-x}O$

Investigations into the properties of CdO–ZnO alloys have focused primarily on the composition range comprising the wurtzite (WZ)-structured alloys, where near-band-edge luminescence can be tuned across the visible range [109, 110, 100, 111, 112, 113, 114]. First reported in 1996 by Choi, Lee, and Cho [109], $Cd_xZn_{1-x}O$ was initially synthesized by sol-gel techniques. Following this, Makino et al. [115, 110] reported the growth $Cd_xZn_{1-x}O$ thin films up to 0.07% by pulsed laser deposition (PLD) on nearly lattice matched (0.034%) $ScAlMgO_4$ substrates. One significant obstacle to studying the $Cd_xZn_{1-x}O$ alloy system is the low equilibrium solubility of Cd in ZnO ($\sim 2\,$at.%) [116], but this has been overcome through the application of optimized, nonequilibirum growth techniques. Further details regarding the growth of $Cd_xZn_{1-x}O$ thin films will be discussed in Chapter 3.

In Figure 2.4a, the $Cd_xZn_{1-x}O$ data reported by Ishihara et al. [100, 99] is used to calculate the bandgap vs. lattice parameter points (green circles) for both WZ and RS-$Cd_xZn_{1-x}O$ alloys. These results show significant incorporation of Cd into WZ-ZnO (up to $\sim$ 70%) before there is a discontinuous jump in the properties to those of the RS alloys. Other reports suggest that Cd incorporation $x > 0.65$ is possible [114, 117], but there is still disagreement on the value of E_g for the alloys, and no effort has been made to measure and account for the electron concentration in these films.

There have also been very few reports of first-principles calculations of the properties of $Cd_xZn_{1-x}O$ alloys to accompany the growing (although still very basic) set of experimental data. Both the structural stability and electronic structure have each been calculated, however. *ab-initio* free energy calculations suggest significant phase stability of $Cd_xZn_{1-x}O$ up to x=0.95, but note that the small energy difference between RS-CdO and WZ-CdO phases may complicate these simulations, and further note the possibility of a large miscibility gap in the alloy system [118]. Electronic structure calculations predict that reduction in the bandgap is accommodated nearly equally by the movement of both the conduction band and valence band [119]. This claim will be tested experimentally in 5.

As discussed previously, there has been renewed interest in CdO-based materials for transparent conductor applications due to their outstanding electron mobility and infrared (IR) transparency, but to date there have been relatively few investigations of RS-structured $Cd_xZn_{1-x}O$ alloys. Notably, the papers by Ishihara et al. [100, 99] are the only existing reports regarding the basic optical and structural properties RS-$Cd_xZn_{1-x}O$ alloys. As seen in Figure 2.4a, the RS-phase alloys (green circles) increase in bandgap along with Zn incorporation in RS-CdO. The electrical properties of these films are not reported, although they are potential candidates for broad-spectrum TCO applications given that their fundamental gaps are higher than that of CdO.

In Chapter 4, the optical, electrical, and structural properties of both RS- and WZ-$Cd_xZn_{1-x}O$ thin films are investigated and these results are correlated with changes in the band offsets (Chapter 5). The resulting picture connects trends in the mobility and bandgap across the composition range and offers new insights into how the unique properties of the $Cd_xZn_{1-x}O$ system make it intriguing for novel device applications, including as a photoanode for photoelectrochemical devices for water splitting.

On a final note, the potential environmental release of Cd, a known carcinogen, remains an important concern and must be managed at three stages: during manufacturing, during the life of the product, and at the end-of-life stage in which Cd must be recycled or disposed of safely [120]. Elemental Cd, itself a byproduct captured during the refinement of zinc, lead, and copper processing, is employed in two major commercial uses: it has been used for decades as an electrode material in Ni-Cd batteries, and recently it has been used in the form of CdTe and CdS in thin-film PV applications [121]. Unless there is an economic incentive to recover Cd from the waste byproducts of the processing of the more industrially relevant metals, the potential for its rerelease into the environment is quite high. In the United States the environmental effects of Cd are regulated economically by mandating that the recycling cost be included in the battery price to offset the work necessary to collect and process used batteries. Similar costs are now built into PV technologies [122]. On a device level, the release of Cd from PV modules is safeguarded in two ways: first, Cd exists in either telluride or oxide form, both of which far less toxic than elemental Cd; second, encapsulation methods are used in all PV devices to trap device layers beneath glass and high-stability polymer layers. While the European Union has banned the sale of consumer Ni-Cd batteries and has recently considered such a ban on the production and sale of Cd-containing PV technologies, to date no such action has been taken. CdTe absorber materials are a dominant thin-film PV technology and occupy a significant portion of the total global PV market share–9% as of 2010, falling to 5.5% in 2011 and as such the regulatory, economic, and technological considerations for safe handling of Cd have long been considered [123].

Chapter 3

Thin film growth and compositional analysis of $Cd_xZn_{1\text{-}x}O$ alloys

$Cd_xZn_{1\text{-}x}O$ alloys have been synthesized by a variety of methods, including sol-gel processes [109], pulsed laser deposition [110, 124], solid-state powder methods [125], RF magnetron sputtering from ceramic $Cd_xZn_{1\text{-}x}O$ targets of fixed composition [126], reactive sputtering from elemental targets [127, 114], metalorganic chemical vapor deposition (MOCVD) [128, 99, 100], and molecular beam epitaxy with an RF oxygen radical source [129, 111]. The highest Cd incorporation ($x > 0.65$) in WZ-$Cd_xZn_{1\text{-}x}O$ has been reported for reactive processes such as MOCVD and reactive sputtering from metal (Zn, Cd) sources. Thin film deposition has been carried out using a variety of common substrates, including glass, quartz, *a*-plane [99, 100, 111] and *c*-plane sapphire [124, 128], and Si(111) [127]. In all cases, WZ-$Cd_xZn_{1\text{-}x}O$ thin films are polycrystalline and show a preference for *c*-axis texturing, a phenomenon common to the growth of wurtzite films such as ZnO and GaN.

This chapter presents the growth of $Cd_xZn_{1\text{-}x}O$ thin films by pulsed, filtered cathodic arc, a plasma-based technique that reacts metal ions from pure metal (Zn, Cd) with oxygen gas to form a ternary metal-oxide alloy thin film. Section 3.1 provides an overview of the experimental technique and outlines the basic physical mechanisms upon which cathodic arc methods are based. Section 3.1.1 provides the specific growth parameters and details of the experimental setup applied in this study, and Section 3.2 discusses the thickness and composition characterization results obtained from Rutherford backscattering spectrometry (RBS) analysis. A discussion of the RBS technique and an example of the fitting procedure used to extract thin film composition and thickness for $Cd_xZn_{1\text{-}x}O$ films is given in Appendix A.2.

3.1 Pulsed filtered cathodic arc deposition

The family of deposition techniques that rely on vacuum "arc" processes has a long history, starting with Thomas Edison's patent for duplicating phonograms (phonograph recordings) by running high currents into a metal cathode in a vacuum and directing the resultant "metallic vapor" at wax molds [130]. In the middle of the 20th century, arc sources for depositing metal coatings were investigated and refined for industrial applications. By the 1970s, reactive arc processes for the creation of wear-resistant and decorative metal-nitride films were developed [131].

The main limitations on the application of vacuum arc deposition technologies to the synthesis of high-quality metal-oxide alloys have been 1) the limited control of the location of the arc on the surface of the cathode, which leads to unstable growth processes, and 2) the presence of metal "macroparticles" that are ejected in the process of creating high-density metal plasmas by high-current electric arcs [132]. Each of these limitations has been addressed through the development of direct-current and pulsed sources and the implementation of efficient macroparticle filters, resulting in the use of cathodic arc deposition methods to create high-quality metal-oxide films for research and industrial applications [131, 132].

The physical mechanisms of cathodic arc processes have been well studied for a variety of materials[1] [131, 132, 134, 135]. The fundamental process to all arc-related techniques is the creation of a metal plasma by creating a high-current electric discharge from an anode into a metal cathode. At a μm-scale spot on the cathode surface, the high current density of the arc incites the metal to undergo an explosive phase transformation to a plasma state. The physics of the generation and evolution of such cathode spots over time is the subject of ongoing investigation, but the result of this complex discharge behavior is the production of a fully-ionized metal plasma along with relatively smaller amounts of evaporated neutral species and the ejection of macroparticle droplets. This discharge can be run continuously (direct-current (DC) mode), in which case high deposition rates (up to 250 nm/min for AZO [136]) are possible, or in a pulsed mode. For pulsed-arc designs, the cathode source area can be modified to include multiple metal cathodes that share a common anode but are pulsed independently [137, 133].

In filtered cathodic arc, the total output of the discharge is directed toward a bent solenoid coil in which the magnetic field can be used to separate the desired plasma phase from neutral species. As the output species (plasma, neutrals, and macroparticles) move away from the cathode and into the vacuum, the plasma decreases in density and the species enter a metal coil that acts as a solenoid. A current is run through the metal coil such that the resulting magnetic field acts on the moving electrons of the plasma. The ion species are pulled along indirectly via electrostatic interaction with the plasma electrons [137, 133]. The magnetic field of the solenoid is pointed along the axis of the coil cylinder and only serves to steer the plasma, not to accelerate it toward the substrate. Neutral evaporated species are unaffected by this magnetic field and move through the filter or are deposited on its coils. Macroparticles, even if they are charged, have far too high a mass-to-charge ratio to be steered toward the substrate and are simply deposited elsewhere in the chamber. Both S-shaped double-bend and elbow-shaped single-bend solenoid designs have been developed, in addition to dual-filter designs that allow for completely independent cathode sites [137].

---

[1] The book by Anders [133] offers an excellent overview of the fundamental physics of cathodic arc processes.

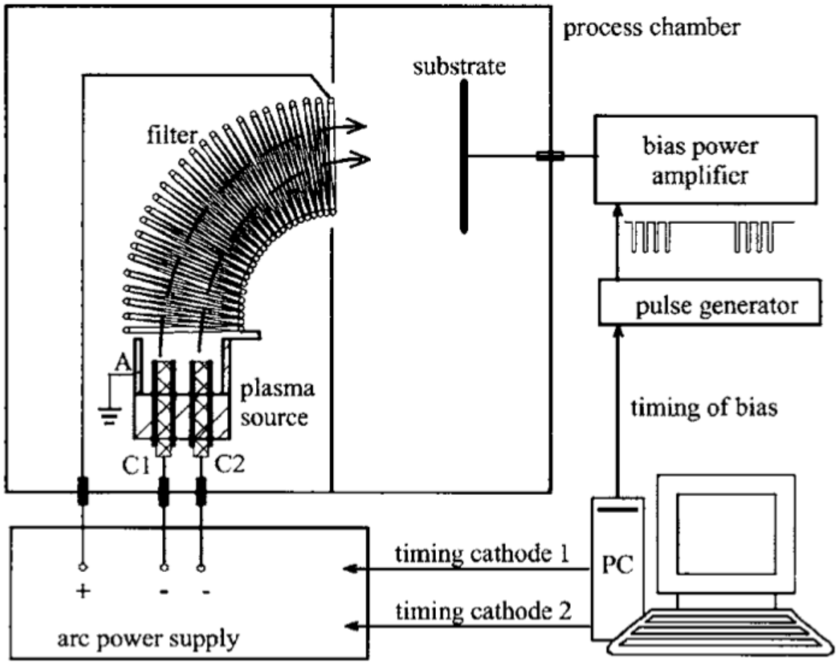

Figure 3.1: Dual-cathode, pulsed filtered cathodic arc deposition (PFCAD) setup with optional substrate bias. From Ref. [137].

A schematic for a dual-cathode, pulsed filtered cathodic arc (PFCAD) device is shown in Figure 3.1 [137].

It is important to note that in cathodic arc processes, the current is set experimentally and the voltage delivered to the cathode is self-adjusting to meet the energy needed to sustain the discharge [138, 135]. The typical kinetic energy of an ion species in unbiased cathodic arc processes is $20 - 200$ eV. It has been shown that this kinetic energy, the distribution of ion charge states, and the self-adjusting arc voltage all depend on the cohesive energy of the metal source cathode. The average kinetic energy of Zn atoms in cathodic arc processes, for example, has been observed to be around 36 eV, although in reactive deposition some of this energy is lost to interactions with the process gas. As noted in Figure 3.1, it is possible, although not always desirable, to apply a bias voltage to the substrate. This bias can be applied to filter the incident ions based on their charge state or to increase their kinetic energy as they reach the substrate, which in many cases results in higher-quality film growth by enhancing surface mobility and adhesion [137]. In contrast to magnetron sputtering, where unintended and undesirable high-energy (> 200 eV) ions can bombard the substrate, in cathodic arc processes it is easier to control the presence and energy of species that are available to participate in growth [139]. Negative substrate bias can also enhance the interaction of the metal ions with the process gas. The choice of reactive process gas depends on the compound desired, but both molecular nitrogen and oxygen have been used

Table 3.1: Growth conditions for PFCAD $Cd_xZn_{1-x}O$ films.

Sub. Type	Sub. Temp. (°C)	Source Cath.	Source Cath.	Arc Volt. (V)	Arc Curr. (A)	O_2 Flow (SCCM)	O_2 Part. Pressure (Torr)	Base Pressure (Torr)
Glass	300	Cd	Zn	500	610	42	7×10^{-3}	7.5×10^{-7}

to created compound films. The interaction of the process gas with the ion flux induces dissociation and ionization of the process gas, and as such higher kinetic energies of ions can promote higher rates of compound formation [132, 137].

Cathodic arc methods have proven to be capable of producing high quality metal-oxide materials, specifically TCOs. High quality ZnO films have been demonstrated using both DC filtered arc [136] and PFCAD [139]. Similarly, CdO films with excellent electrical and optical properties have been grown by PFCAD [94, 95]. Although high-quality films of each of these binary compounds have been created using PFCAD, the synthesis of $Cd_xZn_{1-x}O$ alloys using dual-cathode PFCAD has not been demonstrated previously.

3.1.1 PFCAD of $Cd_xZn_{1-x}O$

In this work, thin films of $Cd_xZn_{1-x}O$ were deposited on glass substrates using dual-cathode PFCAD with elemental Zn and Cd rods as cathodes, following the experimental setup shown in Figure 3.1 with no applied bias voltage and with the addition of O_2 as a process gas. The cathode rods (1/4 in. diameter) were vertically stacked and electrically isolated from one another in separate circuits, though sharing a common anode, so that the discharge could be independently triggered to occur only one at a time. The rods are surrounded by an insulating alumina sheath that prevents arc spots from forming anywhere but the tip of the rod. The macroparticle filter used was a 90° quarter-taurus filter, illustrated in Figure 3.1

The growth parameters common to all films in this work are summarized in Table 3.1. The growth parameters were chosen to optimize the electrical mobility of the CdO endpoint and were based on previous CdO deposition results using the same experimental setup [94, 57]. The base vacuum pressure of 7.5×10^{-7} Torr was maintained by cryogenic pumping. Oxygen flow into the growth chamber was controlled using a mass flow controller set to a flow rate of 42 SCCM. By partially closing the gate valve on the cryo pump, the total chamber pressure could be maintained at 7 mTorr during growth.

The substrates were radiatively heated to 300°C prior to deposition. The nominal substrate temperature was measured by a thermocouple embedded in the substrate holder and is only a rough estimate of the temperature at the substrate surface. The substrates used in this work, soda lime glass microscope slides, were cleaned with Liquinox, an industrial glass detergent that has been shown to clean surfaces without leaving organic residue [136], before being mounted in the chamber. In each growth run, three 1 in.×3 in. glass slides were vertically stacked, yielding a total growth area of 3 in.×3 in. The substrate was kept stationary during growth.

A 1 ms pulse duration with a current amplitude of 610 A was alternately delivered to the metal cathodes at a repetition rate of 1 pulse per second. The resulting arc voltage delivered by the power supply was $\sim$ 500 V. The ratio of Zn and Cd was controlled by varying the pulsing sequence of the respective metallic cathodes. For reach growth run, a desired Cd:Zn ratio was determined and the total number of pulses was set to achieve a whole-number ratio. Pure CdO and ZnO films were grown to determine the relative growth rate of the two endpoint compounds.

Following each growth run, the composition and thickness of the samples was measured by Rutherford backscattering spectrometry (RBS) using a 3 MeV He^+ ion beam. Although RBS is relatively non-destructive compared to other ion-beam tools such as secondary ion mass spectrometry, bombardment by 3 MeV He^+ ions can produce point defects within the mm-scale probe area of the beam. The samples were then sectioned into 1 cm×1 cm pieces such that the areas immediately adjacent to the RBS spots were chosen for further analysis. RBS spectra were fitted using SIMNRA [140] and SIMTARGET [141]. An example of this fitting procedure is provided in Appendix A.2.

3.2 Thickness and composition results

A summary of the pulse ratio details and RBS results for each PFCAD growth run of $Cd_xZn_{1-x}O$ is presented in Table 3.2. Samples were grown with Cd:Zn pulse ratios of 0:1 (ZnO), 1:6, 2:5, 5:2, 10:1, 7:1, 6:1, and 1:0 (CdO). The samples vary in thickness from 45 nm to 240 nm as a result of different total pulse numbers used in each growth run and as a result of the thickness variation across the 3 in.×3 in. growth area.

Additionally, there are significant compositional variations across the entire growth area. This inhomogeneity arises due to the the stacked configuration of the source cathodes (Upper=Zn, Lower=Cd) inside the source and the lack of substrate rotation in the chamber. As a result, the film growth is combinatorial in nature. The sample positions indicated refer to the vertical position along the center section of the film, with 1 (top middle) and 6 (bottom middle). For most growth runs, RBS spectra were recorded at a total of 18 spots, representing the upper/lower and left/center/right of each horizontally-oriented glass slide. The combinatorial nature of the growth is illustrated in Figure 3.2, in which the thickness and composition of each film is plotted against one another. Each growth run is grouped by color with the Cd:Zn pulse ratio indicated in the legend. The cause of the low thicknesses of films at high pulse ratios (samples CZO_07-9) is not immediately clear, given the higher per-pulse growth rate of the higher CdO endpoint. Evolution of the Cd cathode, which was used for multiple growth runs, may play a significant role. The cathode may need to be replaced or reconditioned after a number of growth runs.

The deposition rate of ZnO is calculated to be 0.072 nm per pulse, while that of CdO is 0.112 nm per pulse. For a 1 ms pulse this corresponds to an effective instantaneous growth

Table 3.2: Growth parameters and RBS results for PFCAD $Cd_xZn_{1-x}O$ films.

Name	Sample Position	Cd:Zn Pulse Ratio	Total Pulses	RBS Thickness (nm)	RBS x (Cd)
CZO_00	3	0:1	1000	71	0.00
CZO_04	1	1:6	2280	121	0.05
	2			165	0.05
	3			200	0.07
	4			206	0.08
	5			158	0.13
CZO_05	1	2:5	2429	105	0.09
	2			200	0.09
	3			240	0.13
	4			238	0.19
	5			210	0.25
	6			130	0.30
CZO_06	1	5:2	2000	106	0.51
	2			146	0.53
	3			203	0.62
	4			204	0.67
	5			161	0.69
	6			100	0.69
CZO_07	1	10:1	1892	54	0.74
	2			68	0.74
	3			98	0.76
	4			105	0.78
	5			93	0.79
	6			75	0.82
CZO_08	1	7:1	1800	45	0.74
	2			62	0.73
	3			93	0.74
	4			76	0.76
	5			76	0.70
	6			64	0.80
CZO_09	1	6:1	1800	59	0.72
	2			77	0.70
	3			98	0.75
	4			103	0.72
	5			102	0.76
	6			82	0.82
CZO_01	3	1:0	1000	112	1.00

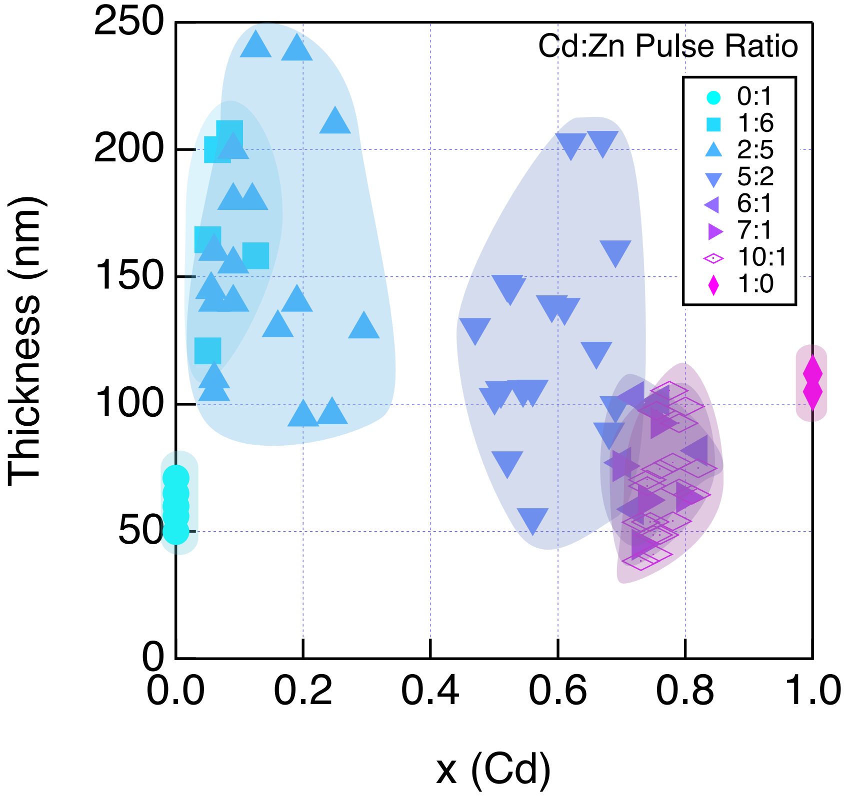

Figure 3.2: The lack of substrate rotation in the PFCAD films results in combinatorial growth experiments. There are both thickness and composition gradients across the 3 in. × 3 in. growth area.

rate of 72 nm/s and 112 nm/s, respectively, although the dynamics of a full one second arc would be inherently different than those of shorter duration. The details of the growth kinetics, oxidation processes, evaporation properties, and thermal decomposition properties of the growing CdO and ZnO films are likely different for the two endpoint alloys, leading to the different growth rates. This per-pulse growth rate is useful for calibration purposes, and in theory allows one to better target intended ternary alloy compositions. Notably, the thickness of CdO and ZnO deposited by each pulse is on the order of the lattice constant of each compound, which suggests that the alternating pulse strategy may allow for enough intermixing and interdiffusion so as to not allow significant compositional gradients in the film growth direction.

Compositional maps for the ternary $Cd_xZn_{1-x}O$ alloy growth runs are presented in Figure 3.3 along with photographs of the CZO_05–06 samples and a substrate map indicating the naming convention for individual sample positions. No data was gathered on the left and right edges of the substrates for CZO_04 and CZO_08 samples. Generally, for each sample the Cd content increases from the top of each substrate to the bottom, and there is a smaller compositional gradient from left to right. As mentioned previously, the stacked configuration of the cathodes likely accounts for this variation. While the separation of the cathodes is small compared to the size of the macroparticle filter entrance, small variations in the plasma direction as it enters the solenoid appear to influence the spatial variation in composition in the growing film. The photographs of the films from the CZO_05-06 growths indicate that the changing Cd content of the samples systematically decreases the absorption edge, up to about $x \sim 0.7$. The compositional variation among high Cd-content growth runs (CZO_07–CZO_09) is less than that of the lower Cd-content alloys. This is also illustrated by the bunching of the compositional data in Figure 3.2, although the reason for this behavior is not immediately clear. The compositional maps in Figure 3.3 reveal one additional source of composition variation, which is that some samples on the left side ("a" samples) are deficient in oxygen by 2–3%. A likely factor contributing to this phenomenon is the directional flow of O_2 gas into the chamber. For this reason, and because films along the vertical middle of the substrates were thicker than those on the sides, all samples analyzed in Chapters 4 and 5 are taken from the middle third of the substrate.

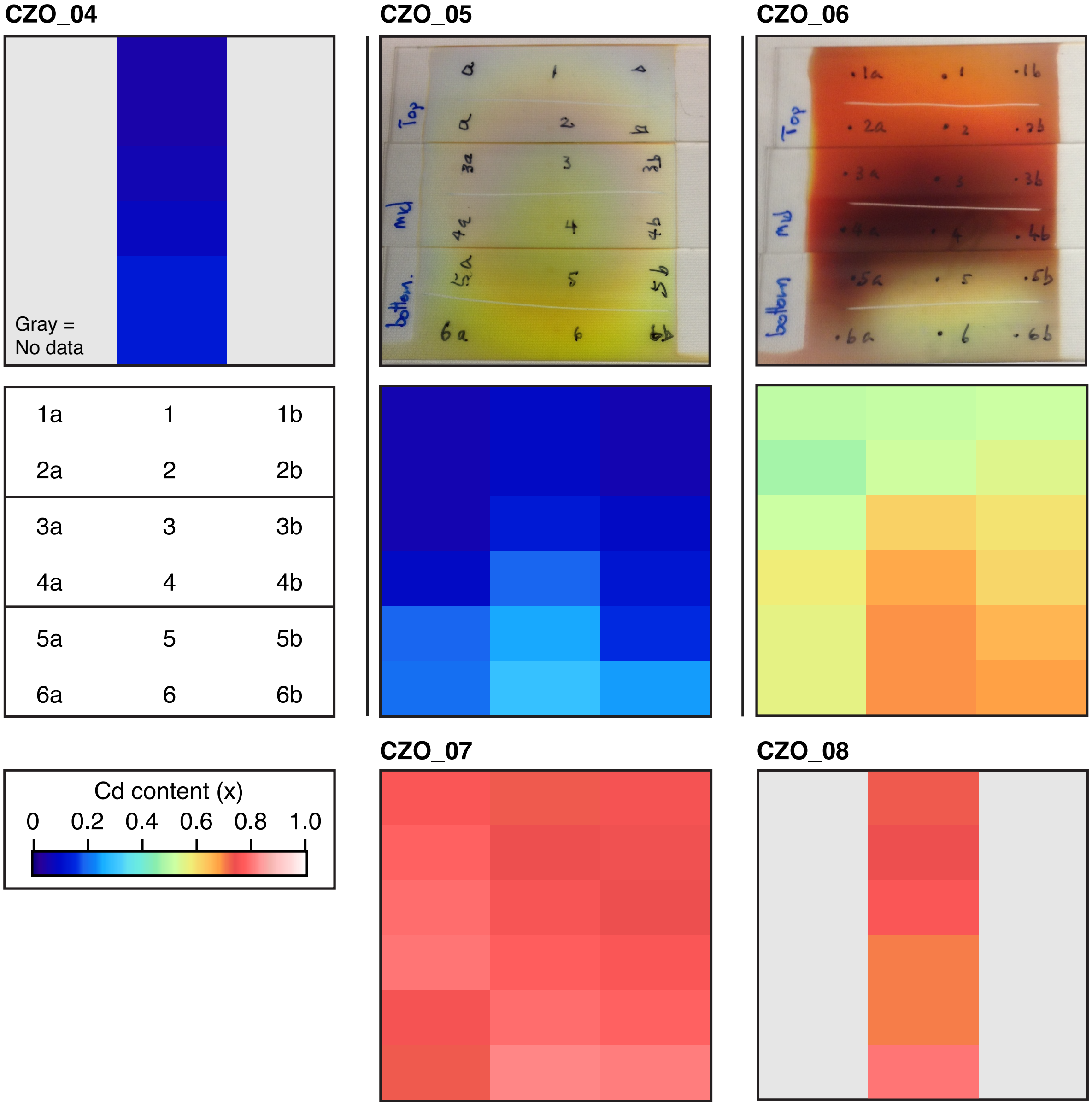

Figure 3.3: Combinatorial growth of $Cd_xZn_{1\text{-}x}O$ by PFCAD. Compositional maps from RBS data reveal variation in the Cd content over the 3 in× 3 in. growth area. Photographs of the CZO_05 and CZO_06 substrates show the spatial variation in the optical absorption edge from gradients in Cd content.

Chapter 4

Correlated structural, optical, and electrical properties of $Cd_xZn_{1\text{-}x}O$

This chapter presents the structural, electrical, and optical characterization of $Cd_xZn_{1\text{-}x}O$ thin films grown by PFCAD on glass substrates. The properties are analyzed with regards to the two phase regimes that are observed to split the composition range into two distinct alloy systems with different property trends. The structure and phase of the films is analyzed by X-ray diffraction (XRD) in Section 4.1. The room-temperature electrical properties are investigated by Hall effect measurements in Section 4.2. Optical absorption (Section 4.3) and photoluminescence (Section 4.4) spectroscopies are then used to characterize the optical properties of the alloys. Finally, Section 4.5 combines the results of the electrical and optical characterization to determine the intrinsic, carrier-free direct bandgap E_g of each alloy, taking into account carrier-induced shifts in the optical absorption edge.

4.1 Structural characterization by X-ray diffraction

The structural properties of $Cd_xZn_{1\text{-}x}O$ thin films were investigated using standard powder X-ray diffraction (XRD) techniques, with Cu K_α radiation and a Ni foil K_β filter. The symmetric 2θ scans of the powder diffraction method probe out-of-plane lattice constants. For thin film samples, particularly those that are polycrystalline, this setup allows one to quickly probe the phase, lattice constant, and texture (preferred orientation) of the films. The reduced dimensionality of thin films (either thickness or crystallite size of polycrystalline materials) leads to peak broadening in 2θ. The full width at half max (FWHM) β (in radians, and corrected for instrumental broadening effects) can be related to the crystallite size or thickness (in the case of single crystals) τ by the Scherrer equation

$$\tau = \frac{K\lambda}{\beta \cos\theta}, \tag{4.1}$$

where K is a shape factor (typically 0.9), λ is the X-ray wavelength in Å, and θ is half the detector angle [142].

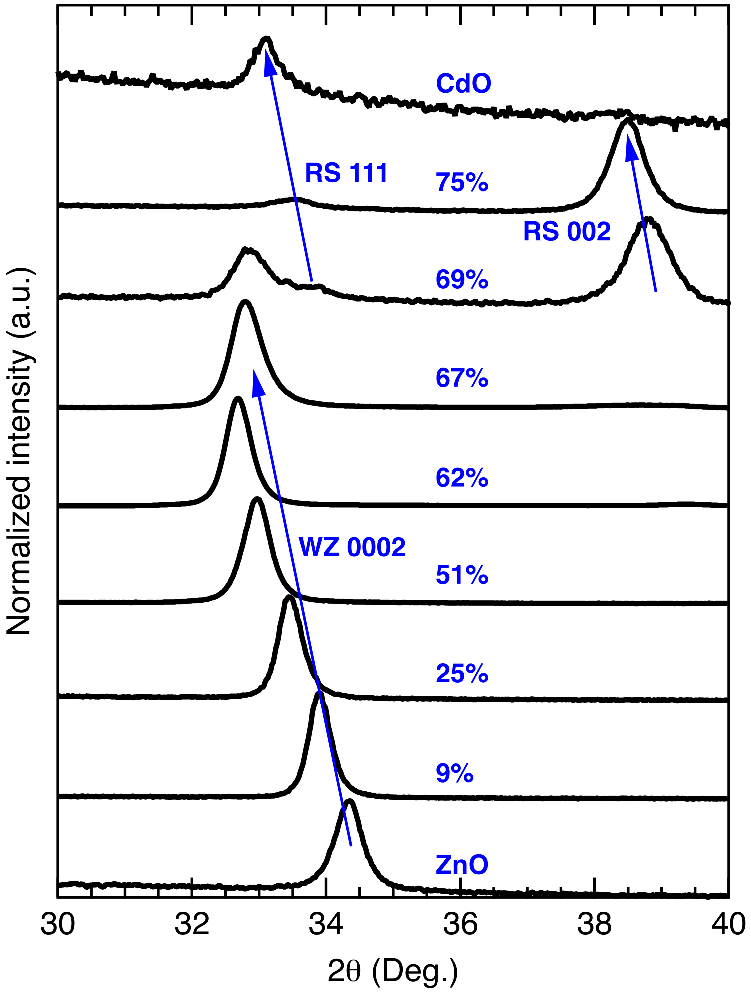

Figure 4.1: XRD patterns of $Cd_xZn_{1\text{-}x}O$ films across the composition range. The polycrystalline films are predominately {0002}-textured wurtzite (WZ) phase at compositions $0 < x < 0.67$; at higher Cd content, the films are rocksalt (RS) phase. The emergence of a small volume fraction of RS phase is observed in WZ-dominant samples $0.60 < x < 0.67$. Samples at the structural transition ($x = 0.69$) exhibit either predominately WZ or RS with a small volume fraction of the other phase present.

Figure 4.1 shows 2θ XRD scans of selected samples across the composition range. All films are polycrystalline with an average $\tau \sim 20$ nm. All films are shown to have a preferred texture, as only the WZ 0002 and RS 002 reflections (and their higher order peaks) are observed. At compositions $0 < x < 0.69$, the films have the WZ crystal structure and {0002} texture. The reduction in the WZ 0002 diffraction peak angle (from $2\theta \sim$34.5 to 33°) with increasing Cd content corresponds to the increase of the WZ c-axis from 5.2 Å ($x = 0$)

to 5.46 Å ($x = 0.67$). The emergence of a small volume of RS phase is observed in WZ-dominant samples with $0.60 < x < 0.67$. Around $x = 0.69$, a structural transition from WZ to RS takes place; samples at this composition were mixed phase and varied from primarily WZ to primarily RS in structure, with a small volume of the other phase present. At alloy compositions above $x = 0.69$, the films were RS in structure with preferred {002} orientation, while the final endpoint CdO exhibited a {111} texture.

Although these films were deposited on amorphous substrates, the structural properties of $Cd_xZn_{1-x}O$ alloys grown by PFCAD are comparable to those of films grown by other methods on crystalline substrates [100, 114, 111]. This is the first report of $Cd_xZn_{1-x}O$ films deposited on amorphous substrates.

4.2 Electrical characterization

The mobility μ and electron concentration n of each sample can be determined by carrying out Hall effect and resistivity measurements using the van der Pauw geometry for contact placement. The van der Pauw technique is a common four-contact method that can be used to measure the sheet resistance of a sample of arbitrary geometry and uniform thickness. One standard electrical contact arrangement (which is the one used in this study) places contacts at the corners of a square sample. Current is applied between two contacts and voltage is measured between the other two contacts. The process is repeated for all combinations of contacts and the sheet resistance R_s can be calculated using the approach described in Ref. [143]. The resistivity ρ can then be calculated from R_s using Equation 1.1 if the film thickness is known. The individual contributions to ρ from μ and n are separated by additionally carrying out Hall effect measurements in the presence of a magnetic field normal to the film surface. Further information involving this experimental setup and the theory of Hall measurements can be found in Ref. [29].

The room-temperature electrical properties were determined using an Ecopia HMS3000 Hall effect system with a 0.6 T magnet. Suitable contact was made to the samples using spring-loaded gold contacts, as all samples exhibited linear IV characteristics in the $> 1\ mA$ current range without the addition of pressed or evaporated metal contacts. The electrical properties of the alloys are summarized in Figure 4.2. Room-temperature Hall effect and resistivity measurements reveal that electron concentration, shown in Figure 4.2a, rises gradually with increasing Cd content across the WZ composition regime, from $n \sim 2 \times 10^{19}$ cm^{-3} at $x = 0$ to $n \sim 2 \times 10^{19}$ cm^{-3} at $x = 0.67$. The electron concentration remains nearly constant in the RS regime. The mobility, shown in Figure 4.2b, increases slightly with Cd content for WZ-structured alloys, from $\mu \sim 15$ cm^2/Vs at $x = 0$ to $\mu \sim 30$ cm^2/Vs at $x = 0.67$. An abrupt rise in the mobility, to $\sim$ 90 cm^2/Vs, is observed alongside the transition to the RS structure at $x \sim 0.69$. This step-like increase in the mobility can be attributed to the difference in the static dielectric constants ϵ_r of the endpoint binary compounds. Nominally undoped WZ-ZnO thin films ($\epsilon_r = 7.5 - 9$) [7] exhibit an electron mobility of $15 - 30$ cm^2/Vs, while that of RS-CdO films ($\epsilon_r = 21.9$) [19] is typically $100 - 200\,$cm^2/Vs. The large static

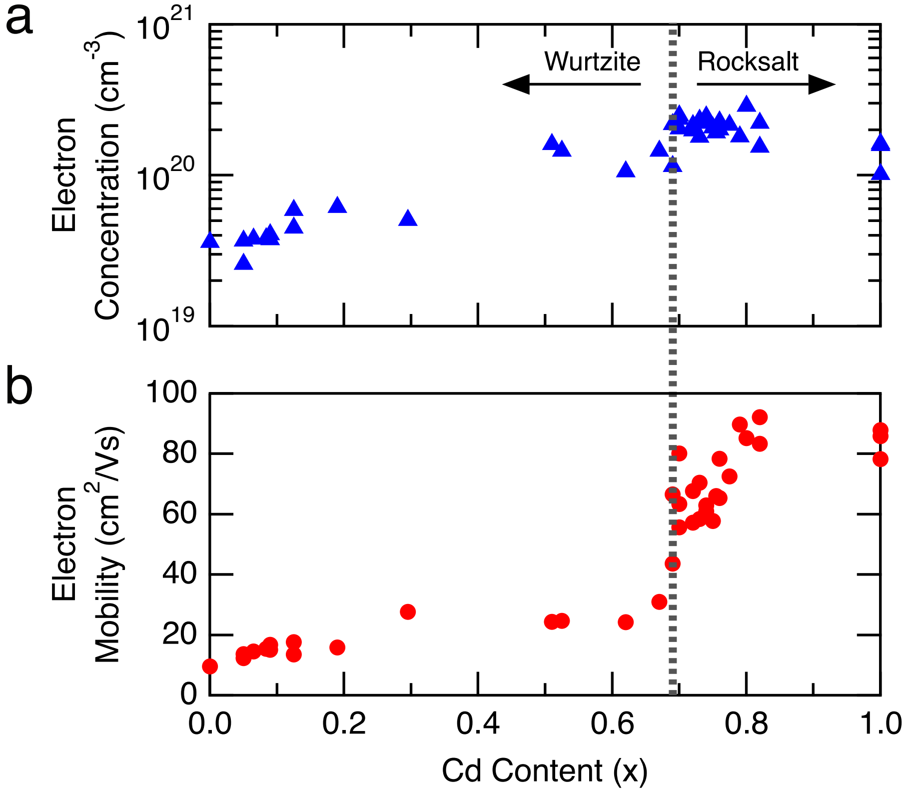

Figure 4.2: Electrical properties of $Cd_xZn_{1\text{-}x}O$ alloys as measured by room-temperture Hall effect. Room-temperature Hall effect measurements were used to determine the (a) free electron concentration and (b) electron mobility of $Cd_xZn_{1\text{-}x}O$ films as a function of Cd content.

dielectric constant of CdO leads to more effective screening of ionized impurities and higher electron mobility, a phenomenon that likely extends to the RS-phase alloys as well.

This unusual behavior of the electron mobility indicates negligible alloy disorder scattering, a feature expected for alloys with weak composition dependence of the conduction band edge position. Indeed, as will be shown in Chapter 5, the conduction band minima of the alloys across both the WZ and RS phase regimes are relatively constant. The consequences of this effect on the mobility of $Cd_xZn_{1\text{-}x}O$ films are explored in Section 5.5.

4.3 Optical absorption spectroscopy

Optical absorption spectroscopy measures transmission (and optionally reflection) characteristics of materials as a function of photon wavelength or energy[1]. The energy-dependent absorption coefficient $\alpha(E)$ is sensitive to allowed optical transitions between energy states in the material, represented by the joint optical density of states. $\alpha(E)$ is particularly sensitive to interband transitions, both direct and indirect, between the filled valence and unfilled conduction bands. In theory, optical absorption spectroscopy allows one to distinguish between indirect and direct transitions. For an intrinsic semiconductor with band edges that have parabolic densities of states, absorption across a direct-bandgap E_g^{dir} can be described by an $E^{1/2}$ dependence where

$$\alpha(E) = \alpha_o(E - E_g^{\text{dir}})^{1/2}, \tag{4.2}$$

where E is the incident photon energy $h\nu$ and α_o is a materials-dependent absorption constant. Indirect transitions will show an E^2 dependence. For this reason it is customary to extract E_g from $\alpha^2(E)$ vs. E plots and E_g^{ind} from $\sqrt{\alpha(E)}$ vs. E plots in simple cases. High electron concentrations require one to take into account carrier effects, however, modifying this simple approach. In the case of $\mathrm{Cd_xZn_{1\text{-}x}O}$, the bandgap can be found by modeling the absorption to take these free-carrier effects into account (Section 4.5). Appendix Section A.4 further discusses this technique and compares it with a more straightfoward approach based on Equation 4.2.

The simplest approach to calculating the absorption coefficient $\alpha(E)$ for a film of thickness d from the experimentally determined transmittance $T(E)$ and reflectance $R(E)$ spectra is to solve Beer's law of absorption

$$T(E) = I_o(E)\exp(-\alpha d), \tag{4.3}$$

subtracting the reflected light $R(E)$ from the incident light I_o such that

$$T(E) = [1 - R(E)]\exp(-\alpha d), \tag{4.4}$$

assuming that the total intensity of reflected, transmitted, and absorbed light is equal to the incident intensity, normalized to $I_o = 1$. Back-reflection from the film-substrate interface is not considered here, and as such this model assumes only single-pass absorption[2]. Solving Equation 4.4 for α, the resulting (energy-dependent) optical absorption coefficient can be found from the experimental data by the equation

$$\alpha(E) = -\left(\frac{1}{d}\right)\ln\left[\frac{T(E)}{1 - R(E)}\right]. \tag{4.5}$$

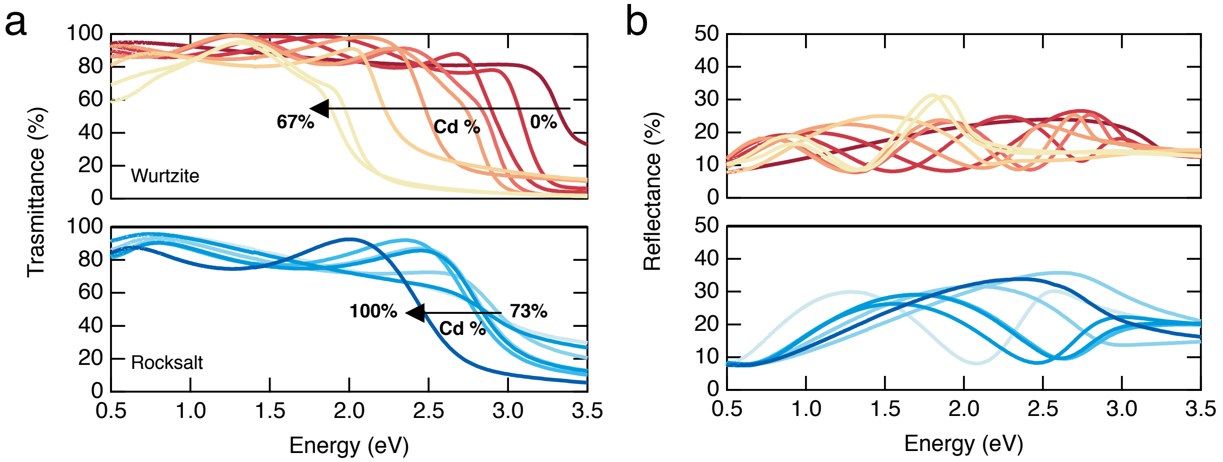

Figure 4.3: (a) Transmittance and (b) reflectance spectra of WZ (upper panels) and RS (lower panels) Cd$_x$Zn$_{1-x}$O fims on glass substrates.

4.3.1 Optical absorption properties of Cd$_x$Zn$_{1-x}$O

The transmission and reflection properties of the films were measured using a Perkin-Elmer Lambda 950 UV-Vis spectrometer in the spectral range of $\lambda = 350 - 2500$ nm. Transmission data was taken using the standard transmission optics of the instrument and reflectance was recorded using the universal reflectance analyzer. Reflectance data was collected at 8° from the direction of the surface normal. A glass reference substrate was placed in the second reference beam of the instrument for transmission measurements.

The transmittance and reflectance spectra (presented here in units of energy $h\nu \approx 0.5$–3.5 eV) for the Cd$_x$Zn$_{1-x}$O films are shown in Figure 4.3a and Figure 4.3b, respectively. For WZ films (upper panels), the high-energy transmittance cutoff decreases in energy with the substitutional incorporation of Cd in ZnO up to $x = 0.69$; for higher Cd-content RS films (lower panels), the transmittance cutoff occurs at higher energies than the highest Cd-content WZ samples. CdO has a lower energy edge in its transmittance spectrum compared to RS-Cd$_x$Zn$_{1-x}$O alloys. The periodic features in the reflectance spectra (which can also be seen in the transmittance spectra), are Fabry-Pérot oscillations and are a well-known interference effect in thin films [145]. The periodicity of these fringes is dependent on the thickness, surface irregularities, and index of refraction of each film; as such there are no clear trends seen in the data. Nonetheless, from Equation 4.5 the reflectance data is quite useful for calculating $\alpha(E)$. At higher electron concentrations the plasma reflection edge can be clearly seen in reflectance measurements over this energy range, but in this case, where

---

[1] The introductory text by Pankove [144] provides an excellent overview of the basic optical properties of semiconductors.

[2] Ref. [145] offers a more in-depth treatment of modeling the absorption that considers reflection of multiple interfaces.

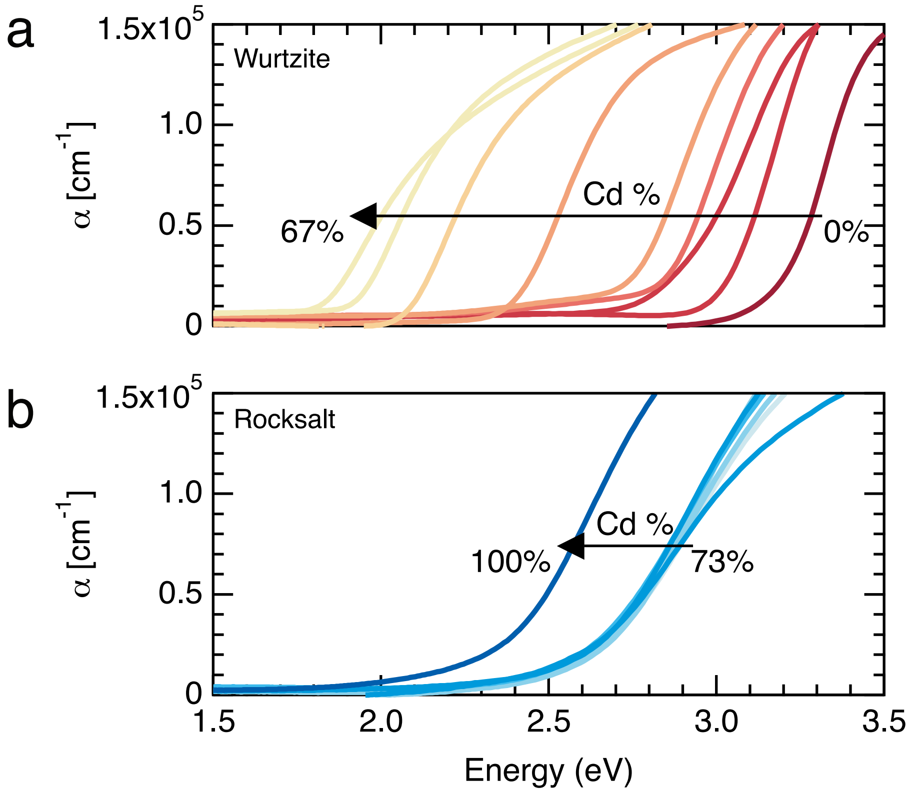

Figure 4.4: Optical absorption coefficients as a function of photon energy of $Cd_xZn_{1\text{-}x}O$ films with (a) wurtzite structure ($0 < x < 0.69$) and (b) rocksalt structure ($0.69 < x < 1$).

$n \sim 10^{20}$ cm^{-3} (refer to Figure 4.2) the plasma edge is located further into the IR.

Figure 4.4 presents a summary of the optical absorption of $Cd_xZn_{1\text{-}x}O$ films. Following Equation 4.5, the optical absorption coefficient α as a function of photon energy of WZ and RS alloys was determined by taking both transmission and reflection measurements into account.

As shown in Figure 4.4a, the incorporation of Cd into WZ-ZnO ($E_g = 3.3\ eV$) reduces the absorption edge energy E_g^{opt} from the ultraviolet through the entire visible range. The absorption spectra for Cd-rich alloys are shown separately in Figure 4.4b. At $x = 0.73$, there is an abrupt increase in the E_g^{opt} relative to that of the $x = 0.67$ alloy, corresponding to the transition to the RS phase. From $0.73 < x < 0.83$, E_g^{opt} remains relatively constant, but remains higher than that of pure CdO.

This data, along with the Hall effect data from Section 4.2, will be used to calculate the values of the intrinsic, direct bandgaps of $Cd_xZn_{1\text{-}x}O$ alloys in Section 4.5.

4.4 Photoluminescence spectroscopy

Photoluminescence (PL) spectroscopy measures the emission of photons from radiative recombination processes in a material following an absorption process. After the photoexcitation of electrons many radiative and non-radiative relaxation processes can occur, each with different time constants and at different energies. The emission from fundamental optical transitions, such as band-to-band recombination of photoexcited electrons across a direct bandgap, is sensitive to structural quality and phonon interactions, both of which broaden the emission energies of observed transitions. Both of these interactions, as well as energy states from impurities in the bandgap, provide alternate routes for non-radiative recombination. The energy- and momentum-relaxation of carriers to the band edges is a fast process with respect to the total carrier lifetime. In a direct-bandgap semiconductor the band edge positions offer charge carriers an opportunity to radiatively recombine across the bandgap, provided non-radiative processes do not dominate; in an indirect semiconductor the carriers relax to band edge positions at different points in k space, and non-radiative recombination processes dominate. A more complete background on luminescence behavior in semiconductors can be found in Refs. [15] and [144].

In this section, PL will be used to probe the direct bandgaps of $Cd_xZn_{1-x}O$ materials using above-bandgap laser light. Room temperature photoluminescence (PL) spectra were measured using a 30 mW, 325 nm HeCd excitation laser and a Hamamatsu R928 photomultiplier tube detector. Data were recorded over a wavelength range of 350-820 nm with a filter in place to block the 2nd-order, 650 nm laser line. The raw data were weighted by dividing each data point by the instrument response function of the PMT detector to account for its variable spectral sensitivity. The instrument function data, along with additional temperature-dependent measurements, are provided in Appendix Section A.6.

4.4.1 Room-temperature photoluminescence of $Cd_xZn_{1-x}O$

The normalized PL spectra are shown as a function of photon energy in Figure 4.5. The incorporation of Cd in WZ-ZnO reduces the energy of the strongest photoluminescence peak, which is presumed to be the result of band-to-band recombination, from 3.27 eV at $x = 0$ to 1.75 eV at $x = 0.69$. The FWHM of the band-edge PL at first increases along with Cd content, from 130 meV ($x = 0$) to 260 meV ($x = 0.08$), but then decreases to 160 meV for the highest Cd-content WZ sample ($x = 0.69$). The peaks with larger FWHM are likely the convolution of the band-edge PL with another peak. In lower Cd-content samples, a broad, sub-bandgap feature around 2.5–2.7 eV is observed, indicative of defect luminescence from mid-gap defect states [6]. As will be seen in Section 4.5.2, the band-edge PL is significantly redshifted relative to E_g^{opt} in samples with high n. Redshifts between absorption and emission are generally referred to as Stokes shifts. No detectable band-edge luminesce is seen in the higher Cd-content RS-$Cd_xZn_{1-x}O$ alloys or in CdO, indicating that the indirect gap of CdO may be maintained throughout the RS alloy range. Notably, PL at 1.75 eV is observed

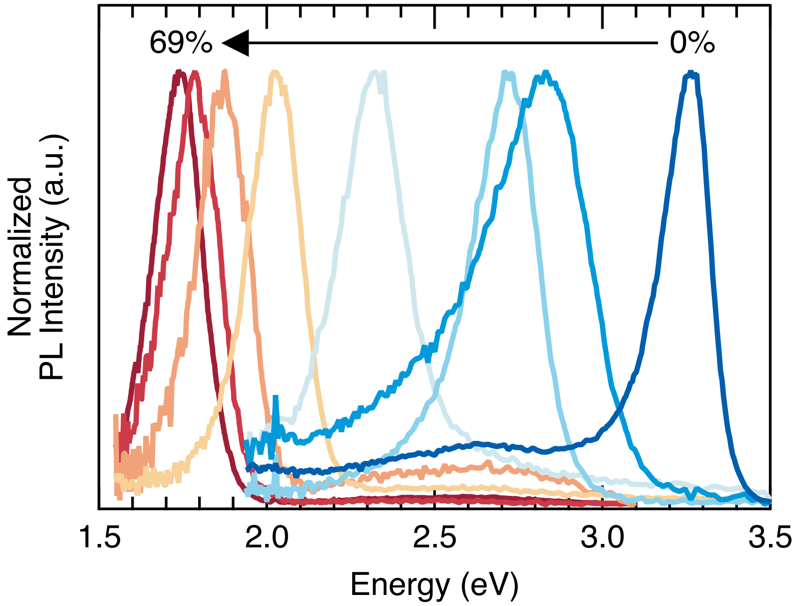

Figure 4.5: Normalized photoluminescence spectra of wurtzite $Cd_xZn_{1\text{-}x}O$ phase films measured at room temperature. The band-to-band PL decreases in energy from 3.27 eV (ZnO) across the visible spectral range to 1.75 eV ($x = 0.69$). No visible band-edge luminescence is seen in the higher Cd-content RS-$Cd_xZn_{1\text{-}x}O$ alloys or in CdO.

from mixed phase samples on either side of the structural transition that have an average composition of $x \sim 0.69$.

The combinatorial aspect of the PFCAD growth, discussed in Chapter 3, results in samples with systematic gradients in Cd-content from one side of the substrate to the other. The photoluminescence properties of a sample with average Cd content of $x = 0.69$ is shown in Figure 4.6. A photograph of the sample, (field of view: ~ 0.5 cm$\times \sim 1$ cm) reveals the differences in the optical absorption edge betwee the two phases. Regions of both low E_g^{opt} (top) and high E_g^{opt} (bottom) correspond to locations of the higher-Cd-content RS-dominant phase and the lower-Cd-content WZ-dominant phase, respectively. In this way, the abrupt phase-transition with Cd-content can be seen from the spatial gradient of Cd content.

While the E_g^{opt} of the mixed phase samples near $x \sim 0.69$ increases abruptly, indicating change in the dominant phase, a PL peak near 1.8 eV persists even for compositions with an apparently high volume fraction of the larger-E_g^{opt} RS phase. The energy of this WZ-PL is slightly higher than that of the highest Cd-content sample in Figure 4.5, indicating that the WZ phase of the inclusions has slightly lower Cd-content than the WZ-majority phase. Mixed phase samples that are dominated by the high-electron-concentration RS phase and that exhibit photoluminescence—likely due to embedded nanoparticles of WZ-phase material—are an attractive mesoscale system that warrants further investigation.

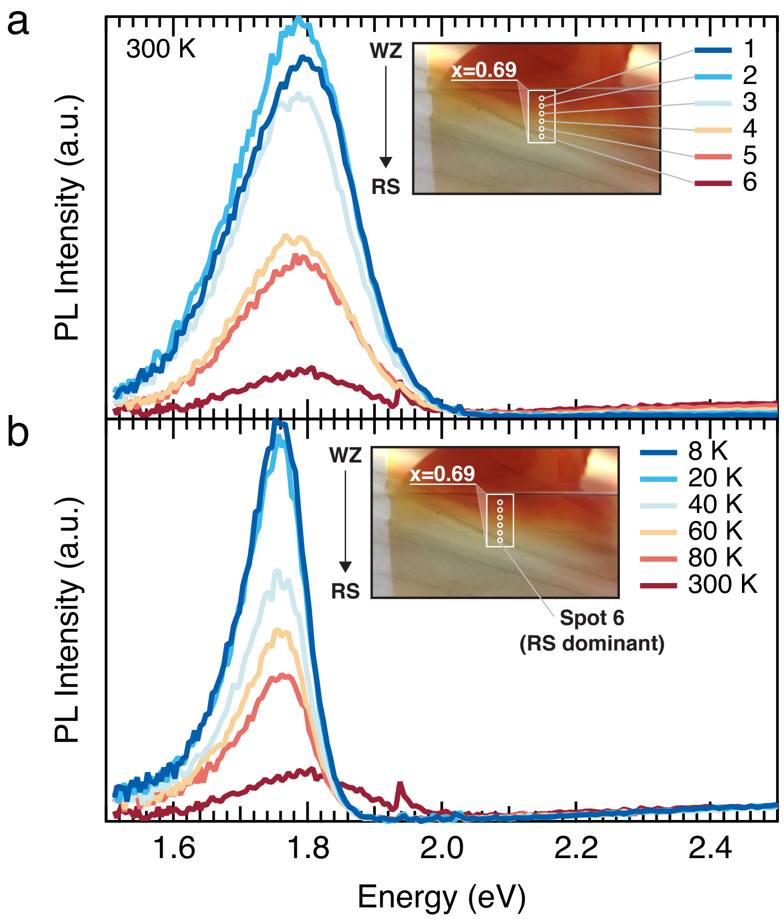

Figure 4.6: Non-normalized PL of phase-separated $Cd_xZn_{1\text{-}x}O$ sample with $x \sim 0.69$, along with photograph of the sample (field of view: ~ 0.5 cm$\times \sim 1$ cm). (a) Spatial variation of PL at spots 1 (dominant WZ phase, low-E_g^{opt}) to 6 (dominant RS phase, high-E_g^{opt}). PL at 1.8 eV persists even in the RS phase, likely due to inclusions of luminescent WZ phase. (b) Temperature-dependent PL spectra at spot 6 shows that at temperatures < 80 K, luminescence from this WZ-phase is strongly enhanced and slightly blueshifted, as is typical for band-to-band emission.

4.5 Bandgap determination of $Cd_xZn_{1\text{-}x}O$ alloys

4.5.1 Bandgap renormalization and carrier filling effects

As mentioned in the introduction to Section 4.3, for samples with high electron concentrations the direct bandgap cannot be determined directly by using conventional linear fits to α^2 vs E plots. While this conventional approach can be modified to incorporate carrier-induced changes as rigid shifts to the extracted value of E_g^{opt} (a procedure discussed in more detail in Section A.4), it is commonly misused for the analysis of TCO materials [146]. Instead, the intrinsic, carrier-free gap E_g can be found by modeling the optical absorption data to account for carrier effects [147, 148].

The energy-dependent absorption coefficient $\alpha(E)$ can be calculated as the convolution of the Fermi-level shifted absorption with a Gaussian function of width Δ to account for experimental broadening so that

$$\alpha(E) = \frac{1}{\Delta\sqrt{\pi}} \int_{-\infty}^{\infty} \alpha_0 (E' - E_g^o)^{\frac{1}{2}} \left[1 + \exp\left(\frac{E_F - E'}{k_B T}\right)\right]^{-1} \times \exp\left[-\left(\frac{E' - E}{\Delta}\right)^2\right] dE', \quad (4.6)$$

where α_0 is an absorption constant and E_g^o is the Burstein-Moss-corrected direct bandgap, as yet uncorrected for the carrier-induced renormalization shifts discussed below. E_F is the Fermi level relative to the conduction-band minimum and represents the value of the Burstein-Moss shift. E_F can be determined from the measured Hall effect electron concentration n, by the integral equation (Equation 1.6) presented in Chapter 1

$$n(E_F) = \frac{1}{3\pi^2} \int_0^{\infty} \frac{\exp\left(z - \frac{E_F}{k_B T}\right)}{\left[1 + \exp\left(z - \frac{E_F}{k_B T}\right)\right]} k^3(z)\, dz, \quad (4.7)$$

where $z = E/k_B T$ [50, 51, 52]. E is the electron energy relative to the conduction-band edge ($z = 0$), and the wavevector k is found using the non-parabolic dispersion as derived from Kane's two-band $k \cdot p$ model (also presented as Equation 2.2) [149]

$$E(k) = \frac{\hbar^2 k^2}{2m_o} - \frac{E_g}{2} + \left(\sqrt{\left(\frac{E_g}{2}\right) + \frac{E_g \hbar^2 k^2}{2m_e^*}}\right). \quad (4.8)$$

As is the case with the III-V analog of this system, $In_xGa_{1-x}N$ [150], the effective mass of an electron m_e^* at the band edge is assumed to be proportional to the bandgap following the expression

$$\frac{m_e^*}{m_o} \approx \frac{E_g}{E_p}. \quad (4.9)$$

An interaction energy (E_P) of 8.1 eV leads to good agreement with the literature values for the binary endpoints CdO ($E_g = 2.18\ eV$, $m_e^* = 0.21m_0$) [84] and ZnO ($E_g = 3.3\ eV$, $m_e^* = 0.29m_0$) [151]. Assuming the constant $E_P = 8.1$ eV in the entire composition range one can assume a reduction of the value of the band edge electron effective mass with increasing Cd content in the WZ phase. This could be an additional effect responsible for the gradual increase of the electron mobility with increasing Cd content shown in Figure 4.2.

In order to determine the intrinsic, carrier-free bandgap of each alloy, one must also take into account two additional carrier-induced shifts: the upward energy shift of E_g^{opt} due to the dispersion of the valence band, renormalization effects due to electron-electron and electron-ion interactions.

The magnitude of these normalization effects is calculated according to the methods developed by Berggren and Sernelius [52] and used in Refs. [50, 51] for intentionally-doped GaAs and nominally undoped CdO, respectively. The paper by Walsh, Da Silva, and Wei [53] illustrates how these effects change the band structure of the prototypical TCO material In_2O_3. Empirically, these effects are often seen to follow $n^{1/3}$ dependence, in contrast to the $n^{2/3}$ dependence of E_{BM} for parabolic semiconductors [152].

As the concentration of electrons in the conduction band increases the charge carriers interact and begin to exhibit correlated behavior. This ordering lowers the energy of the conduction band states by a value E_{e-e} that depends on n via the Fermi wavevector k_F, such that

$$E_{e-e} = -\frac{2e^2 k_F}{\pi \epsilon_r} - \frac{e^2 \lambda_F}{2\epsilon_r}\left[1 - \frac{1}{4}\tan^{-1}\left(\frac{k_F}{\lambda_F}\right)\right], \tag{4.10}$$

where λ_F is the Thomas Fermi screening parameter

$$\lambda_F = -2\left(\frac{k_F}{\pi a_B}\right)^{1/2}, \tag{4.11}$$

and a_B is the Bohr radius of an electron in the material, calculated as $a_B = a_H(\epsilon_r/m_e^*)$, where a_H is the Bohr radius of hydrogen.

The Coulombic interaction between electrons and ionized impurities leads to a separate concentration-dependent decrease in the energy of the conduction band

$$E_{\text{ion}-e}(n) = -\frac{e\hbar}{2}\left[\frac{\pi^3 n}{\epsilon_r m_e^*}\right]^{1/2}. \tag{4.12}$$

The position of E_{FS} is similarly lowered by this electrostatic interaction although it is unaffected by electron correlation effects.

One additional carrier-induced shift discussed in Chapter 1 that must be taken into account is the blueshift in absorption due to the valence band curvature. For ZnO (and other materials with valence bands with downward curvature away from the VBM), the magnitude of this shift simply follows the dispersion relation

$$E_{VB} = \frac{\hbar^2 k_F^2}{2m_h^*}. \tag{4.13}$$

The valence band dispersion and dielectric constant for WZ and RS alloys were assumed to be unchanged from the binary ZnO and CdO endpoints: for WZ alloys the hole effective mass is assumed to be $0.59m_0$ [6]; for RS alloys the valence band is assumed to be flat [80]. Since these additional carrier-induced effects can be applied as rigid shifts to the bands, they are added to or subtracted from E_g^o, found by fitting the absorption model (Equation 4.6) to experimental data in Figures 4.4a and 4.4b. This procedure yields the intrinsic, carrier-free gap E_g.

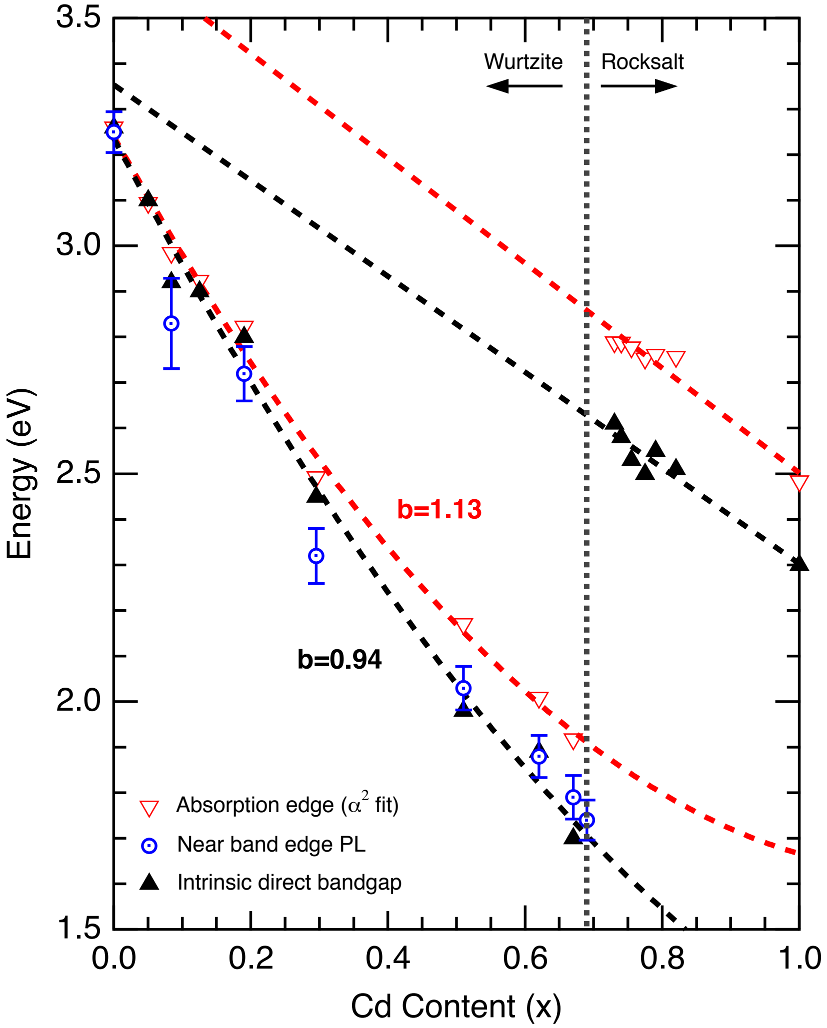

Figure 4.7: The compositional dependence of the band-to-band photoluminescence energy, the direct-gap absorption edge E_g^{opt}, extrapolated from linear α^2 vs. energy plots, along with the carrier-free, intrinsic gap E_g determined by comparing optical absorption spectra to a model that accounts for carrier filling and carrier-induced renormalization effects.

4.5.2 Determination of the carrier-free, direct bandgap

Figure 4.7 presents the compositional dependence of the band-to-band photoluminescence energy as well as a comparison of the direct-gap absorption edge E_g^{opt} found by extrapolating linear fits to α^2 vs E plots with the intrinsic gap E_g found by the absorption fitting procedure described in Section 4.5.1. Further discussion of the use (and common misuse) of α^2 vs. E plots is presented in Appendix A.4.

For low Cd-content WZ alloys ($x < 0.30$), where $n \sim 10^{19}$ cm^{-3}, there is good agreement between our absorption model and the standard fitting technique. There is a larger discrepancy, however, at higher Cd-content WZ alloys, where the electron concentration is high ($n \sim 10^{20}$ cm^{-3}). At $x = 0.67$, the direct gap determined by α^2 (1.9 eV) overestimates the intrinsic gap (1.7 eV) by ∼200 meV.

Fitting the intrinsic bandgap of WZ alloys to the standard bowing equation given by Equation 2.4

$$E_g^{\mathrm{WZ-Cd_xZn_{1-x}O}}(x) = (1-x)E_g^{\mathrm{WZ-CdO}} + xE_g^{\mathrm{WZ-ZnO}} - bx(1-x) \tag{4.14}$$

yields a bowing parameter b of 0.94 eV. The extrapolated direct bandgap of the WZ-CdO phase (1.3 eV) falls within the range of values (1–1.5 eV) predicted by first-principle calculations [119, 153] and the bowing parameter agrees well with another report ($b = 0.95$ eV) for WZ-phase $Cd_xZn_{1-x}O$, measured for compositions up to $x = 0.16$ [112].

Similarly, α^2 fitting (with no additional corrections for free carrier effects) significantly overestimates the intrinsic gaps of the high electron concentration RS alloys. Notably, the incorporation of up to $\sim$ 25% Zn in CdO ($x \sim 0.75$) increases the intrinsic gap from $\sim$ 2.3 eV to $\sim$ 2.6 eV. It has previously been demonstrated that when intentionally doped with In or Ga, CdO can achieve an electron concentration $\sim 10^{21}$ cm^{-3} with a mobility exceeding 100 cm^2/Vs. Consequently, the optical absorption edge increases to $\sim$ 3.2 eV with excellent transparency up to 1500 nm [19]. Hence the Cd-rich CdZnO alloys with $\sim$ 300 meV increase in the intrinsic gap that maintain good electrical performance could potentially serve as transparent conductors for devices that utilize a wide range of the solar spectrum (from 340–1400 nm), such as high efficiency triple junction solar cells [19].

In summary, in this chapter the structural, optical, and electrical properties of $Cd_xZn_{1-x}O$ alloys grown by PFCAD have been presented. The carrier-free, intrinsic direct bandgaps of alloys across the full composition range have been found by taking carrier filling and renormalization effects into account when modeling the optical absorption coefficient. The structural mismatch between WZ-ZnO and RS-CdO creates two distinct regimes of optical and electrical behavior. At one end, the wurtzite phase alloys at compositions $0 < x < 0.69$ exhibit a decrease in the absorption edge across the visible spectrum from 3.3 to 1.9 eV along with an increase in electron concentration (from $\sim 10^{19}$ cm^{-3} to $\sim 10^{20}$ cm^{-3}) and a moderate rise in electron mobility as the Cd content increases. A phase transition to the rocksalt structure is observed above $x = 0.69$, along with a drastic step increase in the electron mobility up to 90 cm^2/Vs and an intrinsic gap of 2.6 eV.

This analysis provides a good foundation for the investigations of the changing band offsets presented in the next chapter. Clearly, the bandgaps of $Cd_xZn_{1-x}O$ alloys change significantly with composition, but whether these changes are accommodated by the movement of the conduction band or the valence band is an open question. As noted in Section 2.2, the mobility should be affected by changes in the conduction band minimum (CBM) with changing alloy content. The relatively constant electron mobilities across each phase regime offer some hint that the CBM of the alloys does not vary significantly with composition within a particular phase regime, however.

Chapter 5

Fermi-level stabilization and band-edge energies in $Cd_xZn_{1-x}O$ alloys

5.1 Introduction

As discussed in Section 2.2, many semiconductor properties as well as the the optimal design and performance of semiconductor devices are deeply affected by the position of the band extrema of the semiconductor relative to those of the other materials in the device. The band alignment of the individual constituent materials on an absolute scale is of paramount importance in predicting the behavior of electrical junctions that form when the materials are connected. According to the amphoteric defect model (see Section 2.1.1), the positions of the band extrema on an absolute scale further affect the electrical behavior of native point defects and doping limits.

In this chapter, the changes in the optical bandgap of $Cd_xZn_{1-x}O$ films (presented in Section 4.5.2 and Figure 4.7) are connected to the independent movement of the CBM and VBM across the composition range. The compositional shifts in the band-edge positions have previously been studied using first-principles calculations [119, 154], but to date there is little experimental evidence to confirm these electronic-structure calculations beyond one report of $Cd_xZn_{1-x}O$ alloys up to $x = 0.075$ [125].

Here, the $Cd_xZn_{1-x}O$ band offsets are studied by three complementary techniques. In Section 5.2 ion irradiation is used to measure the position of the conduction band minimum (CBM) by Fermi-level stabilization, following the ADM framework of Section 2.1.1. In Section 5.3 X-ray photoelectron spectroscopy (XPS) is used to probe the valence band and core levels. Section 5.4 presents the results of soft X-ray absorption and emission spectroscopy (XAS/SXE), taking into account core level shifts revealed in XPS. A summary of the band offsets found by the three aforementioned techniques is presented in Section 5.5. The results show good agreement among the three techniques, offering a self-consistent picture of the

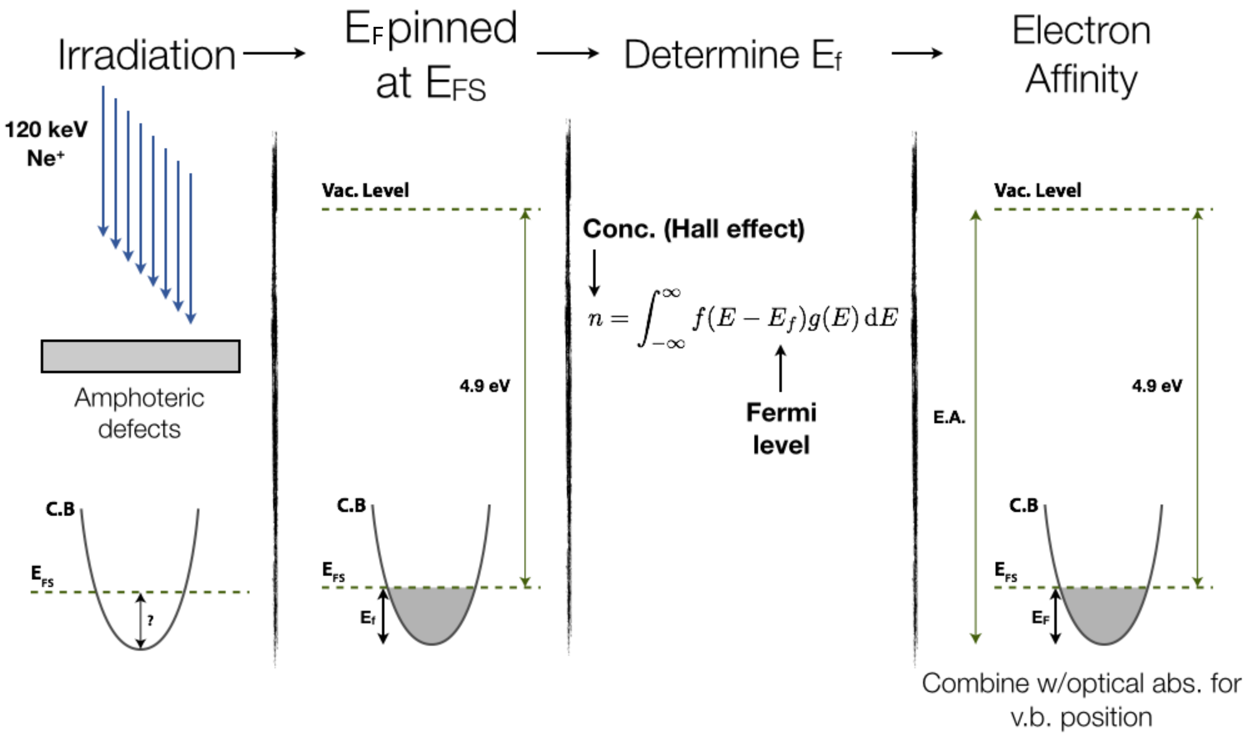

Figure 5.1: Summary of Fermi-level stabilization experiment to determine the electron affinity E_A for $Cd_xZn_{1\text{-}x}O$ alloys. Amphoteric point defects are generated in $Cd_xZn_{1\text{-}x}O$ films by 120 keV Ne+ ion irradiation, pinning the Fermi level E_F at E_{FS}. The measured free carrier concentration n is related to E_F by Equation 4.7. The total electron affinity E_A is determined by adding E_F to the constant value of E_{FS}.

band alignment as a function of Cd content for both the WZ and RS structure alloys.

The unique band alignments revealed by this work hold significant promise for the design of photoelectrochemical (PEC) devices based on $Cd_xZn_{1\text{-}x}O$ heterojunctions with Si. This concept, along with a schematic for a hypothetical $Cd_xZn_{1\text{-}x}O$-based PEC device, is explored in further detail in Chapter 6.

5.2 Fermi-level stabilization by ion irradiation

As discussed in Section 2.1.1, the charge state as well as the formation energy of native defects in semiconductors is dependent on the position of the Fermi level E_F with respect to E_{FS}, located ~ 4.9 eV below the vacuum level in all semiconductors [65, 66]. As illustrated in 5.1, when intentionally generated via ion irradiation, these electrically active, amphoteric defects move E_F toward E_{FS}, eventually pinning it at that energy; E_F is unaffected by further irradiation. In the case of materials where E_{FS} is close to or inside the conduction band, the pinned value of E_F relative to the CBM is determined by calculating E_F from the measured free electron concentration n using Equation 4.7. In order to calculate the density of states term from the nonparabolic dispersion, both the composition-dependent value of m_e^* calculated using Equation 4.9 and the experimentally determined value of E_g found in Section 4.5.2 are used.

The electron affinity E_A, by extension, can be determined as

$$E_A = E_{\mathrm{FS}} + E_F. \tag{5.1}$$

When combined with the value of E_g, this technique also establishes the energy of the valence band at the Γ-point with respect to the vacuum level at each composition. This method has previously been used to establish the position of E_{FS} in (and therefore the natural band alignment among) a number of elemental and compound semiconductors [66, 155], including the endpoint binary compounds, CdO ($E_A = 5.9$ eV) [51] and ZnO ($E_A = 4.85$ eV) [102], investigated in this study.

Point defects were generated by irradiating films with 120 keV Ne^+ ions in fluence increments of 5×10^{12} cm^{-2}, reaching a final total fluence of 3×10^{13} cm^{-2}. The electron concentration and mobility at each damage fluence was measured by room-temperature Hall effect following the procedures described in Section 4.2. The energy range was selected so that the results could easily be compared to similar Fermi-level stabilization studies carried out on CdO [51] and ZnO [102]. The implantation depth was simulated using the freely available Monte-Carlo-based SRIM ("Stopping Range of Ions in Matter") software. Note that the thicknesses of the films used in this study (100–200 nm) were smaller than the projected range of the Ne^+ ions, ensuring that end-of-range damage was not in the thin film and that defects were generated relatively uniformly in the films. Example SRIM calculations are provided in Section A.7.

5.2.1 Results

The electrical properties as a function of total ion fluence are presented in Figures 5.2 and 5.2b and summarized in Table 5.1. Additional optical absorption data for irradiated samples is presented in Appendix A.7. The electron concentration (Figure 5.2a) of WZ samples with low Cd-content ($x < 0.29$) decreases from $n \sim 10^{19}$ cm^{-3} (as-grown) to $n \sim 10^{18}$ cm^{-3} at saturation (total fluence: 3×10^{13} cm^{-2}). By contrast, the concentration in the WZ sample with $x = 0.56$ does not change appreciably with increasing fluence, and that of the RS samples (dotted lines) increases from $n \sim 1 - 2 \times 10^{20}$ cm^{-3} to a final saturation value of $n \sim 3 \times 10^{20}$ cm^{-3}. The mobility (Figure 5.2b) of each sample decreases with increasing total irradiation dose due to increasing scattering events from the ionized native defects. The resistivity of the pure ZnO sample was too large to provide accurate concentration and mobility values at total ion fluences above 2×10^{13} cm^2/Vs. The last reliably measurable value of the electron concentration, 1.05×10^{18} cm^{-3} (with $\mu \sim 3.2$ cm^2/Vs), agrees well with the saturation value observed in previous experiments [102].

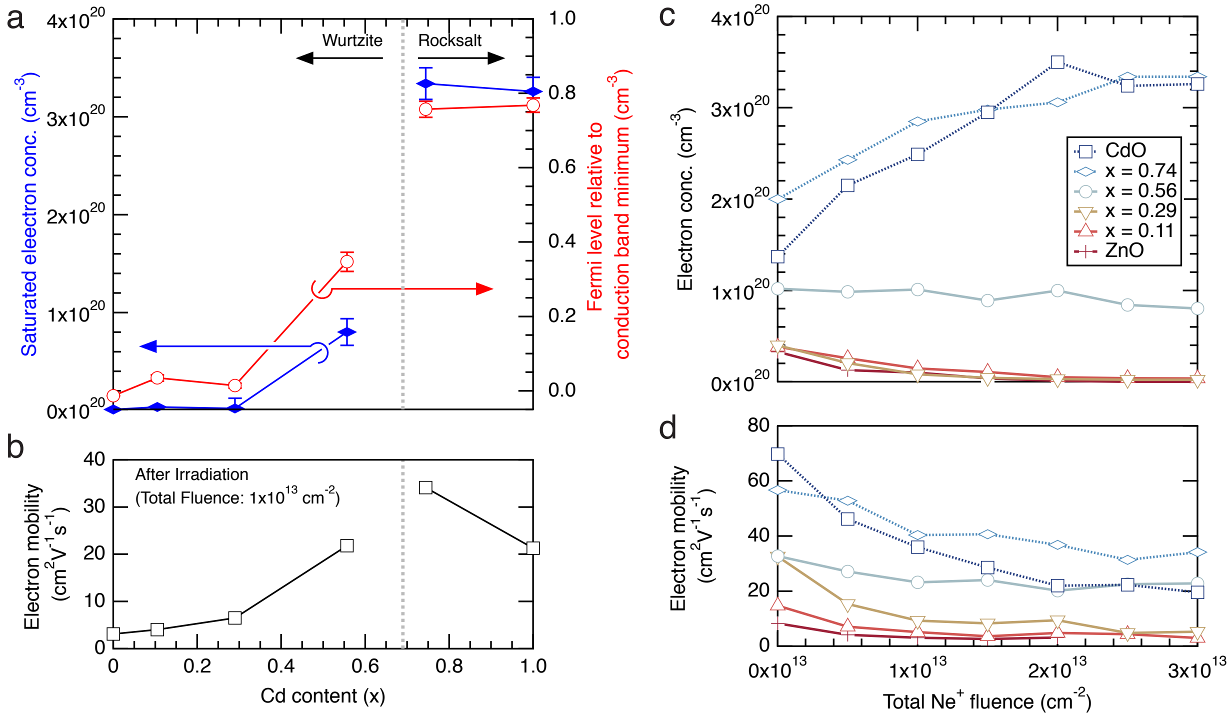

Figure 5.2: Electrical properties of (120 keV Ne^+) ion-irradiated $Cd_xZn_{1\text{-}x}O$ films as a function of irradiation fluence, as measured by room-temperature Hall effect, along with values of n and μ following irradiation as a function of Cd content. (a) Amphoteric point defects generated by ion irradiation move the Fermi level toward E_{FS}, eventually leading to a saturation in the free electron concentration when $E_F = E_{\text{FS}}$. (b) The mobility of each sample decreases with increasing total ion fluence. (c) The saturation value of the electron concentration, along with the corresponding shift in the Fermi level (following Equation 4.7), is constant for WZ films below $x = 0.29$, rises moderately near the phase transition point, and reaches higher values for the RS films. (d) The electron mobility of films following irradiation reaches a maximum for $x = 0.74$.

The composition dependence of the electrical properties of the films following irradiation is shown in Figures 5.2c and 5.2d. As shown in Figure 5.2c and indicated in Table 5.1, the saturated electron concentrations for films with $x < 0.29$ are all close to 10^{18} cm^{-3}. The value of E_F with respect to the CBM (calculated using Equation 4.7) for these concentrations is close to zero, and therefore the CBM lies close to E_{FS} in this composition range (that is, $E_A \approx 4.9$ eV). The saturation concentration of 8.0×10^{19} cm^{-3} for the highest Cd-content WZ film ($x = 0.56$) is significantly higher and indicates that the Fermi level is pinned ~ 350 meV above the CBM (with a corresponding increase in E_A.) For both of the RS samples, the saturated electron concentration indicates a high electron affinity with the CBM of each sample located ~ 0.8 eV below E_{FS}. The electron mobility of the samples

Table 5.1: Summary of ion irradiation experiment to determine Fermi level stabilization energy and electron affinity in $\mathrm{Cd_xZn_{1\text{-}x}O}$ films.

Cd content (x)	n (as-grown) ($\mathrm{cm^{-3}}$)	n (saturation) ($\mathrm{cm^{-3}}$)	μ (at saturation) ($\mathrm{cm^2/Vs}$)	E_F rel. to CBM (eV)	E_A (eV)
0.00	3.28×10^{19}	1.05×10^{18}	3.2	-0.013	4.89
0.11	3.84×10^{19}	1.05×10^{18}	4.1	0.035	4.94
0.29	3.99×10^{19}	2.17×10^{18}	6.5	0.015	4.91
0.56	1.02×10^{20}	8.02×10^{19}	21.8	0.347	5.25
0.74	2.00×10^{20}	3.34×10^{20}	49.4	0.757	5.66
1.00	1.37×10^{20}	3.26×10^{20}	34.1	0.768	5.67

is shown in Figure 5.2d. It is somewhat surprising that maximum electron mobility is not observed at $x = 1$ (pure CdO) but rather in the alloy with $x = 0.74$ given that the saturation concentration is constant throughout the RS range. The reason for this behavior is unclear at present.

Within the framework of the amphoteric defect model, establishing the position of the CBM with respect to E_{FS} also yields valuable information regarding the extent of charge accumulation (or depletion) at surfaces. The surface Fermi level of all samples (both as-grown and irradiated) can be assumed to be pinned at E_{FS}. Additional ion-induced defect generation tends to align the bulk Fermi levels at E_{FS}, attaining a flat band condition. For this reason, as the bulk Fermi level of all $\mathrm{Cd_xZn_{1\text{-}x}O}$ samples is observed to lie close to or above the CBM, downward band bending and electron accumulation are expected at the surface and along internal extended defects of as-grown films. Similarly, the increase in E_A from WZ to RS explains the rise in Hall concentration of as-grown films observed in Section 4.2, as native defects will have a greater tendency to act as donors as the CBM moves below E_{FS}.

5.3 X-ray photoelectron spectroscopy

X-ray photoelectron spectroscopy (XPS) is a technique that relies on the photoelectric effect, the photo-induced ejection of electrons, to probe the filled electronic states of a material. The technique is used to probe both elemental core levels, which commonly undergo slight chemical shifts based on changes in oxidation state based on their local bonding environment, and changes in the valence band structure of semiconductors.

The kinetic enegy of ejected electrons E_{KE} is used to determine the binding energy E_b of states in the semiconductor relative to the position of the Fermi level E_F (where $E_b = 0$) by the relation

$$E_b = h\nu - (E_{KE} - \Phi_{det}) \tag{5.2}$$

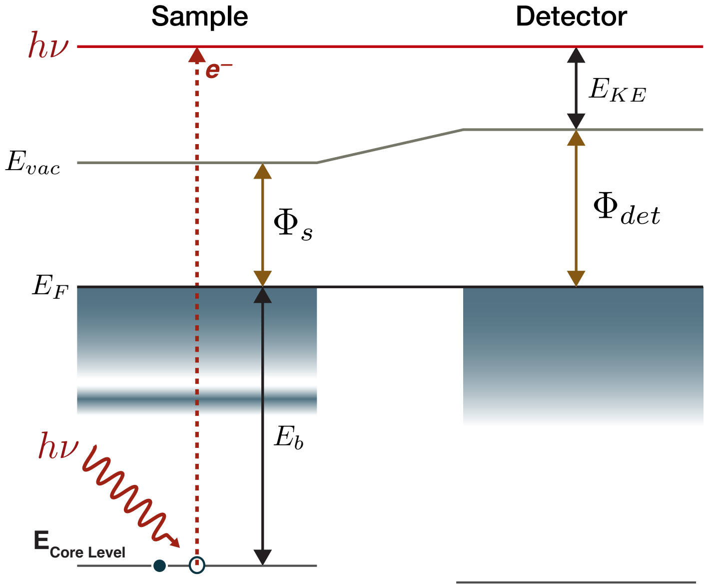

Figure 5.3: Schematic illustration of X-ray photoelectron spectroscopy. The binding energy E_b of states in a material are probed by monochromatic X-ray photons via the photoelectric effect. The resulting electron kinetic energy E_{KE} spectrum reflects the occupied density of states in the sample.

where $h\nu$ is the incident X-ray photon energy and Φ_{det} is the work function ($\Phi_{det} \equiv E_{vac} - E_F$) of the detector used in the experiment. Figure 5.3 provides a schematic of a typical XPS experiment with the energy terms of Equation 5.2 indicated. A sample is brought into electrical contact with the detector, establishing a constant E_F for the system. The sample is exposed to monochromatic X-rays, typically Al K_α radiation, which eject electrons from all filled states simultaneously. A hemispherical electron energy analyzer, consisting of two hemispherical, parallel-plate electrodes with variable bias, is typically used to measure the dispersion of E_{KE}. Electrons from core levels with high E_b will have low E_{KE}, and valence band electrons be detected with high E_{KE}. The value of the work function of the sample Φ_s is not essential for the calculation of E_b but can be determined based on the high-energy cutoff of the spectrum [156].

XPS analysis is extremely surface sensitive. While the photoexcitation of electrons occurs much deeper in the sample, only electrons within a few nanometers of the surface will escape without causing secondary electrons (which contribute to a nonlinear background in the signal that is asymmetric around each peak, known as the Shirley background [156, 157].)

A set of Cd$_x$Zn$_{1-x}$O samples independent of those used in the irradiation experiment, but selected from the same growth series, was examined by XPS in order to probe shifts in the valence-band maximum and core levels as a function of composition. XPS spectra were measured using a monochromated Al K_α X-ray source ($h\nu = 1486.6$ eV) with a Kratos Axis Ultra DLD hemispherical electron analyzer.

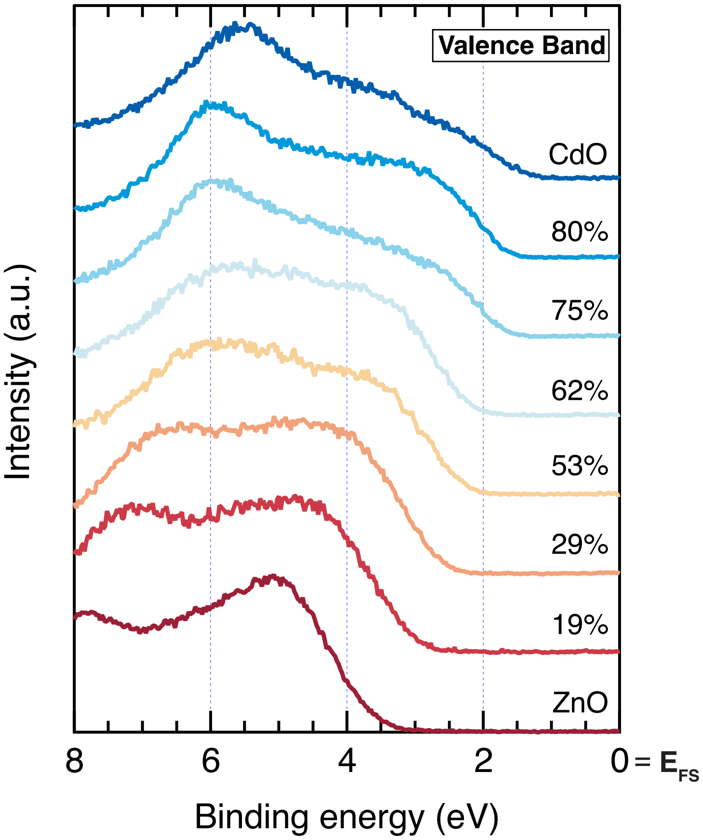

Figure 5.4: XPS valence band spectra of $Cd_xZn_{1-x}O$ alloys. A linear extrapolation of the band edge shows that the VBM shifts upward by ~1.4 eV across the WZ phase regime, moving to even lower binding energies for the RS alloys. The total shift in the VBM across the entire composition range is ~ 2.3 eV.

5.3.1 Results

Valence band spectra of samples spanning the complete composition range are shown in Figure 5.4. The VBM for each sample was determined by taking a linear extrapolation of the valence band edge to zero intensity. There is a monotonic decrease in binding energy of the VBM over the entire composition range. Across the WZ phase regime, the binding energy of the VBM decreases from 3.3 eV (ZnO) to 2.2 eV ($x = 0.53$) whereas the binding energy of the VBM moves to even lower values (~ 1.6 eV) in the RS range. In contrast to that of the WZ alloys, the onset of the valence band edge for the RS alloys is less abrupt. The shallower slope may indicate that the L-point VBM of the CdO endpoint established in previous studies is preserved with Zn incorporation [77, 83, 158]. As well, this conclusion is supported by the lack of band edge photoluminescence from the RS alloys seen in Section 4.4.1. While binding energies are plotted relative to the Fermi level of each sample, the surface sensitivity of XPS

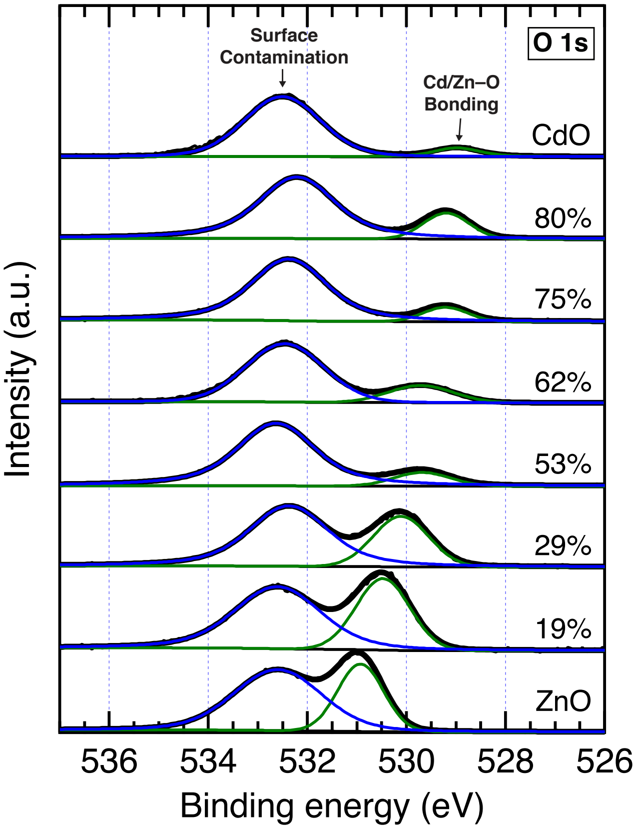

Figure 5.5: XPS O1s core-level spectra for $Cd_xZn_{1-x}O$ alloys across the composition range. The high binding-energy component can be attributed to surface contamination, following King et al. [158], while the lower-binding-energy feature arises from metal-oxygen bonding. XAS/SXE spectra recorded relative to the O1s level (shown in Figure 5.7) must be corrected for the nearly 2 eV shift to lower-binding energy with Cd content observed in this second peak.

allows one to reference the observed shifts to a common energy level because the Fermi level at the surface of each sample is inherently pinned at E_{FS}.

XPS also reveals chemical shifts in the oxygen 1s core-level energy across the composition range. As indicated in Figure 5.5, there are two components to the peak at the O1s level: a high-binding-energy peak that is nearly static with Cd content and a lower binding-energy component that exhibits a monotonic decrease in energy with increasing Cd content. These peaks were fitted with two Voigt lineshapes and a standard Shirley background. As shown by King et al. [158] for the case of binary CdO and ZnO, the high-binding-energy feature arises from surface contamination while the presence of the lower binding-energy peak is due to Cd-O and Zn-O bonding. Over the entire composition range the peak moves by nearly 2 eV, a shift that is consistent with that reported by Ma et al. [117].

It is critically important to account for such core-level shifts when performing X-ray absorption and emission spectroscopy, where the resultant spectra are taken with respect to the energy of these specific core levels. Section 5.4, which combines the results of Figure 5.5 with such soft X-ray spectra, demonstrates the dramatically different (and erroneous) conclusions that the as-recorded spectra lead to without these necessary corrections.

5.4 Soft X-ray absorption/emission spectroscopy

Soft X-ray spectroscopy uses a tunable source of X-rays with $h\nu < 1$ keV to probe both the filled and untilled states in the electronic structure of a material. Synchrotron radiation provides a tunable source of coherent, high-intensity photons in this energy range, and as such this spectroscopy is performed at such facilities. Different types of soft X-ray spectroscopy are used in a wide range of disciplines, and a general survey of these techniques is outside the scope of this work[1] [160].

At present, two basic modes of operation are considered: soft X-ray absorption spectroscopy (XAS) and soft X-ray emission spectroscopy (SXE). The working principles of these complementary techniques are illustrated in Figure 5.6. In XAS, depicted in Figure 5.6a, a monochromator is used to vary the wavelength of incident soft X-rays incident on a sample. In the case of an oxide, X-rays energies in the range of the O1s binding energy (530 eV) are used to excite electrons from the core level. The absorption spectra is recorded by measuring either the total fluorescence yield (TFY) of X-ray emission back to the empty core level, or the current into the sample. Due to the elemental specificity of this absorption process, each signal is proportional to the partial density of states of the material relevant to that element. In the case of excitation from an O1s level the absorption (and subsequent emission) processes probe the density of states derived from oxygen bonding, which include states in the valence band, conduction band, and hybridized core levels.

Soft X-ray emission (SXE), depicted in Figure 5.6a, is a complementary X-ray spectroscopy method that can be used to probe the filled, elemental-specific partial density of states of a material. In this photon-in, photon-out technique, the excitation X-ray energy is fixed at an energy that is at or above the threshold for X-ray absorption. As electrons from occupied states above the core level relax to fill the core hole, an emission spectrum is recorded by a spectrometer. Additional band structure information in SXE can be found by taking advantage of the K selectivity of the SXE process. Core levels are delocalized in k space and as a result electrons from these levels can undergo direct transitions to unfilled states across the Brillouin zone, regardless of wavevector, in contrast to the direct transitions observed in optical absorption spectroscopy. If the excitation X-ray wavelength is tuned to an energy that is at the threshold of X-ray absorption, emission is restricted to only those valence states within a narrow range of k-space. If X-ray emission is tuned well above the

---

[1] A general review of different forms of soft X-ray spectroscopy can be found in Refs. [159, 160].

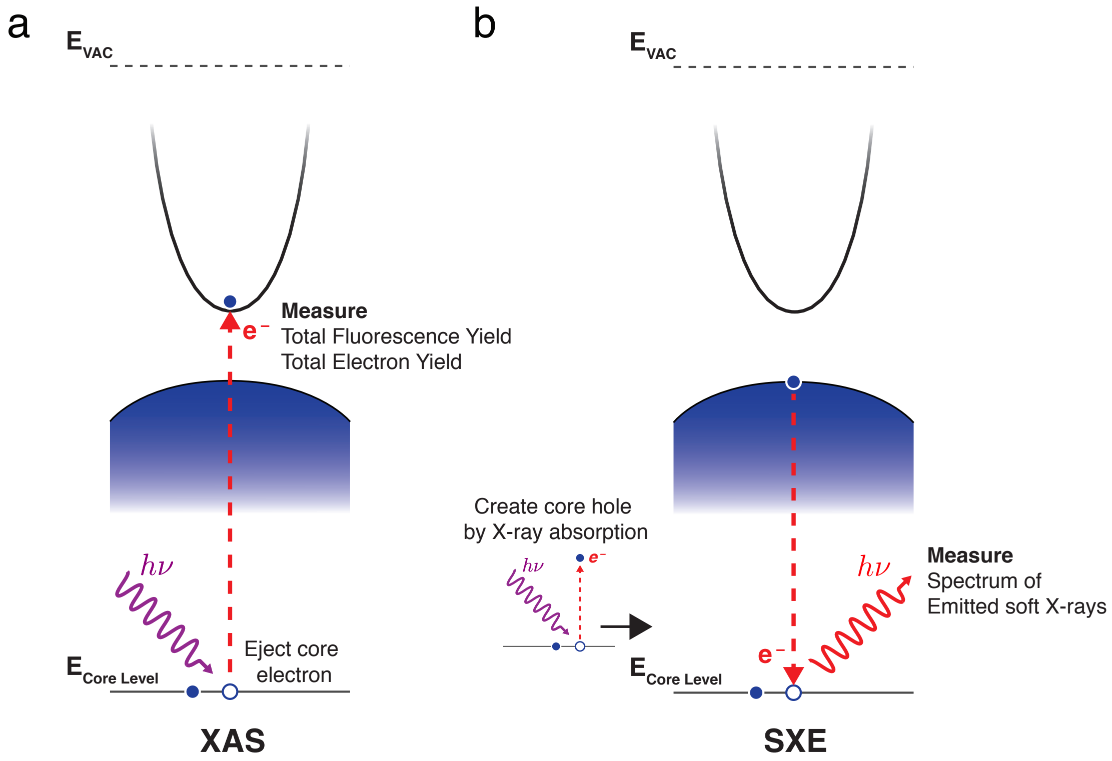

Figure 5.6: XAS/SXE schematic.

absorption edge, emission from valence band states across the Brillouin zone will contribute to the SXE signal.

Given its versatility, soft X-ray spectroscopy is a commonly used method to validate band structure calculations. Previously, these techniques have been used to compare the band structure of both CdO [80, 83] and ZnO [161] to *ab initio* calculations. It is important to note that both XAS and SXE are referenced to whatever core level is fundamental to the excitation and emission process, and as such any changes in this level due to chemical- or core-hole-effects must be corrected for.

In order to independently and directly probe changes in the conduction and valence band edges of $Cd_xZn_{1-x}O$ as a function of composition, XAS/SXE were used to measure the oxygen partial density of states in the conduction and valence bands, respectively. For each of the samples previously analyzed by XPS, oxygen K-edge absorption spectra and oxygen-resonance emission spectra were recorded at Beamline 8.0.1 of the Advanced Light Source at Lawrence Berkeley National Laboratory. The absorption spectra, measured by total fluorescence yield, were recorded with the sample oriented 45° relative to the direction of incidence; the emission spectra were recorded using 530 eV photon excitation. The SXE spectra were normalized such that the maximum intensity value of each was scaled to 1. The XAS spectra were first normalized to a common value far above threshold (556 eV) before the spectra were uniformly scaled to set the maximum intensity (of the CdO spectrum) to 1. The XAS and SXE spectra were placed on a common energy scale by shifting the SXE spectra so that the elastic emission feature from the 530 eV excitation in the SXE spectra was aligned with the 530 eV point in the XAS spectra.

5.4.1 Results

The intensity-normalized spectra are presented in Figure 5.7. Figure 5.7b provides a magnified scale to show changes in the absorption and emission edges with composition. These "uncorrected" spectra appear to suggest that the VBM, found by extrapolating each curve to the horizontal axis, is stationary with composition and that the narrowing of the gap with Cd content is caused by a nearly 2 eV decrease in the CBM energy. The energy scale of the spectra presented in the upper panels of Figure 5.7a and 5.7b references the incident and emitted photon energies, and thus its features are measured with respect to the O1*s* core level. As demonstrated in the XPS measurements, however, the energy of this core level is not constant with alloy composition. As a result, the positions of the as-recorded, "uncorrected" absorption and emission edges do not represent energy shifts in the unfilled conduction band (XAS) and filled valence band (SXE) states on an absolute scale.

The compositional changes in the CBM and VBM can be assessed by shifting the XAS/SXE spectra by the change in its O1*s* level, as measured by XPS, relative to that of ZnO. The corrected spectra, shown in the lower panels of Figure 5.7a and 5.7b, reveal that with increasing Cd content there is a systematic rise in the emission edge while the absorption edge remains relatively constant across the composition range. The 2 eV rise in the VBM observed by SXE is consistent with the VBM shift measured by XPS in Figure 5.4.

5.5 $Cd_xZn_{1\text{-}x}O$ band offsets

A summary of the results from the three independent measurements of the conduction and valence band edge positions is presented in Figure 6. The irradiation and XPS results, as discussed previously, can be independently placed on an absolute energy scale, while the relative shifts in the band edges extrapolated from the XAS/SXE spectra are placed on the same absolute scale by matching the value of the VBM (SXE) and CBM (XAS) to the absolute values obtained from XPS and irradiation, respectively.

In two of the measurement techniques the position of only one band edge is measured independently, but in both cases the energy of the other band can be inferred by including the intrinsic, direct bandgap E_g (see Section 4.5.2) found by correcting the measured optical absorption edge for free carrier effects. In this way, irradiation-induced Fermi-level pinning directly measures the CBM and indirectly yields the valence band at the Γ point, as optical transitions are always direct. For direct-gap WZ alloys, the VBM is located at the Γ point. For RS alloys, as is the case with CdO, however, the VBM is positioned at the L symmetry point and gives rise to an indirect bandgap. In the case of the RS alloys, therefore, the Γ

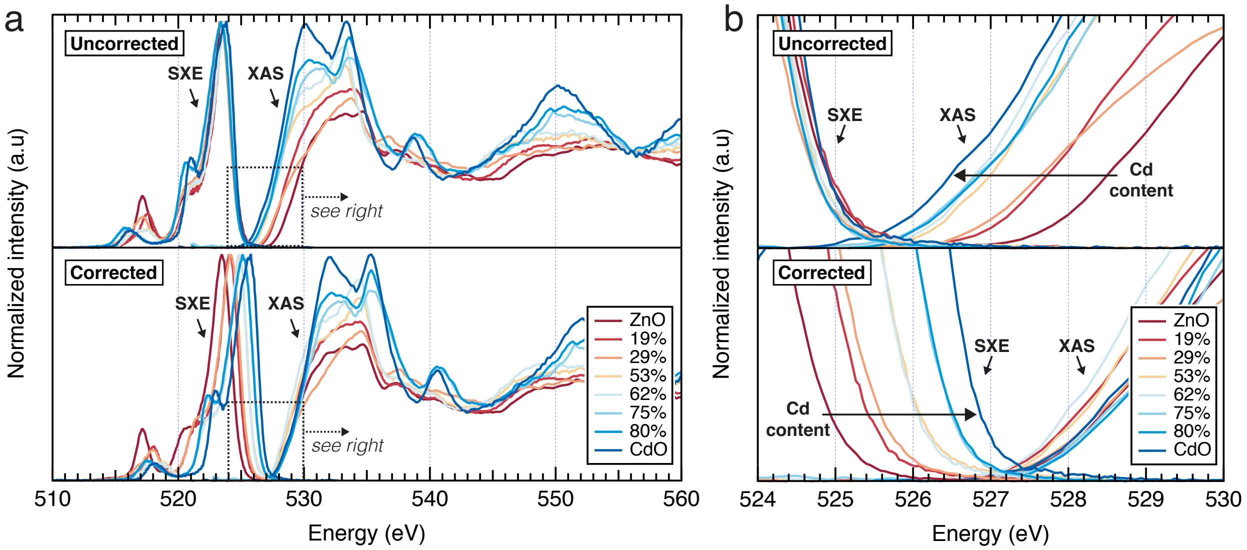

Figure 5.7: Normalized soft X-ray absorption and emission spectra for $Cd_xZn_{1-x}O$ alloys across the composition range, uncorrected (top) and corrected (bottom) for chemical shifts in the O1*s* core level position shown in Figure 4. The full normalized XAS/SXE spectra are shown in (a) while a magnified energy scale in (b) reveals shifts in the density of states near the VBM (SXE) and CBM (XAS). The band edge shifts with Cd content suggested by the uncorrected spectra (the downward movement of the CBM and a stationary VBM) are reversed when the movement of the core level position is taken into account. The corrected spectra reveal a rise in the VBM density of states and a relatively stationary CBM (XAS).

point valence band position revealed by Fermi-level pinning and subsequent optical bandgap subtraction is complementary to the band edge extremum measured by the two X-ray spectroscopic techniques. Conversely, adding E_g to the VBM measured by XPS yields a value for the CBM, but only for direct-gap, WZ films.

There is good agreement among the three techniques about the observed changes in the band edges with composition. In the WZ-phase regime, there is excellent agreement between the directly measured (irradiation-CBM and XPS-VBM) and indirectly inferred (irradiation-VBM and XPS-CBM) band edges. The relative shifts observed by XAS/SXE support the conclusion that the considerable narrowing of the optical gap from 3.3 eV to 1.7 eV across the WZ composition range can be ascribed to the $>$ 1 eV shift of the VBM toward the vacuum level. For both RS samples, the VBM measured by XPS and XAS is considerably higher in energy than the Γ-point VBM inferred from irradiation, offering another indication that the indirect gap of the endpoint CdO is maintained for RS-alloys. Additionally, the $\sim$ 220 meV decrease in the Γ-point VBM for the RS alloy relative to that of the endpoint CdO partially accounts for the $\sim$300 meV difference in E_g found in Section 4.5.2.

Several previous studies have explored the electronic structure of the endpoint binary

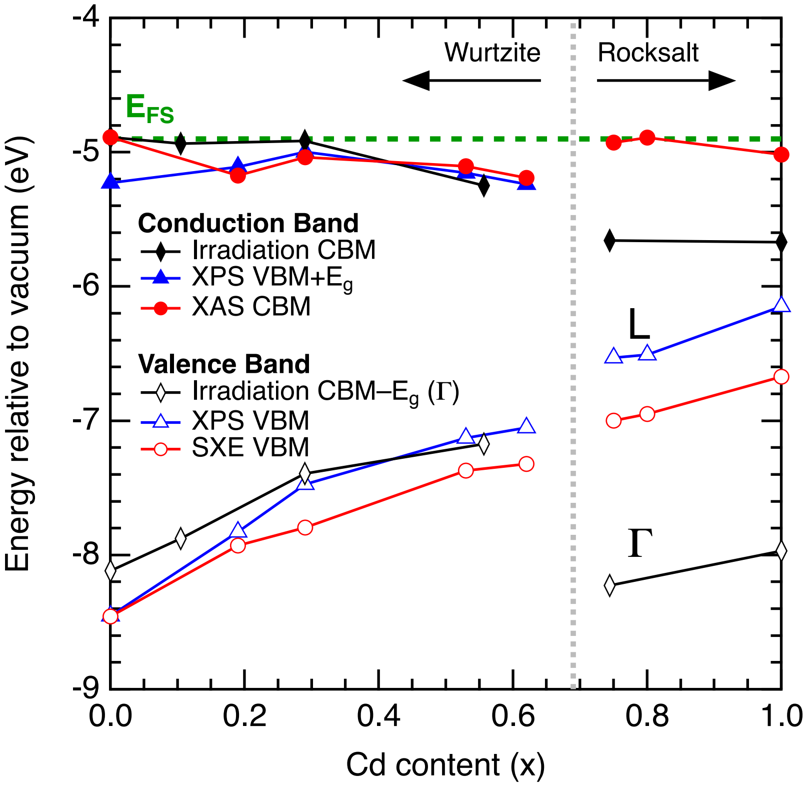

Figure 5.8: The band edge shifts as measured by irradiation-induced Fermi-level pinning, XPS, and XAS/SXE, along with complementary band edge information that can be inferred by incorporating the intrinsic direct bandgap E_g from Section 4.5.2. All three techniques reveal that the narrowing of the intrinsic gap across the WZ composition range can be largely attributed to a > 1 eV rise in the valence band. The indirect gap at the L-point observed in CdO is preserved for RS alloys.

compounds [158, 162, 78], with the natural band alignment calculated by Zhu et al. [162] showing offsets in both the conduction band minima and valence band maxima of CdO and ZnO equilibrium phase structures [25]. As discussed in Section 2.1.2, in pure CdO the valence band structure that gives rise to this L-point maximum is attributed to the close proximity of shallow, filled Cd d levels below the VBM [158].

The electronic structure of ternary $Cd_xZn_{1\text{-}x}O$ alloys was calculated by Schleife et al. [119], indicating a total offset in the CBM ΔE_{CBM} of WZ alloys (that is, from $x = 0$ to the extrapolated value of WZ-CdO at $x = 1$) of $\sim$ 1 eV. The remaining band edge movement that contributes to the total narrowing of E_g (1.6 eV from $x = 0$ to $x = 0.69$) is predicted to come from the upward movement in the VBM. The magnitude of ΔE_{CBM} measured here for the WZ structured alloys is slightly less, approximately $\sim$ 600 meV across the full composition range, and contributes $\sim$ 400 meV to the total reduction in E_g. Each of the spectroscopic measurements in this study independently confirm that the upward rise in the VBM (> 1 eV) is the origin of this bandgap tunability.

The nearly constant value of the CBM in the WZ and RS phase observed here explains the unusually weak composition dependence of the electron mobility we observed in Figure 4.2, where the electron mobility of WZ alloys increases slightly from ~ 15 cm^2/Vs to ~ 30 cm^2/Vs over $0 < x < 0.69$. Typically, alloying of semiconductor materials results in a significant reduction of charge carrier mobilities by alloy disorder scattering. The strength of this scattering mechanism is related to the fluctuations of the CBM due to random atom distribution and is determined by ΔE_{CBM} for each phase regime. As discussed in Section 2.2, the mobility limit for alloy disorder scattering as a function of alloy composition x is related to ΔE_{CBM} by

$$\mu_{\mathrm{AD}} \propto \frac{1}{|\Delta E_{\mathrm{CBM}}|^2 x(1-x)}, \tag{5.3}$$

following Ref. [98]. As seen in Figure 5.8 the values of ΔE_{CBM} measured by all three techniques for both WZ and RS phase are small, indicating that there is a negligible contribution from alloy disorder scattering.

Despite the relatively high electron concentration ($n \sim 10^{19}$ cm^{-3} to $n \sim 10^{20}$ cm^{-3}) of the as-grown samples, there is no distinguishable signal in the XPS spectra from filled states at the Fermi level. Even in the sample with the highest measured electron concentration, the RS alloy with $x = 0.74$ and $n \sim 2 \times 10^{20}$ cm^{-3}, this concentration corresponds to a native donor concentration of $< 1\%$, near the detection limits of the technique. Nonetheless, such a feature has been observed in the case of other nominally undoped transparent conducting oxides, such as in In_2O_3 [163]. The surface quality of the films in this study, as evidenced by the intensity of the O1s peaks due to surface contamination, may help explain the absence of this feature.

We have determined the band alignments of $Cd_xZn_{1-x}O$ alloys across the full composition range, finding good agreement among three independent measurements of VBM and CBM movement in order to explain optical trends such as the reduction in the intrinsic bandgap of luminescent WZ-$Cd_xZn_{1-x}O$ alloys and the widening of the bandgap of RS-$Cd_xZn_{1-x}O$ alloys relative to CdO. The relatively stationary position of the CBM across the WZ composition range, and the correspondingly negligible role of alloy disorder scattering, explain the trends in the electron mobility reported previously. The rise in the VBM is larger than previously expected and, as will be discussion in Chapter 6, opens up opportunities for creating novel PEC device designs.

Chapter 6

Application of $Cd_xZn_{1-x}O$ alloys in photoelectrochemical applications

The results presented in Chapter 4 show that the structural mismatch of the binary endpoints in the $Cd_xZn_{1-x}O$ system—WZ-ZnO and RS-CdO—results in two distinct regions of optical and electrical behavior. As will be shown in this chapter, these changes in the $Cd_xZn_{1-x}O$ alloy system across the composition range satisfy all of the material requirements for constructing a tandem photoelectrochemical (PEC) photoanode for solar water splitting. A comprehensive review of the materials considerations for such devices is given in Ref. [164, 165, 166].

6.1 Semiconductor materials for water splitting

Metal-oxide semiconductors are of particular interest for their use as electrodes in PEC devices, which could potentially produce hydrogen fuel for industrial needs[1] in an inexpensive, environmentally friendly manner. Current industrial processes rely on steam reforming using hydrocarbon inputs [167, 166]. PEC devices fit into an overall category of techniques known as *artificial photosynthesis*, as they harvest sunlight to produce fuel. Like its natural counterpart, though, artificial photosynthesis requires a holistic approach to managing several reactions, materials, and gasses at once, and requires such a system to be stable over a long period of time in (for most semiconductors, at least) harsh chemical environments. Good electrode materials must exhibit long-term resistance to the corrosive effects of the photoelectrochemical reactions, good charge transport characteristics within the layer as well as at the electrode/water interface for efficient interaction between electrons/holes and aqueous ions, and moderately large direct bandgaps with high absorption coefficients [164, 165].

---

[1] In addition to the potential need of hydrogen for transportation, the production of hydrogen is also a first step in some of the most industrially important chemical reactions on Earth, including ammonia production by the Haber-Bosch process [167].

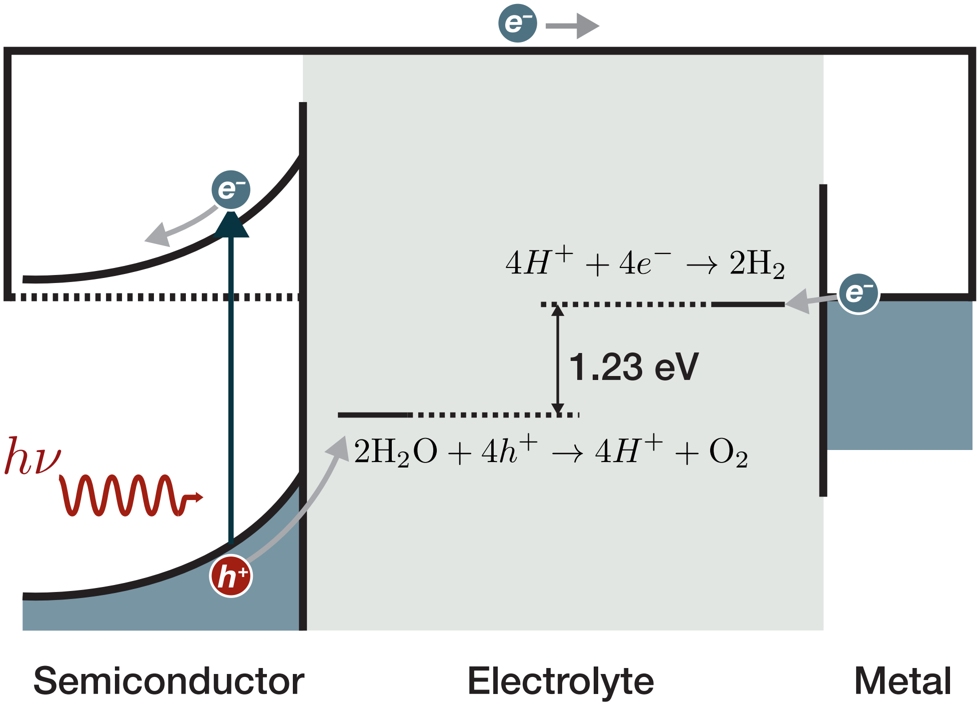

Figure 6.1: Schematic of PEC device with semiconductor photoanode and metal cathode in electrolyte solution. Adapted from Ref. [164].

An additional requirement for PEC materials involves the absolute position of the band edges with respect to the reduction and oxidation potentials of water. For water splitting in an acidic environment, the reduction half-reaction at the cathode is given by

$$4\mathrm{H}^+ + 4e^- \Longleftrightarrow 2\mathrm{H}_2 \ (0.000 \text{ V rel. to NHE}) \tag{6.1}$$

where NHE is the potential of the neutral hydrogen electrode, defined to be 0 V. The oxidation half-reaction at the anode is given by

$$2\mathrm{H}_2\mathrm{O} + 4h^+ \Longleftrightarrow \mathrm{O}_2 \ (-1.299 \text{ V rel. to NHE}). \tag{6.2}$$

The absolute potentials of these half-reactions can be put on the same absolute scale as the band offsets, following Ref. [164], and are included on the band offset chart in Figure A.1. At pH = 2, the H^+/H_2 reduction potential (Equation 6.1) is $4.4 - 4.5$ eV below E_{vac} and the O_2/H_2O oxidation potential (Equation 6.2) is $\sim 5.6 - 5.7$eV below E_{vac}. A basic schematic for PEC design is shown in Figure 6.1. Here, photogenerated carriers in a single material are brought to suitable electrochemical potentials for water splitting; holes at the VBM participate in oxidation while electrons are moved to a metal counter-electrode (such at Pt) for reduction. At a minimum, the material must have a bandgap larger than 1.29 eV in order to photoexcite charge carriers to overcome the potential requirements of Equations 6.1 and 6.2. To a certain extent a larger bandgap is desirable—carriers in a semiconductor photoanode can more easily overcome small surface barriers, but too large a bandgap limits the photo current of the device, just as it does in PV devices.

As suggested by Figure 6.1, the band offsets of semiconductor PEC materials are of paramount importance: the absolute positions of the CBM and VBM must straddle these reduction and oxidation potentials. Electrons at the surface of the electrode must be at higher energies than the water reduction potential, while holes at the surface must sit at a lower energy relative to the oxidation potential. Of course, this simple band-offset picture does not consider the complex behavior of real semiconductor-liquid junctions, in which band bending, surface charge, and adsorbed ions all play a critical role in determining device performance and stability. Nonetheless, these energy-level criteria are of paramount importance and to date no single material has been shown to meet them. Indeed, the collected band offsets of various semiconductors in Figure A.1 provides a rather discouraging picture for the prospects of using a single material for PEC devices. The VBM of most oxides is positioned far too low relative to the oxidation potential of water to supply holes to the water oxidation/oxygen evolution reaction in Equation 6.2, and their conduction bands are located below the reduction potential for H_2 evolution [164].

PEC devices based on tandem designs offer a more viable route to using semiconductors for water splitting. “Z”-scheme devices use two or more semiconductor materials with different gaps. In such devices, a photoelectrochemically active anode layer is connected in series with a photovoltaic device. The ideal heterojunction design for such a device is a type II/III band alignment, such that the valence band of the underlying PV layer at its top interface is aligned with the conduction band of the top photoanode[2]. Photogenerated holes in the top photoanode layer move to the surface to participate in water oxidation, while electrons in this layer recombine through the ohmic tunnel junction with photogenerated holes in the valence band of the underlying PV layer [168]. Photoexcited electrons in the underlying PV layer can be moved to an independent cathode, such as Pt, to produce H_2. This overall device architecture is referred to as the ”D4” concept, as it requires four photons to split each molecule of water. While several materials combinations have been explored in these tandem device designs, to date no such combination has proven to be a durable device for spontaneous solar water dissociation [169].

6.2 $Cd_xZn_{1\text{-}x}O$ alloys for water splitting

The properties of $Cd_xZn_{1\text{-}x}O$ alloys presented in Chapter 4 and the natural band alignments of $Cd_xZn_{1\text{-}x}O$ alloys determined in Chapter 5 suggest that “Z”-scheme PEC devices based on $Cd_xZn_{1\text{-}x}O$ photoanodes may be well suited to the demands outlined above. As seen in Figure 4.7, the direct bandgap of wurtzite $Cd_xZn_{1\text{-}x}O$ can be tuned from 3.3 eV (ZnO) to 1.7 eV ($x = 0.69$), and the results presented in Figure 5.8 show that this decrease is a result

---

[2] This alignment gives rise to the “Z” in the name of this design strategy.

of a significant rise in the VBM toward the vacuum level with Cd content. At the transition composition the conduction band shifts abruptly downward and the new valence band maximum appears in the L symmetry direction. As a result the alloys become indirect-bandgap semiconductors for $x > 0.69$ with excellent electrical transport properties. In addition, the proximity of the CBM of WZ-structured alloys to the VBM of some semiconductors (Si, Ge) suggests that films may be ideally suited for photoanode applications in tandem device designs.

A schematic of a hypothetical PEC design that makes use of a $Cd_xZn_{1-x}O$ photoanode is illustrated in Figure 6.2. The proposed structure, shown in Figure 6.2, is a tandem PEC device that relies on a photoelectrochemically active layer—in this case, multiple layers of $Cd_xZn_{1-x}O$—connected in series with a Si homojunction PV device.

The device schematic shown in Figure 6.2 consists of an n/p Si junction base device with a compositionally-graded $Cd_xZn_{1-x}O$ layer consisting of a WZ absorber ($0 < x < 0.69$) and a RS ($x > 0.69$) top layer. The base of the device is a standard Si $n-p$ solar cell consisting of a thick n-type absorber and a thin p-type hole emitter layer. Photogenerated electrons in these layers move to the cathode (not pictured) to carry out the hydrogen reduction part of the water splitting reaction. The photoanode, grown directly on the Si underlayer to form an ohmic contact [168], consists of direct gap WZ-$Cd_xZn_{1-x}O$ with a graded composition from pure ZnO (or large Zn-content $Cd_xZn_{1-x}O$) to $x = 0.69$ ($E_g = 1.7$ eV) and a top layer of indirect-gap RS-$Cd_xZn_{1-x}O$ or CdO. The upward rise in the VBM with Cd content across the entire $Cd_xZn_{1-x}O$ alloy system suggests that holes generated in a linearly graded WZ absorber would be swept toward the surface and into the RS top layer. Photogenerated electrons in the WZ layer recombine with photogenerated holes from the Si base layers, while holes generated in the WZ layer are swept in the opposite direction, toward the anode surface, as a result of the internal electric field that is generated by the upward rise in the VBM with increasing Cd composition. To a first approximation a direct gap WZ absorber with a bandgap of 1.7 eV would split the solar spectrum with the Si PV layer into two current-matching portions [168, 170]. It is important to note that the interfacial barriers presented in Figure 6.2 are only a rough approximation based on expected doping levels in the device and the natural band offsets described earlier. In future work ideal doping levels will need to be modeled and experimentally validated. Overall, the proposed device structure has a unique advantage of combining a direct-gap semiconductor layer that strongly absorbs solar photons with an indirect-gap semiconductor layer that exhibits long hole lifetimes.

The position of the CBM of the top RS layer may limit photo-induced surface degradation at the water/device interface, as electrons at this low energy are below the reduction potential for hydrogen evolution, As well, the indirect gap of the RS layer may provide yet another advantage for PEC applications: holes transferred into this layer will move to the L-point maximum, avoiding immediate recombination. The holes transferred to the indirect valence band maximum in the top RS layer are predicted to have long lifetimes: initial microwave photoconductivity measurements (not shown) suggest that $\tau > 50\,\mu$s for PFCAD-grown CdO and RS-$Cd_xZn_{1-x}O$ alloys. The long-lived holes move to the surface in contact with water and complete the oxygen evolution half-reaction through the oxidation of water molecules. One drawback to the use of CdO is the large band-bending effects due to electron accumulation from Fermi-level pinning at surfaces, although this behavior at the interface can be controlled by intentional doping of the top CdO layer. The CdO semiconductor surface has an electron accumulation layer with positively charged surface donors that gives rise to an electron concentration of $n = 4 \times 10^{20}$ cm^{-3} and a surface depletion layer with negatively charged surface acceptors for higher electron concentrations. The flat band condition is realized for $n = 4 \times 10^{20}$ cm^{-3}.

The tandem PEC design presented here is only a first step toward exploring the potential of $Cd_xZn_{1-x}O$ materials for such applications. The photoelectrochemical stability as well as the electrical behavior of all interfaces in the device will need to be explored on the way to realizing such a device.

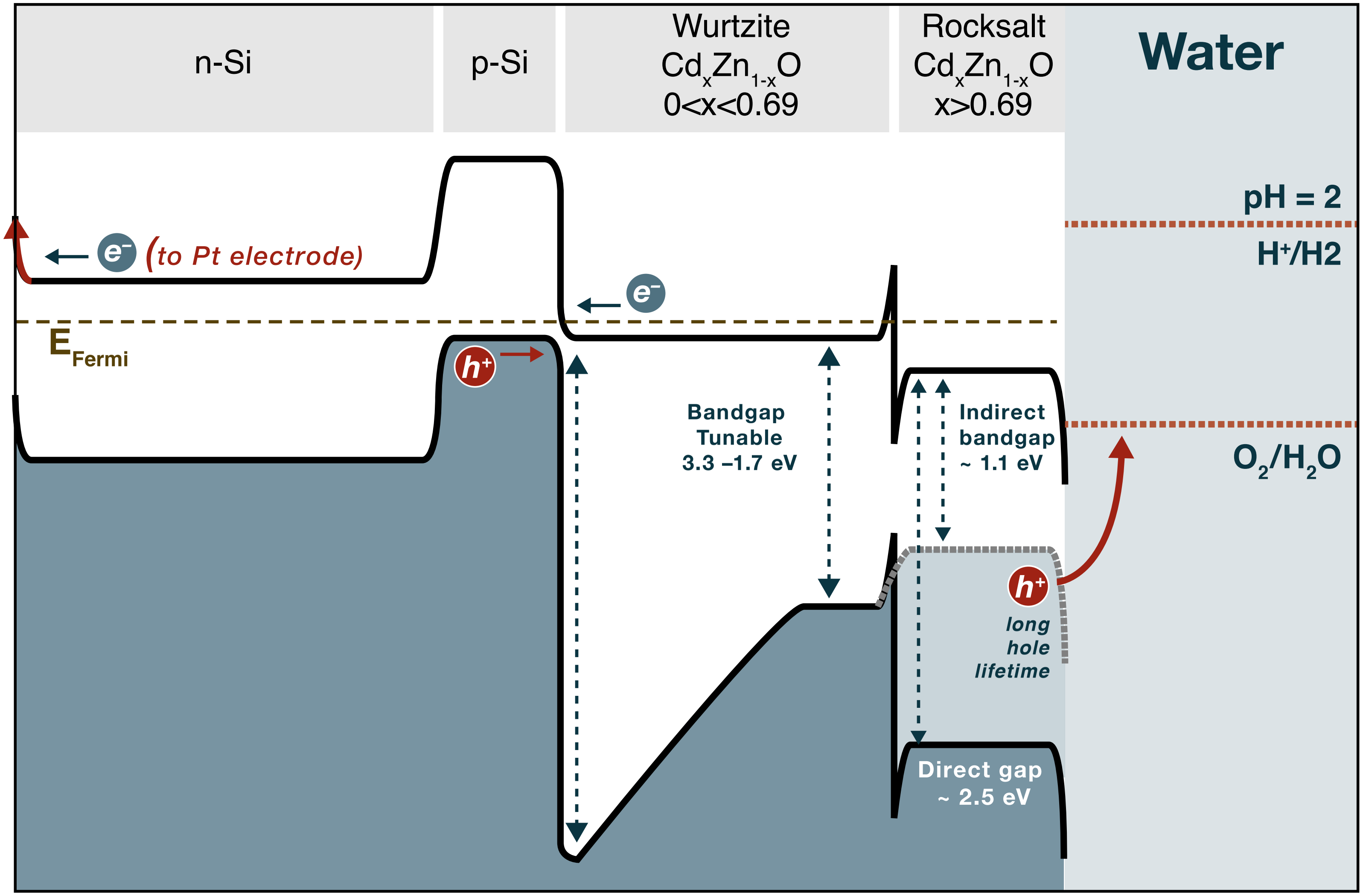

Figure 6.2: Schematic for "Z"-scheme PEC device with WZ-CdZnO and RS-CdZnO heterostructure on Si. Holes generated in the photoanode are swept to the RS surface layer by the upward rise in the VBM across the Cd-graded layer. The indirect gap affects the transport characteristics of the top RS layer and offers an opportunity for long hole lifetimes but does not significantly affect the absorption edge. Photogenerated electrons in the Si move to a separate cathode for H_2 production. Recombination occurs at the ohmic junction between device layers.

Chapter 7

Electrical properties of doped CdO: Modeling and experiment

As outlined in Chapter 1, TCO materials must exhibit extremely low resistivity, ideally $\rho < 10^{-4}\,\Omega\,\text{cm}^{-1}$. Finding semiconductors with high electron mobility, and equally important—high doping limits—is a significant materials challenge. In Section 2.1.3, doped CdO films from Ref. [19] were shown to have excellent electrical properties, with $\rho \sim 3 \times 10^{-5}\ \Omega\ \text{cm}^{-1}$. This excellent conductivity, driven by its high electron mobility, opens up significant opportunities for its use in many low-bandgap PV applications. The experimental portion of this dissertation focused on understanding how the properties of CdO can be tuned by alloy engineering. As a complement to this experimental bandgap engineering work, in this chapter the electrical properties of doped-CdO are investigated using doping and mobility simulations in order to explore the ultimate limits to the electrical properties of CdO.

Historically, the doping limits of semiconductors have been a topic of great practical and theoretical interest. The amphoteric defect model, summarized in Section 2.1.1 and described in detail in Refs. [65, 66, 67, 171, 172], indicates that the ultimate limits to doping arise due to Fermi-level stabilization at E_{FS}, which drives the formation of compensating native defects as E_F moves away from this universal level [67]. This framework has successfully been applied to the understanding of many III-V and II-VI materials [67, 171, 172]. In practice, doping a material up to the maximum predicted by the ADM framework is complicated by dopant solubility and the formation of other materials phases, strain effects, kinetic limits in processing techniques, diffusion of dopants, and passivation by unintentional impurities such as hydrogen. Nonetheless, one can extract useful knowledge and gain insights into doping behavior applying a simplified, equilibrium model to these complex systems. Here, the ADM concept is applied to study interplay between doping and native defects in doped CdO. Because this model provides a thorough accounting of ionized impurity concentrations as a function of extrinsic doping, these doping results can be extended to predict changes in the electron mobility with doping. The results of these simulations are compared with experimental data from CdO:Ga thin films in Section 7.2.

7.1 Modeling electrical properties of doped CdO

7.1.1 Fermi-level defect concentrations

In a degenerately-doped n-type semiconductor with impurity donors D (of concentration N_D) and doubly-ionized native donors DD^{2+} and acceptors AA^{2-} (of concentration N_{DD} and N_{AA}, respectively), the charge neutrality condition is given by

$$n = \xi_o N_D + 2N_{DD} - 2N_{AA}, \tag{7.1}$$

where ξ_o is a dopant activation function, such that ξN_D represents the number of activated donors D^+. In the simulations presented in this chapter, a constant value of $\xi_o = 1$ is assumed, but it is reasonable to imagine physical justifications for values other than unity. If poor dopant activation is achieved during processing, $\xi_o < 1$ and N_D will be less than that suggested by composition measurements. If dopant activation is dependent on the Fermi level such that dopants are deactivated if the Fermi level lies above their donor level E_d, the activation factor takes on the functional form

$$\xi(E_F) = \xi_o \left(1 + \exp\left[\frac{E_F - E_d}{k_B T}\right]\right)^{-1}. \tag{7.2}$$

The concentration of impurity donor atoms (in cm^{-3}) is related to the experimentally measured impurity cation fraction x_{Dopant} (e.g. $\mathrm{In_xCd_{1\text{-}x}O}$) by the conversion

$$N_D = x_{\mathrm{Dopant}} \left(\frac{N_\mathrm{s}}{2}\right) = x_{\mathrm{Dopant}} \left[\frac{\rho_{\mathrm{CdO}}(M_{\mathrm{Cd}} + M_{\mathrm{O}}) \times N_{\mathrm{Avogadro}}}{2}\right] \tag{7.3}$$

where $N_s/2$ represents the density of cation sites in the CdO lattice, ρ_{CdO} is the density of CdO (in $\mathrm{g/cm^{-3}}$), M_{Cd} and M_{O} are the molar masses of cadmium and oxygen, respectively, and N_{Avogadro} is Avogadro's number.

As described in Section 2.1.1, a central feature of the ADM concept is that the formation energy of native point defects is dependent on the difference between E_F and E_{FS}, the Fermi-level stabilization energy. The formation energies of native donors $E_{f_{DD}}$ and acceptors $E_{f_{AA}}$ are

$$\begin{aligned} E_{f_{DD}} &= E_{f_o} - 2(E_{\mathrm{FS}} - E_F) \\ E_{f_{AA}} &= E_{f_o} + 2(E_{\mathrm{FS}} - E_F) \end{aligned} \tag{7.4}$$

where E_{f_o} is the formation energy of both native donors and acceptors at E_{FS}. All energies are referenced to the CBM. The magnitude of the slope of the linear function in formation energy equations is the charge defect state. In this idealized model, only doubly-ionized native defects are considered and this factor is 2.

Thermodynamically, at a given temperature T the concentrations of native donors N_{DD} and acceptors N_{AA} are determined the by the values of their formation energies, such that

$$\begin{aligned} N_{DD} &= \left(\frac{N_s}{2}\right)\exp\left[\frac{-E_{f_{DD}}}{k_BT}\right] \\ N_{AA} &= \left(\frac{N_s}{2}\right)\exp\left[\frac{-E_{f_{AA}}}{k_BT}\right]. \end{aligned} \tag{7.5}$$

The simulations presented in this chapter will consider the temperature to be that of the (non-equilibrium) growth process $T = T_{growth}$. Similarly, in post-growth annealing studies the value of T should match the temperature of the experiment.

By inserting both Equations 7.4 into Equations 7.5, both N_{DD} and N_{AA} can be expressed in terms of the position of E_F

$$\begin{aligned} N_{DD} &= \left(\frac{N_s}{2}\right)\exp\left[\frac{-(E_{f_o} - 2(E_{\mathrm{FS}} - E_F))}{k_BT}\right] \\ N_{AA} &= \left(\frac{N_s}{2}\right)\exp\left[\frac{-(E_{f_o} + 2(E_{\mathrm{FS}} - E_F))}{k_BT}\right]. \end{aligned} \tag{7.6}$$

Independently, n can also be expressed in terms of E_F. The integral form of this relationship (Equation 4.7) has already been used to calculate Burstein-Moss filling in Chapter 4 and the irradiation-stabilized Fermi level in Chapter 5, but in the present situation of $n > 10^{20}\,\mathrm{cm}^{-3}$ degenerate doping the non-integral form (from Equation 1.7)

$$n(E_F) = \frac{1}{3\pi^2}k^3(E_F) \tag{7.7}$$

can be used. For CdO, the nonparabolic dispersion relation given in 2.1.2 is used for $k(E_F)$.

By combining Equations 7.7 (abbreviated here as $n(E_F)$ for space) and the Fermi-level-dependent terms N_{DD} and N_{AA} from Equation 7.6, Equation 7.1 can be rewritten and solved for N_D as a function of E_F such that

$$\begin{aligned} N_D \quad = \quad & \frac{1}{\xi_o}\left(n(E_F) - N_s\exp\left[\frac{-(E_{f_o} - 2(E_{\mathrm{FS}} - E_F))}{k_BT}\right]\right. \\ & \left. + N_s\exp\left[\frac{-(E_{f_o} + 2(E_{\mathrm{FS}} - E_F))}{k_BT}\right]\right). \end{aligned} \tag{7.8}$$

All relevant concentrations can now be solved in terms of E_F: N_{DD} and N_{AA} are each found by Equation 7.6, n by Equation 7.7, and N_D by Equation 7.8, which makes use of the first three terms. Although N_D is the obvious experimental variable, for doping calculations it is E_F that determines all the relevant parameters.

7.1.2 Compensation ratio

The electron and defect concentrations found above can be used to calculate the compensation ratio, a parameter that will allow for the calculation of ionized-impurity-limited mobility $\mu_{\text{ion. imp.}}$ in Section 7.1.3.

The compensation ratio θ is the ratio of ionized acceptors to ionized donors N_A^-/N_D^+. Following Walukiewicz et al. [59], the total number of ionized impurities N_i and n are related via

$$N_i = n\left(\frac{1+\theta}{1-\theta}\right), \tag{7.9}$$

which can be rewritten as

$$\theta = \frac{N_i - n}{N_i + n}. \tag{7.10}$$

It is important to note that N_i is the concentration of singly-ionized impurities. Because θ will be used to calculate the ionized impurity scattering contribution to the mobility, it must account for the charge-squared strength of Coulombic scattering. Ionized impurities of higher charge states are therefore accounted for in N_i by treating them as the charge-squared equivalent number of singly-ionized species. For this reason, in the present case for doubly-ionized native defects and singly-ionized impurity dopants N_i is written

$$N_i = \xi_o N_D + 4N_{DD} + 4N_{AA}. \tag{7.11}$$

Equation 7.10 can be written using the expressions for N_i and n via Equations 7.11 and 7.1 such that

$$\begin{aligned}\theta &= \frac{\xi_o N_D + 4N_{DD} + 4N_{AA} - \xi_o N_D + 2N_{DD} - 2N_{AA}}{\xi_o N_D + 4N_{DD} + 4N_{AA} + \xi_o N_D + 2N_{DD} - 2N_{AA}} && (7.12)\\ &= \frac{2N_{DD} + 6N_{AA}}{2\xi_o N_D + 6N_{DD} + 2N_{AA}} && (7.13)\end{aligned}$$

This result, along with the electron concentration, will enable the calculation of $\mu_{\text{ion. imp.}}$ in the next section.

In the low-doping limit as $N_D \to 0$, the ADM framework predicts that the concentration of compensating acceptors N_{AA} similarly decreases to ~ 0. In this situation

$$\theta = \frac{2N_{DD}}{6N_{DD}} = \frac{1}{3}. \tag{7.14}$$

In the high-doping limit, $N_{DD} \to 0$ and

$$\lim_{N_D \to +\infty} \theta = \frac{6N_{AA}}{2\xi_o N_D + 2N_{AA}}. \tag{7.15}$$

7.1.3 Mobility

The total mobility of doped CdO materials involves contributions from acoustic phonons, polar optical phonons, and ionized impurity (Coulombic) scattering. The conventional approach to considering all mobility-limiting effects is to employ Matthiessen's rule, which finds the reciprocal total mobility by summing the individual reciprocal mobility limits due to the various scattering mechanisms, but such an approach is not well suited to smaller-gap semiconductors with nonparabolic bands. The charge transport and scattering mechanisms in these materials are more appropriately modeled by combining the individual scattering *lifetimes* of each mechanism using variational methods. A complete description of the variational procedure used to calculate the mobility in this section is beyond the scope of the current work. Complete details of the procedure can be found in the works of Szymańska and Dietl [173] and Walukiewicz [50]. An example of their application to III-N alloys can be found in [174]. Details of the Mathematica calculations used in this section are provided in Appendix B.

Following Ref. [174], the individual mobility-limiting mechanisms are illustrated in Figure 7.1 for three different levels of compensation ($\theta = 0$, $\theta = 0.5$, and $\theta = 0.9$). The mobilities are calculated at $T = 300$ K. The individual mechanisms considered by these calculations are piezoelectric scattering from acoustic phonons $\mu_{\mathrm{Piezoelectric}}$, deformation potential mode scattering from acoustic phonons $\mu_{\mathrm{Acoustic\ phon.}}$, scattering from optical phonons $\mu_{\mathrm{Optical\ phon.}}$, and ionized impurity scattering $\mu_{\mathrm{ion\ imp.}}$. At high electron concentrations, regardless of θ, ionized impurity scattering is the limiting factor of the total mobility $\mu_{\mathrm{Total.}}$. In perfectly uncompensated material ($\theta = 0$, Figure 7.1a), the effect of optical phonons and ionized impurities is roughly the same up to $n \sim 10^{20}\,\mathrm{cm}^{-3}$; at higher n, the contribution from $\mu_{\mathrm{ion\ imp.}}$ dominates. In this concentration range, the maximum value of $\mu_{\mathrm{Total}} \sim 340\,\mathrm{cm}^2/\mathrm{Vs}$ at $n = 10^{19}\,\mathrm{cm}^{-3}$ The contribution to the mobility limit from acoustic phonon scattering is very small and will not be considered further. At moderate levels of compensation ($\theta = 0.5$, Figure 7.1b), ionized impurity scattering is the dominant term for $n > 10^{19}\,\mathrm{cm}^{-3}$. In heavily-compensated material ($\theta = 0.9$, Figure 7.1c), ionized impurity scattering severely limits $\mu_{\mathrm{Total.}}$, such that at $n = 10^{19}$, $\mu_{\mathrm{Total}} < 100\,\mathrm{cm}^2/\mathrm{Vs}$.

Grain boundary scattering is not considered in the present analysis, following the work of Metz et al. [175], who find no influence of grain boundary scattering in CdO at concentrations down to ($2 \times 10^{20}\,\mathrm{cm}^{-3}$), the lowest experimentally observed concentration considered in this work. Given the high Fermi level in the samples and the tendency for CdO surfaces to be accumulated, not depleted, the only scattering that should occur at interfaces is caused by momentum change in the wavevector at the Fermi energy that varies relative to CBM. At concentrations below $10^{20}\,\mathrm{cm}^{-3}$ grain boundary scattering may play a significant role in limiting the mobility although the threshold concentration for this behavior has not been investigated experimentally for CdO.

The relationship between the total electron mobility μ_{Total}, electron concentration n, and compensation ratio θ is summarized in the contour plot shown in Figure 7.2. This calculated curve provides all of the necessary information to calculate the mobility based on

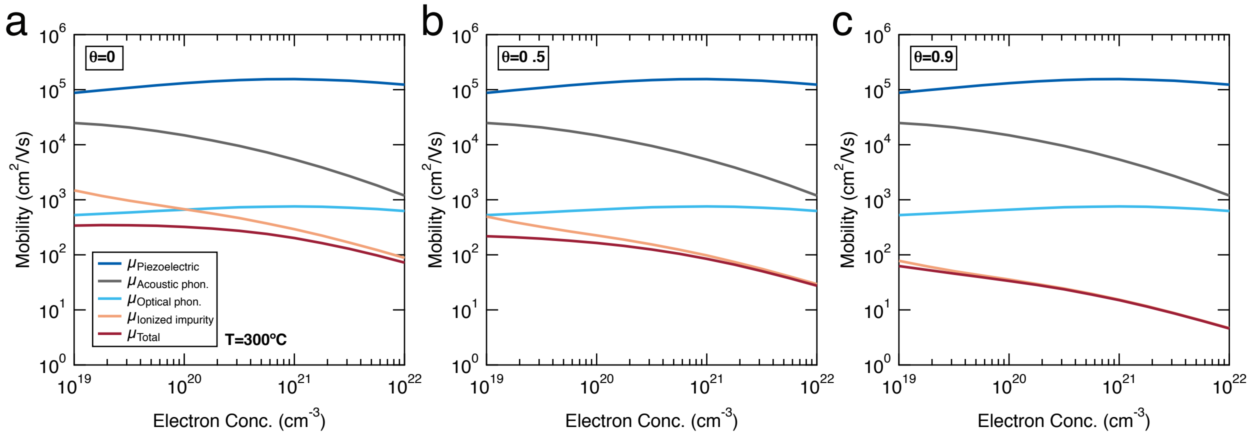

Figure 7.1: Individual scattering mechanisms—piezoelectric-mode and deformation-mode scattering from acoustic phonons, Coulombic scattering from ionized centers, and scattering from optical phonons—contribute to the total calculated mobility in CdO, shown here as a function of electron concentration for compensation ratios $\theta = 0$, $\theta = 0.5$, and $\theta = 0.9$ at $T = 300$ K. (a) In perfectly uncompensated material ($\theta = 0$) optical phonons play a larger role than ionized impurities in limiting the mobility up to $n \sim 10^{20}\,\text{cm}^{-3}$. (b) At moderate compensation values ($\theta = 0.5$), this crossover occurs at $n \sim 10^{19}\text{cm}^{-3}$. (c) For heavily-compensated material ($\theta = 0.9$), ionized impurity scattering dominates throughout the concentration range.

the concentration and compensation values obtained in Sections 7.1 and 7.1.2.

7.2 Comparison of simulation and experiment

In this section, the results of the concentration and mobility calculations based on the ADM are compared with a set of doped CdO:Ga samples deposited by RF magnetron sputtering on glass substrates at $T = 270°\text{C}$.

In Figure 7.3, the electrical properties of doped-CdO films are simulated as a function of the concentration of impurity dopants N_D for different values of the formation energy of native defects at E_{FS}, $0.3 < E_{f_o} < 1.8$. In Figure 7.3a, the electron concentration n is plotted and compared to experimental Hall effect results. The simulated results for $E_{f_o} \approx 1 - 1.2$ eV are a good match to the experimental data. The electron concentration saturates to $n \sim 2 \times 10^{20}\,\text{cm}^{-3}$ for low values of N_D, the same value typically observed in nominally undoped CdO films, as discussed in Section 2.1.3. The origin of this saturation is shown in Figure 7.3, as the concentration of native donors increases significantly with the electron concentration, a result of the Fermi-level-dependent formation energy of the defect in the ADM. Conversely, at high values of N_D, compensating acceptors limit the electron to

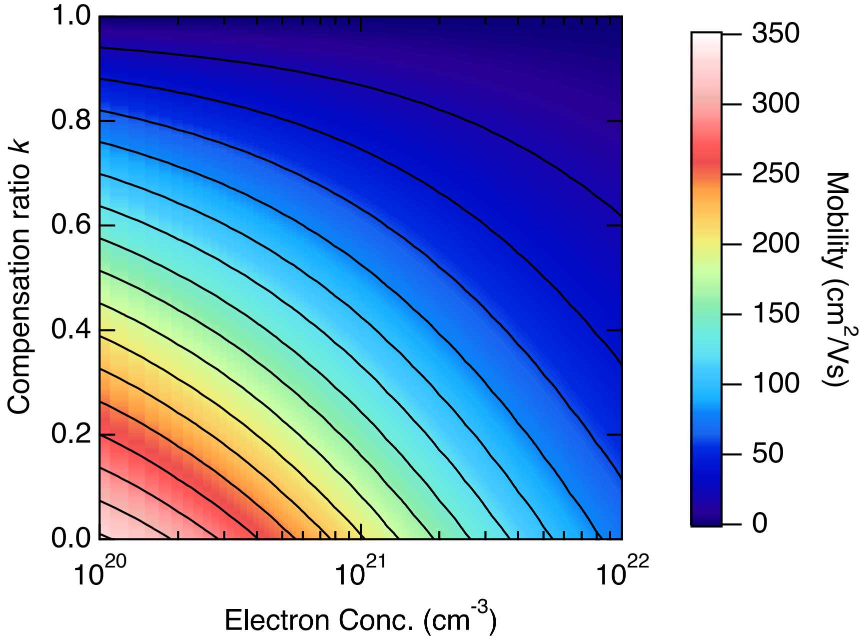

Figure 7.2: Total electron mobility μ_{Total} as a function of carrier concentration n and compensation ratio θ calculated at $T = 300$ K, following methods from Refs. [174, 50]. The concentration and compensation values determined by the ADM calculations can be used in conjunction with this plot to predict μ_{Total} for a given impurity doping concentration N_D.

$n \sim 1 \times 10^{21}\,\text{cm}^{-3}$, even as $N_D \sim 4 \times 10^{21}\,\text{cm}^{-3}$. Near E_{FS}, the simulated doping behavior is linear and 1:1, although it appears that the simulated vales for n are all slightly higher than the experimental values. This may arise due to additional acceptor impurities, as will be discussed below, or may be due to non-unity values of dopant activation ξ_o.

The calculated compensation ratio is shown in Figure 7.3c. Notably, the compensation ratio decreases with additional impurity doping as E_F approaches E_{FS}, then increases dramatically with the increasing concentration of doubly-charged compensating acceptors. This region of low compensation corresponds to the 1:1 doping regime observed in Figure 7.3a. The mobility, shown in Figure 7.3d, correspondingly increases with N_A up to the point that θ begins increasing as E_F moves through E_{FS}, where $N_D \approx 5 \times 10^{20}$. This decrease in compensation and increase with doping is a peculiar feature of the extreme band alignments of CdO. Similar behavior has been observed in Figure 2.3 from Ref. [19] for the case of In-doped CdO.

At high n, the simulated mobility agrees well with the experimental values, but at low n the simulation predicts a mobility limit of $\sim 200 - 300\,\text{cm}^2/\text{Vs}$ for $n \sim 10^{20} - 10^{21}$ while the experimental values fall in the range of $\sim 100 - 150\,\text{cm}^2/\text{Vs}$. While several Fermi-level-dependent scattering mechanisms could account for this behavior, the previous results reported by Yu et al. [19] in Figure 2.3 suggest that compensation in nominally-undoped CdO results in $\theta \sim 0.7$. This value is more than twice the 1/3 limit suggested by Equation 7.14. A background concentration of acceptor impurities is one physical explanation that could account for such a difference. If a singly-ionized acceptor concentration N_A is included in Equations 7.1 and 7.11, the new compensation ratio θ is

$$\theta = \frac{2N_{DD} + 6N_{AA} + 2N_A}{2\xi_o N_D + 6N_{DD} + 2N_{AA}}. \tag{7.16}$$

In the low-doping-limit as $N_D \to 0$, θ is no longer constant and its value instead depends on N_A.

Figure 7.4 presents the electrical properties of doped-CdO as a function of N_D calculated for different values of the concentration of impurity acceptors $N_A \sim 10^{19} - 10^{21}\,\mathrm{cm}^{-3}$, using the same experimental concentration and mobility data from Figure 7.3. Based on the results from Figure 7.3, a value of $E_{f_o} = 1\,\mathrm{eV}$ is chosen for the defect formation energy at E_{FS}. The electron concentration, shown in Figure 7.4a, decreases with additional N_A content, moving the linear doping regime to higher N_D values. Away from $E_F \approx E_{\mathrm{FS}}$, the electrical behavior is dominated by the native defect concentrations shown in Figure 7.4b. The compensation ratio (Figure 7.4c) follows Equation 7.16, with a low-doping limit to θ that is no longer constant at low N_D values but instead is dependent on the concentration of N_A. The total mobility $\mu_{\mathrm{Total.}}$ is significantly reduced with increasing N_A although it still exhibits a rise with donor concentration N_D while E_F is near E_{FS}. The best fit to the mobility data is achieved with $N_A \sim 5 - 6 \times 10^{20}\,\mathrm{cm}^{-3}$, although other scattering mechanisms may also contribute to this behavior at low n. Given the high Fermi level and the likely electron accumulation at grain boundaries in CdO the conventional model of grain boundary scattering is not applicable, although secondary effects due to charged trap states could influence the mobility in a way that is consistent with the behavior modeled here using impurity acceptors.

The calculations and results in this chapter are based on the phenomenological framework of the ADM and reflect a picture of dopants and defects that are based on thermodynamics at equilibrium, but nonetheless present a useful picture for predicting ultimate doping limits. In future work, temperature-dependent transport could be used to differentiate scattering mechanisms at low doping concentrations.

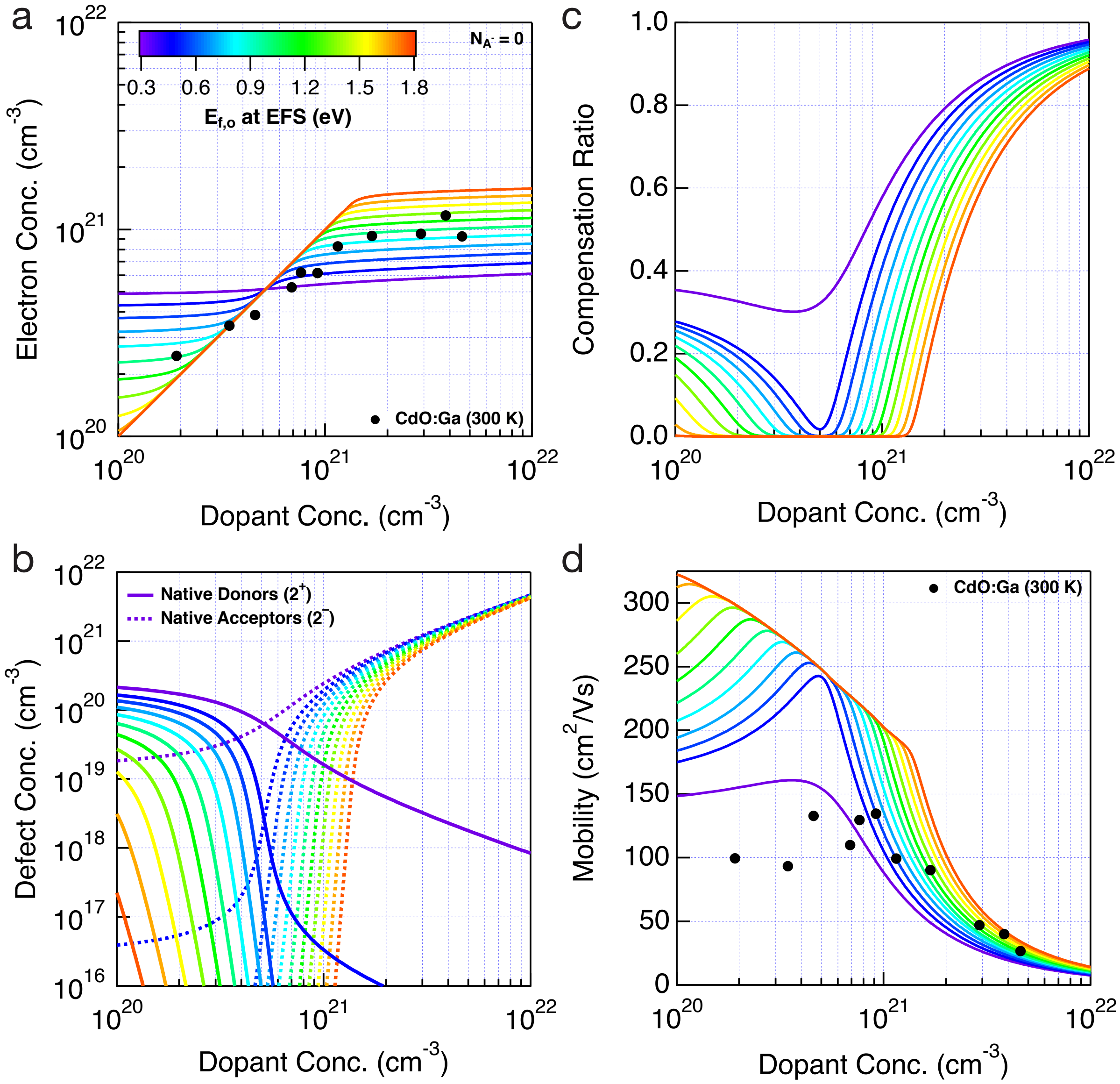

Figure 7.3: Electrical properties of doped-CdO as a function of impurity dopant concentration N_D calculated with different values of the formation energy of native acceptors at E_{FS} E_{f_o}. Experimental CdO:Ga data are included for comparison. (a) The simulated electron concentration n shows good agreement with $E_{f_o} \approx 1-1.2$ eV. The concentration at $N_D \to 0$ matches well with the experimentally observed electron of $n \sim 2 \times 10^{20}\,\text{cm}^{-3}$. (b) The concentration of doubly-ionized native donors N_{DD} and acceptors N_{AA} drops significantly in the 1:1 doping range seen near $2 \times 10^{20} < N_D < 1 \times 10^{21}$ cm^{-3}. (c) The compensation ratio drops up to the point that $E_F \approx E_{\text{FS}}$. (d) The total electron mobility calculations show good agreement $N_D > 10^{21}$ cm^{-3} but overestimate the mobility at lower doping levels. An increase in simulated mobility up to $N_D \approx 5 \times 10^{20}$ is the result of a decrease in the compensation ratio.

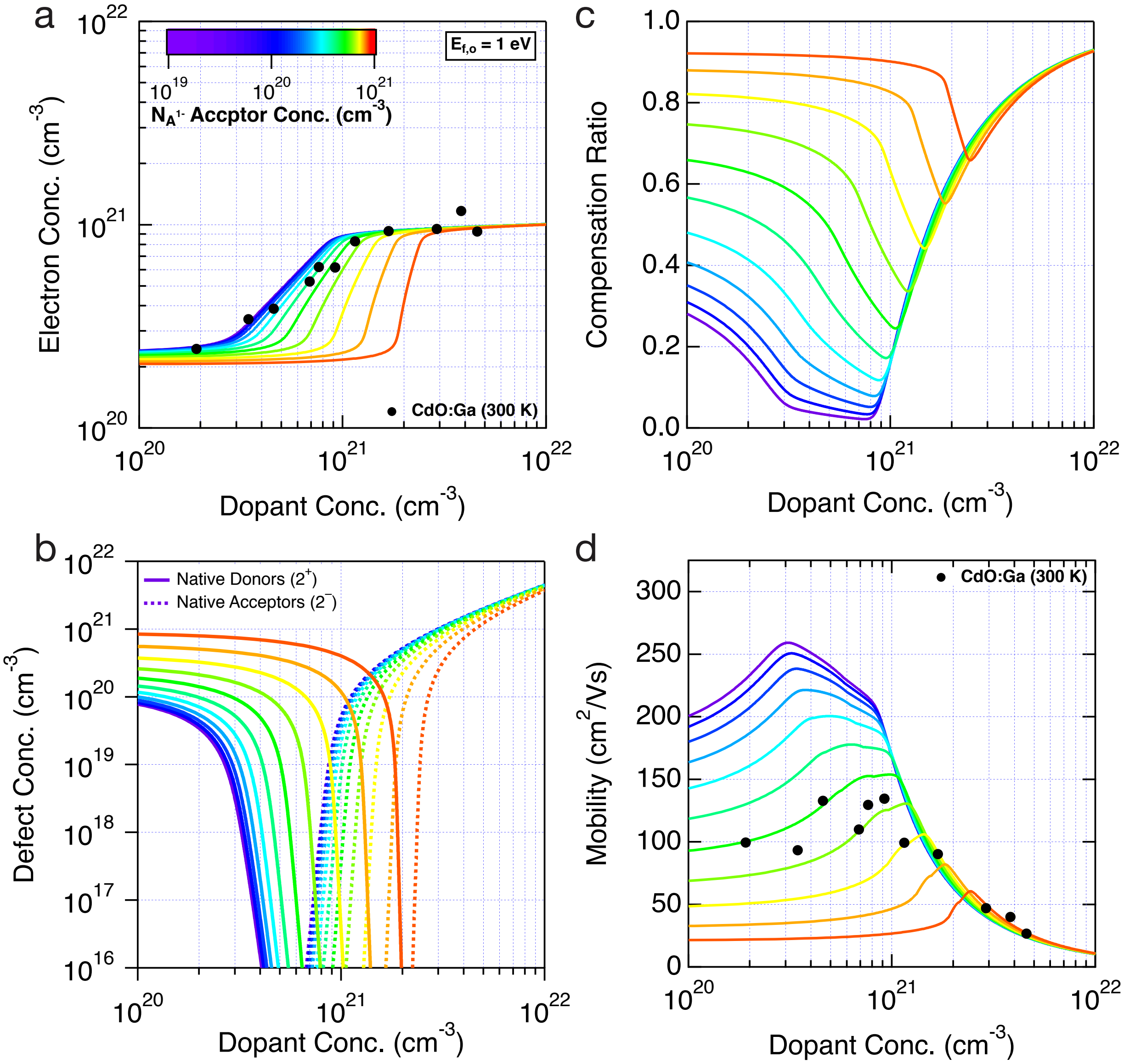

Figure 7.4: Electrical properties of doped-CdO as a function of impurity dopant concentration N_D, calculated with varying concentration of singly-ionized background acceptor impurities N_A. The results are compared with experimental CdO:Ga data. A formation energy value of $E_{f_o} = 1\,\text{eV}$ is chosen based on the results in 7.3. (a) The additional compensating acceptor concentration decreases n, such that 1:1 doping is no longer observed near $E_F \approx E_{\text{FS}}$. (b) The concentration of doubly-ionized native donors N_{DD} increases with increasing N_A due to compensation effects lowering the Fermi level. N_{AA} is slightly reduced. (c) The compensation ratio follows Equation 7.16, with a low-doping limit to θ that varies with N_A. (d) The mobility at low n corresponds to a simulated value of $\mu_{\text{Total.}}$ for $N_A \sim 5 - 6 \times 10^{20}\,\text{cm}^{-3}$.

Chapter 8

Conclusions and future work

Metal oxides are promising materials for many optoelectronic applications and represent an area of intense research interest. The successful development of oxide-based semiconductor devices requires a thorough understanding of their fundamental structural and optoelectronic properties. In particular, it is critical to understand how these properties can be tuned to meet device needs. Furthermore, because metal-oxide alloys are often seen to have a high concentration of inherent defects, and because endpoint compounds of II-oxide alloy systems may be structurally mismatched, the development and optimization of oxide thin film and nanostructure processing techniques is essential for the successful implementation of these materials in device applications.

TCOs, which comprise all industrially relevant transparent TC technologies, are intriguing metal oxides that offer simultaneously good transparency and good electrical conductivity, at least in theory. The reality is that astonishingly few materials can achieve a remotely acceptable compromise between these two properties, as fundamental optical processes degrade the transparency of heavily-doped semiconductors. This transparency limit arises from the electron mobility, which is significantly degraded by doping (except, as seen in Chapter 7, in the case of materials with band offsets like those of CdO) via ionized impurity scattering. In addition, fundamental doping limits that arise from compensating native defect behavior ultimately limit the conductivity of most semiconductors to a point where they are too resistive to act as TCs for most applications. In some metal oxides, such as AZO and ITO, the heavy doping leads to conductivity that is sufficient for them to be used in display, LED, and PV applications that do not require broad-spectrum transparency.

CdO is a high-mobility metal oxide that possesses high doping limits and extreme band offsets. Its high mobility alleviates—although it does not eliminate—the strict tradeoffs between optical transparency described in Chapter 1. While its electrical performance is superior to that of other TCOs, its optical performance at short wavelengths is limited by its low fundamental direct gap of 2.2 eV. Bandgap engineering and doping (via the Burstein-Moss effect) are both viable routes to increasing this short-wavelength transparency, but to date there have been few reports of bandgap engineering of this system.

The need to understand how and whether the electrical and optical properties of CdO can be improved by alloying and doping motivates the work presented in this dissertation. The experimental work and analysis presented in Chapters 3, 4, and 5 has connected the unique electrical, optical, structural, and band offset properties of $Cd_xZn_{1-x}O$ alloys over the entire composition range. The results elucidate the composition dependence of the energy of the VBM and CBM and indicate that the VBM of $Cd_xZn_{1-x}O$ alloys exhibits an increase in energy with Cd content, a behavior that is not normally observed in oxide alloys, where valence bands are derived primarily from the $2p$ states of oxygen.

As discussed in Chapter 6, this unique property makes the $Cd_xZn_{1-x}O$ alloy system uniquely suited to the requirements of a PEC photoanode in a tandem semiconductor heterojunction device for spontaneous water splitting. In this case, the two property regimes created by the structural mismatch of WZ-ZnO and RS-CdO are well suited to the needs of a photoanode. The WZ absorber layer exhibits strong, direct-gap absorption that is tunable over the visible range, and its CBM is well-positioned to make ohmic contact to the p-type silicon layer of the underlying PV layer. Holes that are generated in the graded WZ layer are swept to the surface by the upward rise in the VBM. There, they enter the RS layer, where they should exhibit longer hole lifetimes due to the presence of the indirect gap at the L-point VBM.

In Chapter 7, the unique doping behavior and electrical properties of CdO have been explored via simulations based on the amphoteric defect model. The calculations, despite being based on equilibrium thermodynamics, can offer insight into the transport characteristics of doped CdO films grown by nonequilibrium processes. However, they will require further refinement, including the consideration of the contribution of grain-boundary scattering to the mobility.

8.1 Future work

There are two key areas of future work that are direct extensions of the work presented in this dissertation: the synthesis and characterization of doped $Cd_xZn_{1-x}O$ films and the validation of the PEC device design in Chapter 6.

The doping performance of $Cd_xZn_{1-x}O$ alloys needs to be explored more extensively. Preliminary doping studies of sputtered $Cd_xZn_{1-x}O$ films presented in Section A.3.1 suggest that the mobility increase observed in CdO:In in Ref [19] may not exist for In-doped RS-$Cd_xZn_{1-x}O$ alloys. Overall, the electron mobilities of sputtered films are observed to be lower, which suggests that structural quality and dopant activation may be lower in these materials. An extension of this work is the application of doped $Cd_xZn_{1-x}O$ as a TCO layer in a PV device.

The development of a $Cd_xZn_{1-x}O$-based tandem PEC will further investigations of the device and materials properties of $Cd_xZn_{1-x}O$. First, the vertical transport characteristics of $Cd_xZn_{1-x}O$ on Si must be evaluated to ensure that ohmic contact can be made to the PV layer. Second, the composition of the WZ absorber layer must be modeled to ensure current matching with the underlying layer. Third, further lifetime measurements must be carried out to confirm the lifetime of holes in the indirect-gap top layer. The construction and photoelectrochemical testing of such a PEC device presents a significant engineering challenge, but the basic properties of $Cd_xZn_{1-x}O$ alloys offer plenty of hope that such a device is possible.

There are several "next steps" in the development of CdO-based alloys beyond the further investigation of $Cd_xZn_{1-x}O$. Alloying with transition metal oxides based on Ni- and V-based compounds, which possess localized *d* donor levels near the CBM of CdO, may provide another route to engineering the electronic structure of CdO via band anticrossing effects. In addition, as suggested by the band offset figure in A.1, NiO may exhibit band offsets that are in extreme contrast to those of CdO. The two materials exhibit an extreme type-III offset. More broadly, the extreme band positioning of CdO offers many possibilities for novel devices structures, alloying, and interface studies. The contribution from this dissertation work has followed one such thread, revealing novel physical behavior and motivating future work in the exploration of novel oxide materials and devices.

Appendix A

Additional data and figures

A.1 Band offsets of various semiconductors

The collected band offsets of semiconductors, compiled from experiment and first-principles calculations in Refs. [51, 67, 75, 90, 155], are shown in Figure A.1. On the same absolute scale, the oxidation and reduction potentials for water splitting are shown, assuming pH= 2, following the work by Bak et al. [165] and Mayer et al. [102]. The position of position cation *d* donor and acceptor levels is included, using data from Vesely and Langer [90].

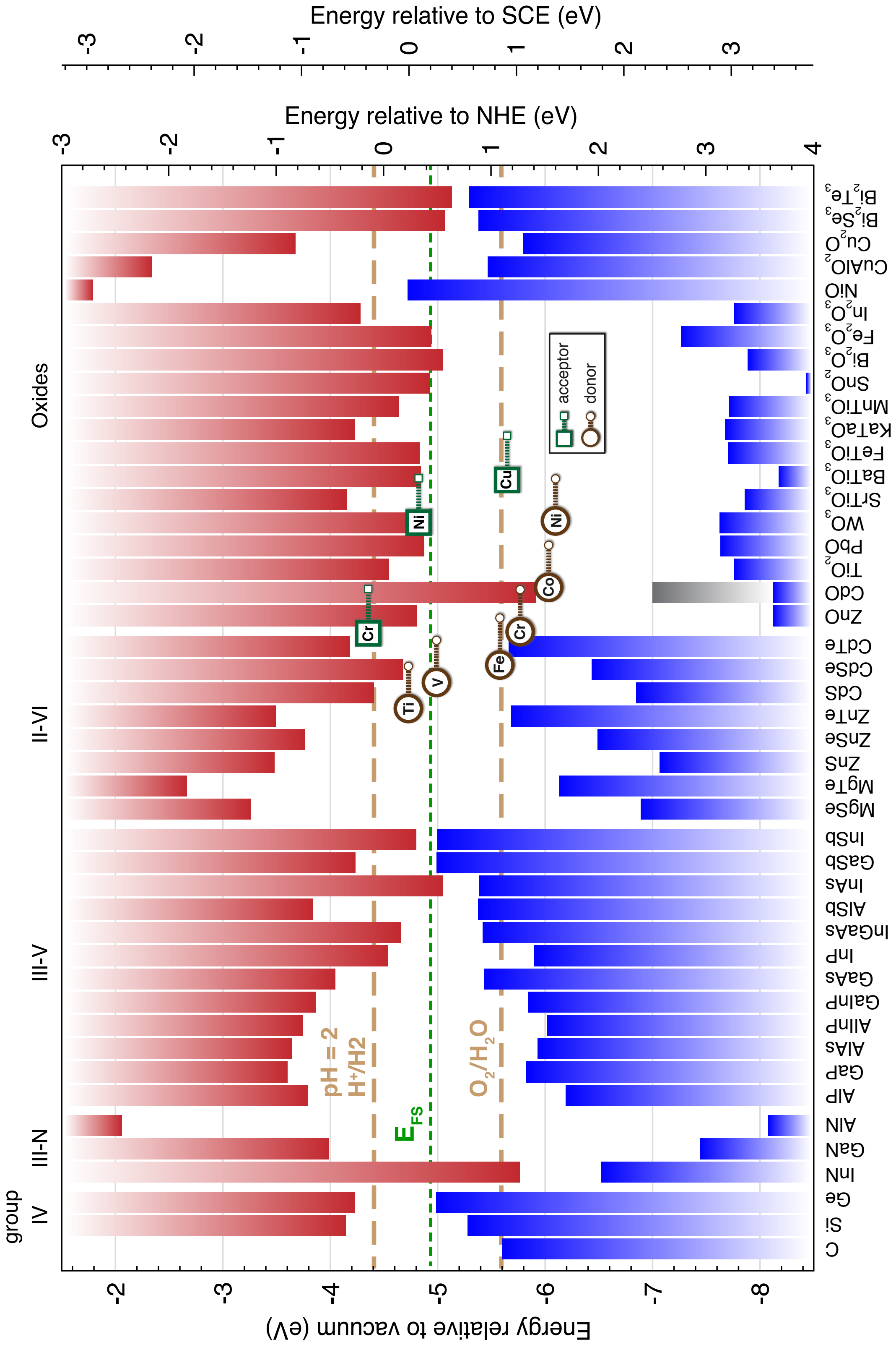

Figure A.1: Collected band offsets of semiconductors along with water-splitting redox potentials and position of cation *d* levels. Compiled from Refs. [51, 67, 75, 90, 102, 155, 165].

A.2 Rutherford backscattering spectrometry

A.2.1 Example fitting procedure for $Cd_xZn_{1-x}O$ thin films

Rutherford backscattering spectrometry (RBS) is a non-destructive technique that can be used to determine the thickness and composition of thin film samples. Figure A.2, provides and example of how RBS data can be simulated using the SIMNRA [140] and SIMTARGET [141] software packages. A sample structure (Figure A.2a) is defined using SIMTARGET and used as an input for the SIMNRA simulation package, which calculates the backscattered spectra (Figure A.2b) based on the experimental conditions of the incident He-ion beam and spectrometer.

The composition of the $Cd_xZn_{1-x}O$ film is analyzed such that the composition value in the RBS target is a fraction of the total atomic density (including oxygen), rather than that of just the cation sites. For this reason the value of x is twice the value seen in the RBS target simulation. The fitting procedure involves first determining the beam energy (nominally 3 MeV) by fitting the prominent oxygen resonance peak near 500 keV. The substrate data (here, the spectra at energies < 1200 keV) is then used a reference to fit the other experimental conditions. Finally, the input sample structure (including thickness, composition, and interface roughness) is varied to match the film peaks. A complete discussion of RBS data analysis is beyond the scope of this work but can be found in Ref. [176].

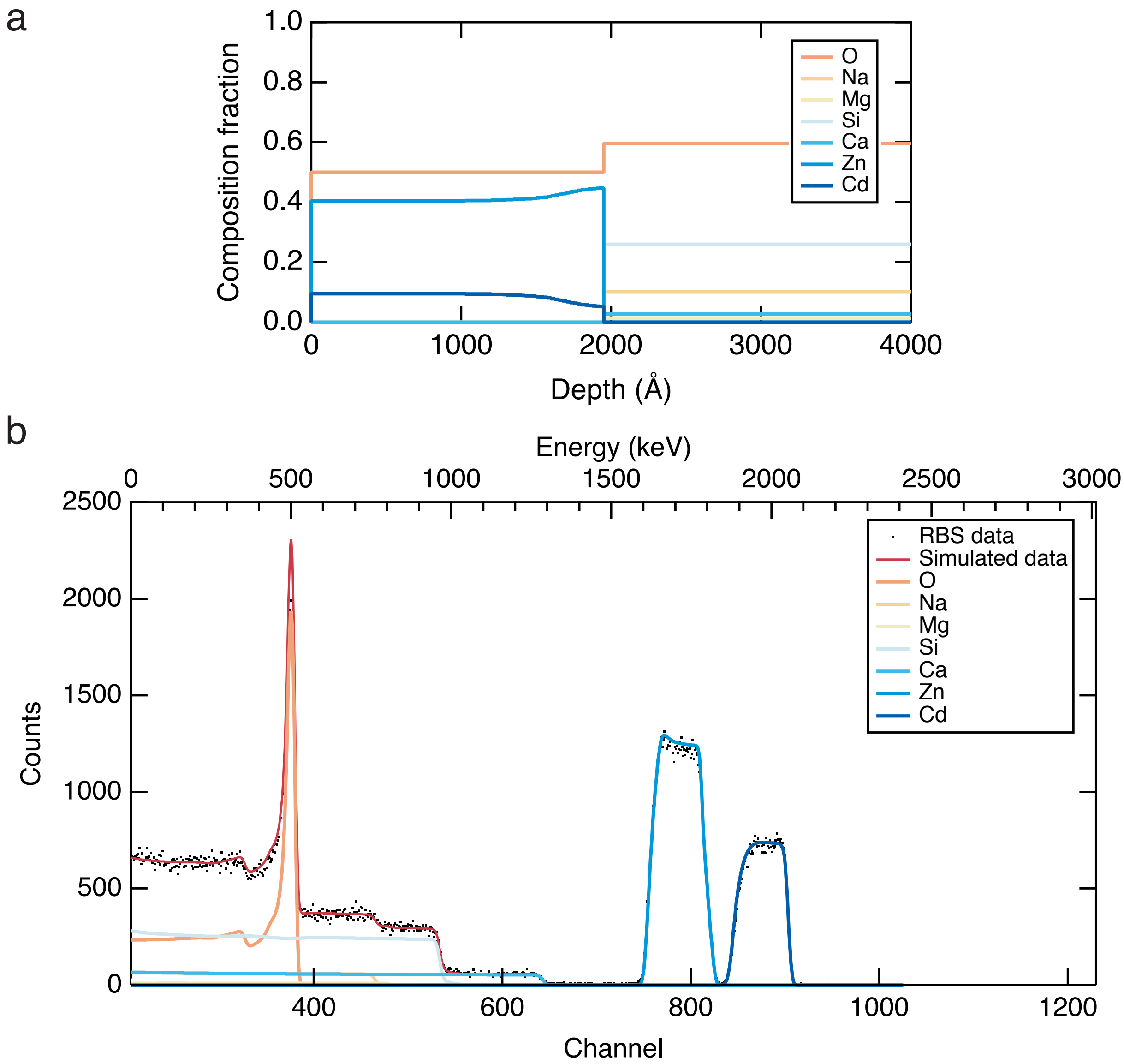

Figure A.2: Example of RBS data analysis of a Cd$_x$Zn$_{1\text{-}x}$O sample ($x = 0.19$ using SIMNRA [140] and SIMTARGET [141] (a) The sample structure, modeled using SIMTARGET, is used as an input to the simulation package SIMNRA along with the experimental conditions of the beam and spectrometer. (b) The resulting simulated elemental RBS spectra are shown along with experimental RBS data (points). The Cd$_x$Zn$_{1\text{-}x}$O thin film is modeled to have a slight composition gradient at the interface between the glass substrate and the growing thin film.

A.3 Additional electrical measurements

A.3.1 Hall effect of $Cd_xZn_{1-x}O$ and $Cd_xZn_{1-x}O$:In films grown by RF magnetron sputtering

In Figure A.3, the electrical properties of $Cd_xZn_{1-x}O$ films deposited RF-magnetron co-sputtering of CdO/ZnO targets are compared to those of PFCAD films. The sputtered films were deposited using Ar gas at 170°C. The composition was controlled by changing the target powers from 0 to 160 W (CdO) and 0 to 120 W (ZnO). The phase transition point observed for PFCAD samples is indicated by the vertical line. Zn-rich samples below $x = 0.4$ were too resistive to measure. The more shallow rise in the mobility with composition and the higher electron concentration for high-Cd-content WZ samples suggests that the sputtered alloys exhibit a higher degree of phase separation.

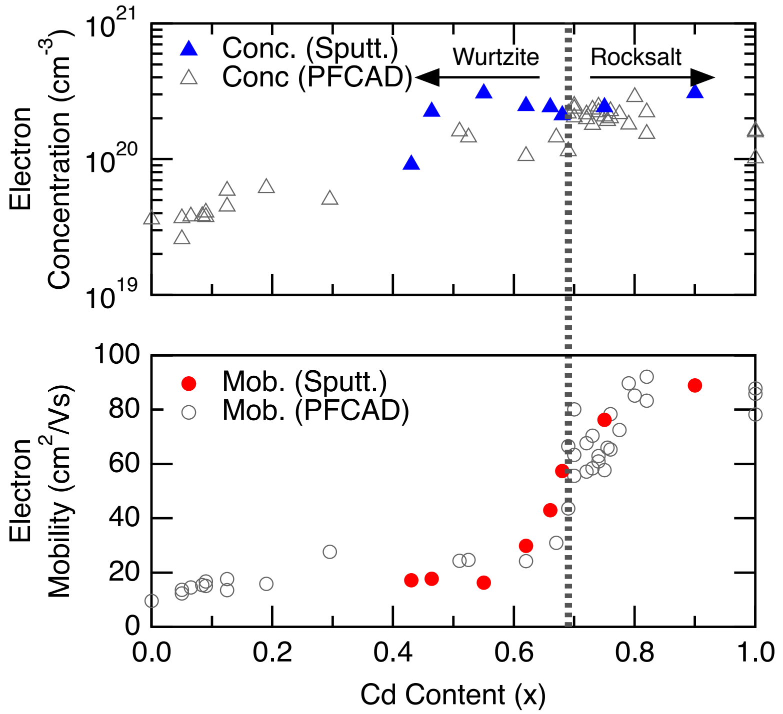

Figure A.3: The electrical properties of $Cd_xZn_{1-x}O$ films from RF-magnetron co-sputtering of CdO/ZnO targets compared to those of PFCAD films. The phase transition point observed for PFCAD samples is indicated by the vertical line. (a) The higher electron concentration of high Cd-content WZ-$Cd_xZn_{1-x}O$ films suggests that the phase transition point in sputtered films may occur at lower Cd-content. (b) The step-increase in the mobility in sputtered samples is more gradual than in the PFCAD case.

A.4 Fitting optical absorption

In the case of semiconductors that have parabolic bands and that are not degenerately-doped, free carriers in the conduction band have no appreciable effect on the position of the direct-gap absorption edge. Following Equation 4.2 and Ref. [144], the absorption edge from an allowed direct-bandgap transition leads to a rise in the absorption edge that depends on $\sqrt{E}$. The bandgap energy can be readily extracted by plotting α^2 vs E and taking an linear extrapolation to the horizontal axis.

Although neither of the above criteria (parabolic bands, nondegenerate doping) applies in the case of $\mathrm{Cd_xZn_{1\text{-}x}O}$ alloys, as a practical matter it is still possible (and often advisable) to estimate the bandgap in such materials using α^2 plots. As illustrated in Figure 1.2, the onset of direct-bandgap absorption is shifted by the Fermi level relative to the CBM (the Burstein-Moss E_{BM} shift discussed in Section 1.3.2). The rising edge of the absorption in this case does not follow a square-root dependence, but nonetheless an α^2 allows one to identify this BM-shifted energy E_g^{opt}. Using the measured carrier concentration, knowledge of the correct dispersion relations (including those of the valence band, from which the blueshift E_{VB} is derived), and the concentration-dependent bandgap renormalization parameters E_{e-e} and $E_{\text{ion}-e}$ (see Section 4.5.1), one can estimate the bandgap E_g by the following expression

$$E_g^{opt} = E_g + E_{BM} - E_{e-e} - E_{\text{ion}-e} + E_{VB}, \tag{A.1}$$

such that all parameters are applied as additive or subtractive shifts to E_g^{opt}. The fitting procedure used in Section 4.5.1 similarly corrects for these terms using rigid energy shifts, but (in theory) offers a better model for fitting carrier-filled bands. Alternate models for fitting that rely on fitting to the first derivate of alpha have been proposed by Makino et al. [177] and Segura et al. [146].

Figure A.4 presents α^2 vs E plots for $\mathrm{Cd_xZn_{1\text{-}x}O}$ films. The general compositional trends in the bandgap are readily apparent, but linear extrapolations of these curves overestimate the value of E_g.

As described in Section 4.5, the energy-dependent absorption coefficient $\alpha(E)$ can be calculated as the convolution of the Fermi-level shifted absorption with a Gaussian function of width Δ to account for experimental broadening so that

$$\alpha(E) = \frac{1}{\Delta\sqrt{\pi}} \int_{-\infty}^{\infty} \alpha_0 (E' - E_g^o)^{\frac{1}{2}} \left[1 + \exp\left(\frac{E_F - E'}{k_B T}\right)\right]^{-1} \times \exp\left[-\left(\frac{E' - E}{\Delta}\right)^2\right] dE', \tag{A.2}$$

where α_0 is an absorption constant and E_g^o is the Burstein-Moss-corrected direct bandgap, as yet uncorrected for the carrier-induced renormalization shifts discussed below.

An example of this fitting procedure applied to the case of a $\mathrm{Cd_xZn_{1\text{-}x}O}$ sample with $x = 0.82$ is shown Figure A.5. Here, $\alpha_0 = 1.45 \times 10^5$ cm^{-1}, $E_g^o = 2.41$ eV, and $E_F = 0.45$ eV. The bandgap renormalization values for this sample, with $n = 1.5 \times 10^{20}$ cm^{-3} result in a final E_g of ~ 2.5 eV.

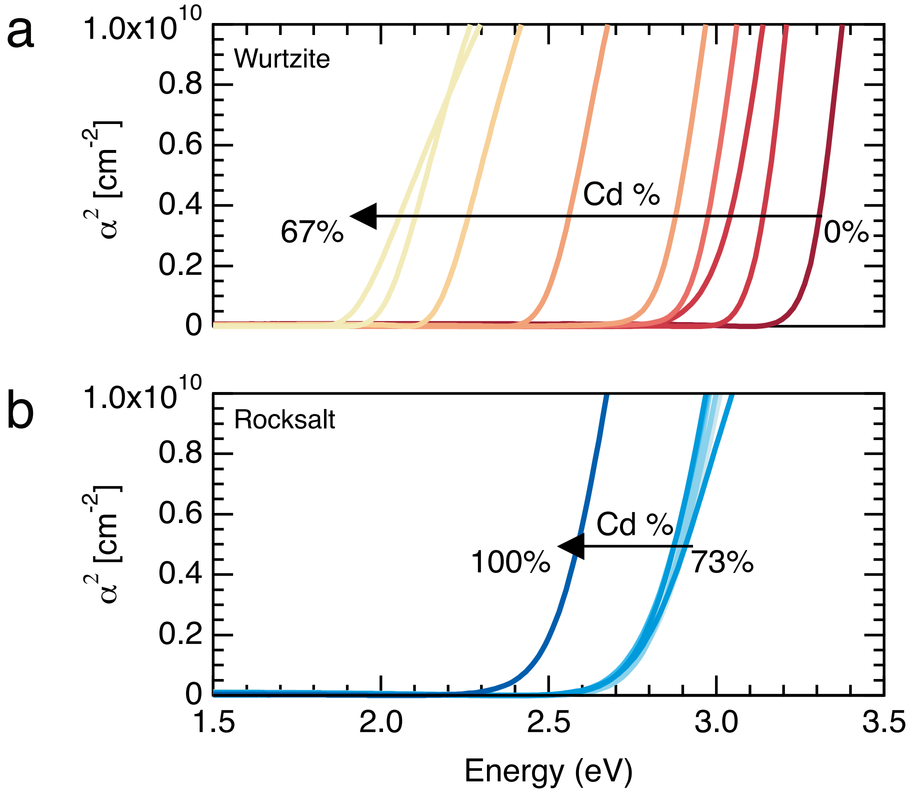

Figure A.4: α^2 vs. E plots for (a) WZ and (b) RS $\mathrm{Cd_xZn_{1\text{-}x}O}$ films.

In Figure A.6, the results of the fitting procedure described by Equation 4.6 in Chapter 4 are compared with those using traditional α^2 vs E to find E_g^{opt}, with additive and subtractive corrections applied following Equation 1.10

$$E_g^{opt} = E_g + E_{BM} + E_{vb} - E_{\mathrm{renorm.}}, \tag{A.3}$$

to extract the intrinsic gap E_g.

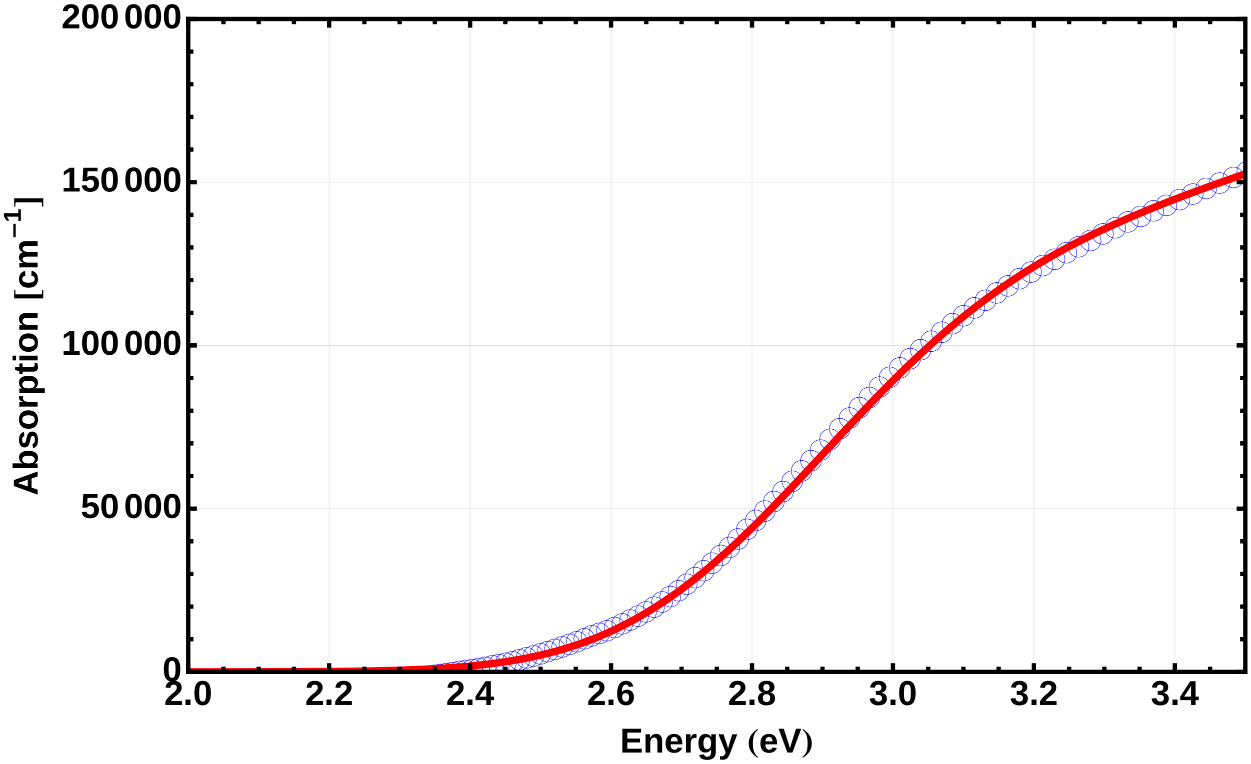

Figure A.5: An example of the absorption fitting procedure for a $\mathrm{Cd_xZn_{1\text{-}x}O}$ sample with $x = 0.82$ following Equation 4.6, with $\alpha_0 = 1.45\times10^5$ cm^{-1}, $E_g^o = 2.41$ eV, and $E_F = 0.45$ eV, along with optical absorption data (circles) calculated from experimental T(E) and R(E) data.

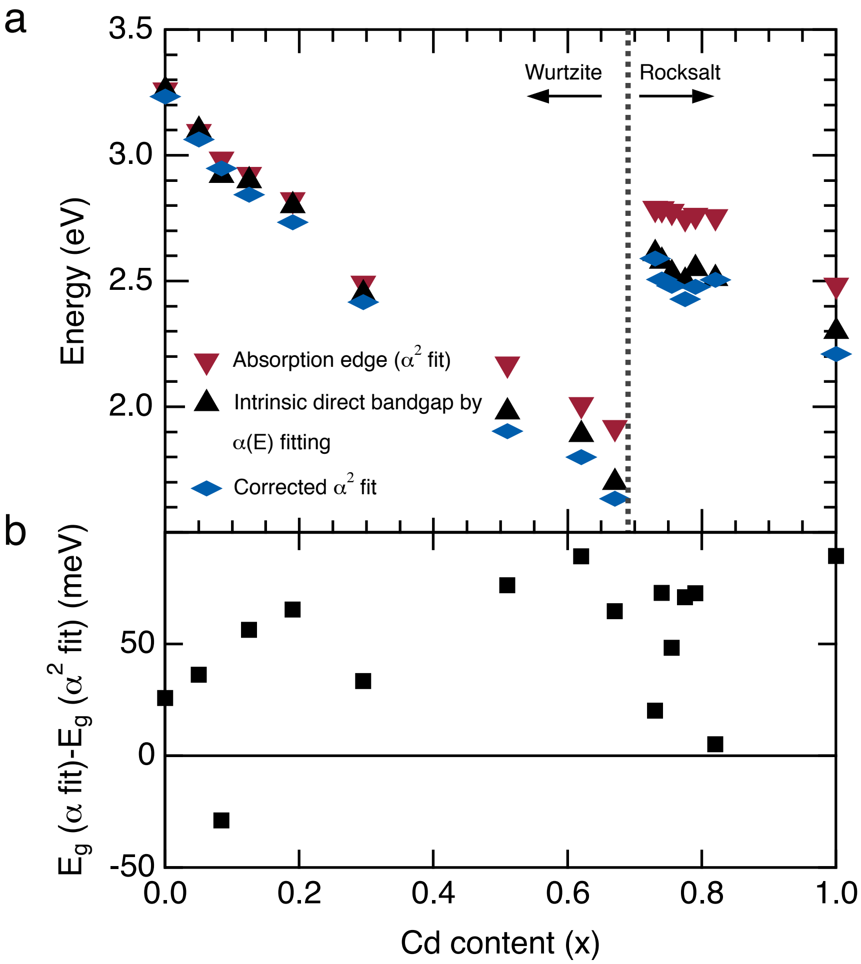

Figure A.6: (a) A comparison of the bandgap values derived from $\alpha(E)$ fitting vs those extracted from traditional α^2 vs E fitting with additional additive/subtractive corrections for carrier-induced shifts. (b) The modified $\alpha(E)$ fitting procedure used in this work yields bandgap values ~ 50 meV higher than the α^2 fits.

A.5 Carrier-induced absorption-edge shifts

Following the renormalization calculations described by Section 4.5.1 and the experimentally determined electron concentrations presented in Section 4.2, Figure A.7 shows the concentration-dependent red- and blue-shifts to the absorption edge.

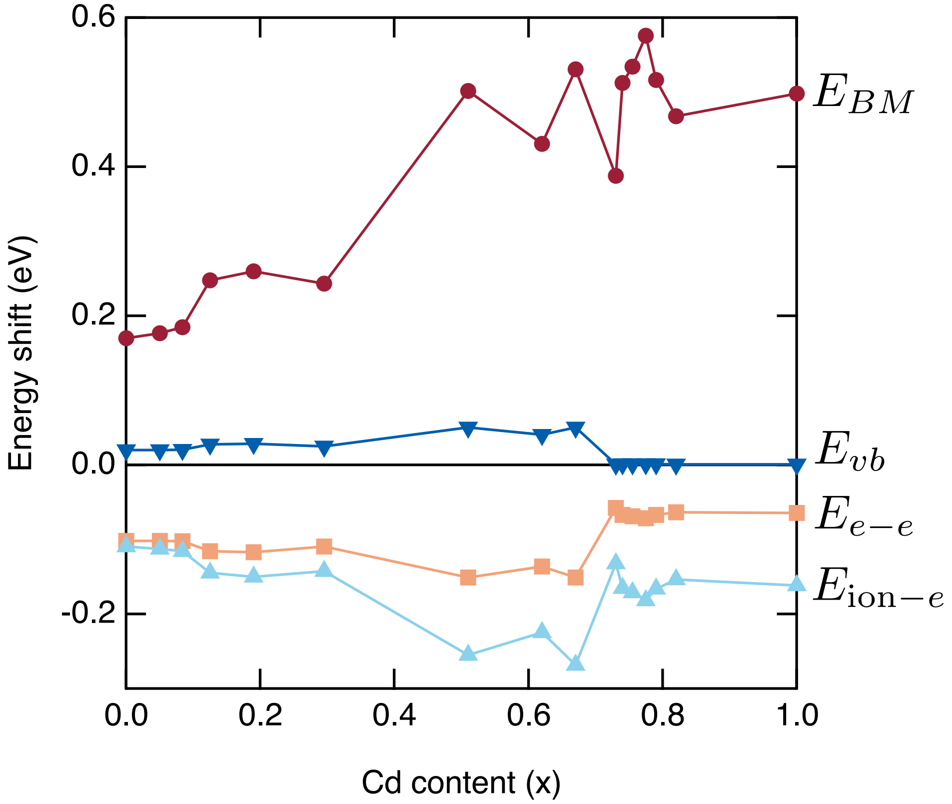

Figure A.7: Values of the electron-concentration-dependent bandgap renormalization effects for $Cd_xZn_{1-x}O$ films as a function of Cd content. The values are calculated according to the equations outlined in Section 4.5.1 and make use of the electron concentration values presented in Section 4.2. For RS films ($x > 0.69$), the valence band dispersion is assumed to be locally flat and the resulting blueshift is negligible.

A.6 Photoluminescence instrument response function

Raw photoluminescence data is normalized by the relative sensitivity of the photomultiplier tube (PMT) detector instrument response function shown in Figure A.8. The instrument response function is measured using an incandescent lamp of known blackbody spectral irradiance for a given set of operating conditions.

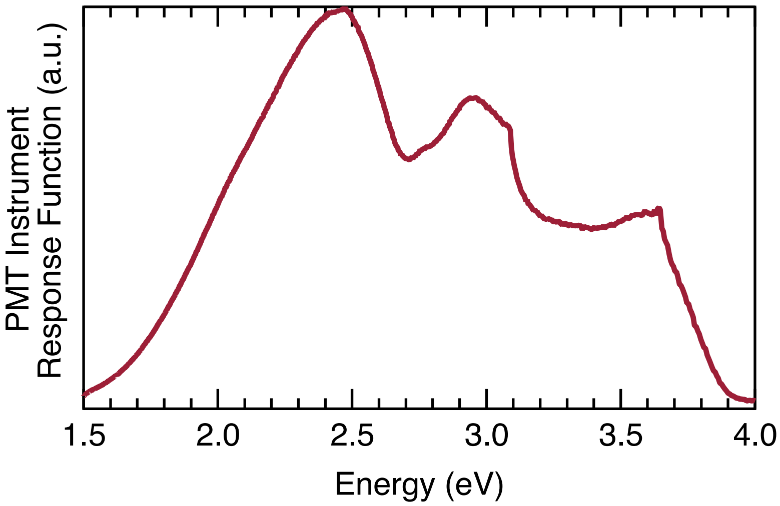

Figure A.8: (a) A comparison of the bandgap values derived from $\alpha(E)$ fitting vs those extracted from traditional α^2 vs E fitting with additional additive/subtractive corrections for carrier-induced shifts. (b) The modified $\alpha(E)$ fitting procedure used in this work yields bandgap values ~ 50 meV higher than the α^2 fits.

A.7 Irradiation data and simulation

A.7.1 SRIM calculations

The end-of-range damage for irradiation experiments is assessed using the Stopping Range of Ions in Matter (SRIM) software package. This Monte-Carlo-based simulation technique can be used to assess damage (vacancy) creation and implantation depths. In the examples provided in Figure A.9, an implantation depth is calculated for 120 keV Ne^+ ion irradiation into 100 nm (Figure A.9a) CdO and ZnO (Figure A.9b) thin films on glass substrates. The end-of-range damage is located in the substrate, and as a result the point-defect creation within the $Cd_xZn_{1-x}O$ films is predicted to be uniform.

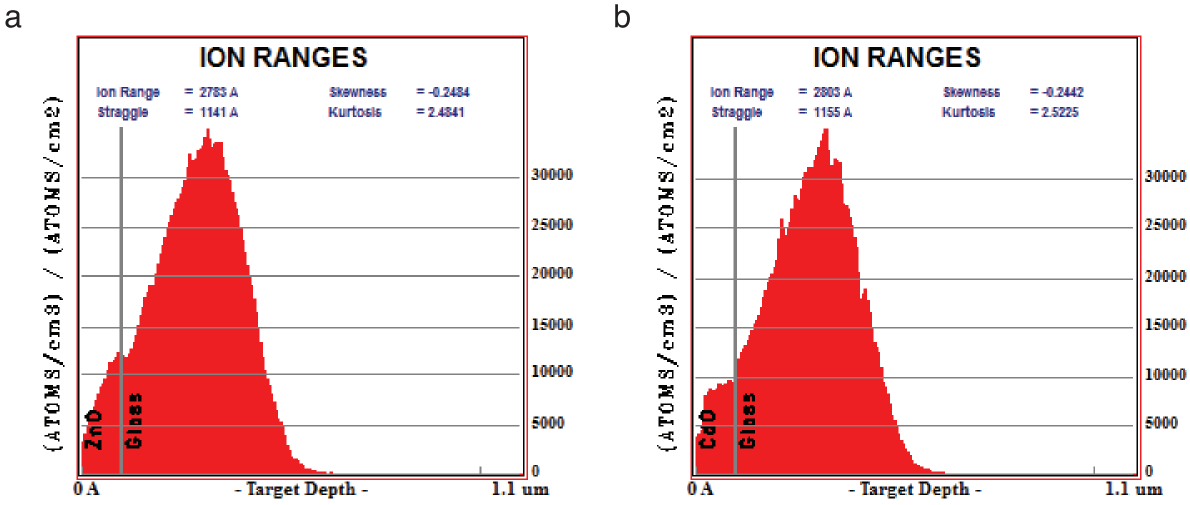

Figure A.9: Ion range calculations generated using SRIM for normal-incidence 120 keV Ne^+ ion irradiation into 100 nm (a) ZnO and (b) CdO thin films on glass substrates.

Appendix B

Mathematica code

The following sections include the code for Mathematica calculations used in this dissertation.

Direct-bandgap absorption fitting for carrier-filled bands

```
ClearAll["Global`*"]
<< PhysicalConstants`
plotSettingsDD =
  {ImageSize → Large,
   PlotStyle → {Red, Thickness[0.005], PointSize[0.01]},
   Frame → True, GridLines → Automatic,
   GridLinesStyle → Directive[LightGray],
   FrameStyle → Directive[Thick, 16],
   AxesStyle → Directive[Thin, 16],
   LabelStyle -> Directive[Bold, 16]};
SetOptions[Plot,
  BaseStyle → {FontFamily → "Helvetica", FontSize → 16}];
SetOptions[ListPlot,
  BaseStyle → {FontFamily → "Helvetica", FontSize → 16}];
SetOptions[ListLogPlot,
  BaseStyle → {FontFamily → "Helvetica", FontSize → 16}];
```

General

Constants

```
kbeV = 8.617 × 10^-5;(*Boltzmann constant,eV/K*)
T = 300;
(*Kelvin*)
```

Equations

```
                              0.5
abs[En_] := A * (En - Eg)        ;

                  Exp[-((En) / delt)²]
gauss[En_] :=  ─────────────────────── ;
                    delt * √Pi

                         (Eg + Ef) - En   -1
fermi[En_] := (1 + Exp[──────────────])
                            kbeV * T
```

Absorption Fitting

x = 1

α vs E data import

```
atable = Import["/Users/detert/Desktop/czox82.txt", "Table"];
```

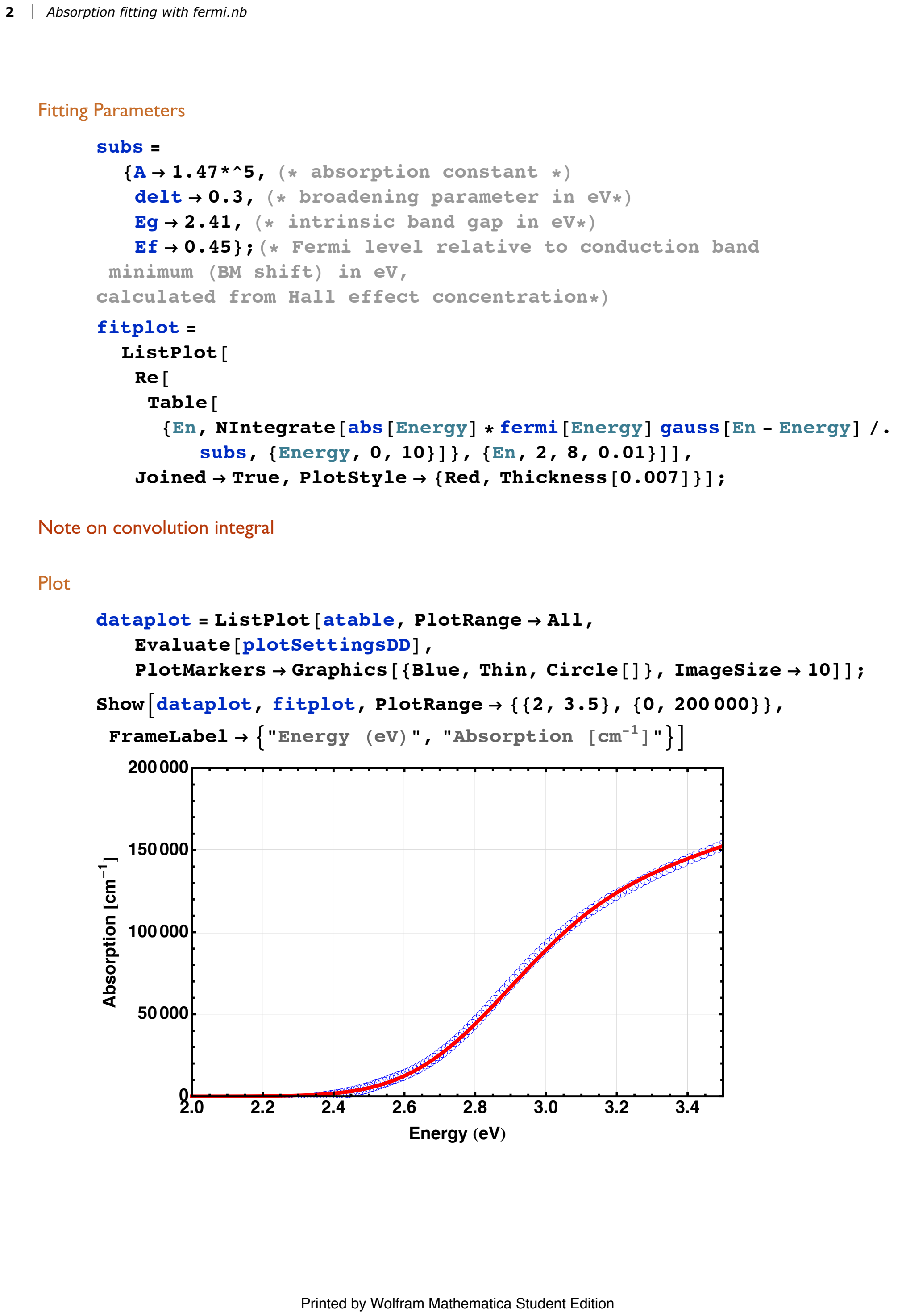

Fitting Parameters

```
subs =
  {A → 1.47*^5, (* absorption constant *)
   delt → 0.3, (* broadening parameter in eV*)
   Eg → 2.41, (* intrinsic band gap in eV*)
   Ef → 0.45};(* Fermi level relative to conduction band
 minimum (BM shift) in eV,
calculated from Hall effect concentration*)
fitplot =
  ListPlot[
   Re[
    Table[
     {En, NIntegrate[abs[Energy] * fermi[Energy] gauss[En - Energy] /.
        subs, {Energy, 0, 10}]}, {En, 2, 8, 0.01}]],
   Joined → True, PlotStyle → {Red, Thickness[0.007]}];
```

Note on convolution integral

Plot

```
dataplot = ListPlot[atable, PlotRange → All,
   Evaluate[plotSettingsDD],
   PlotMarkers → Graphics[{Blue, Thin, Circle[]}, ImageSize → 10]];
Show[dataplot, fitplot, PlotRange → {{2, 3.5}, {0, 200 000}},
 FrameLabel → {"Energy (eV)", "Absorption [cm^-1]"}]
```

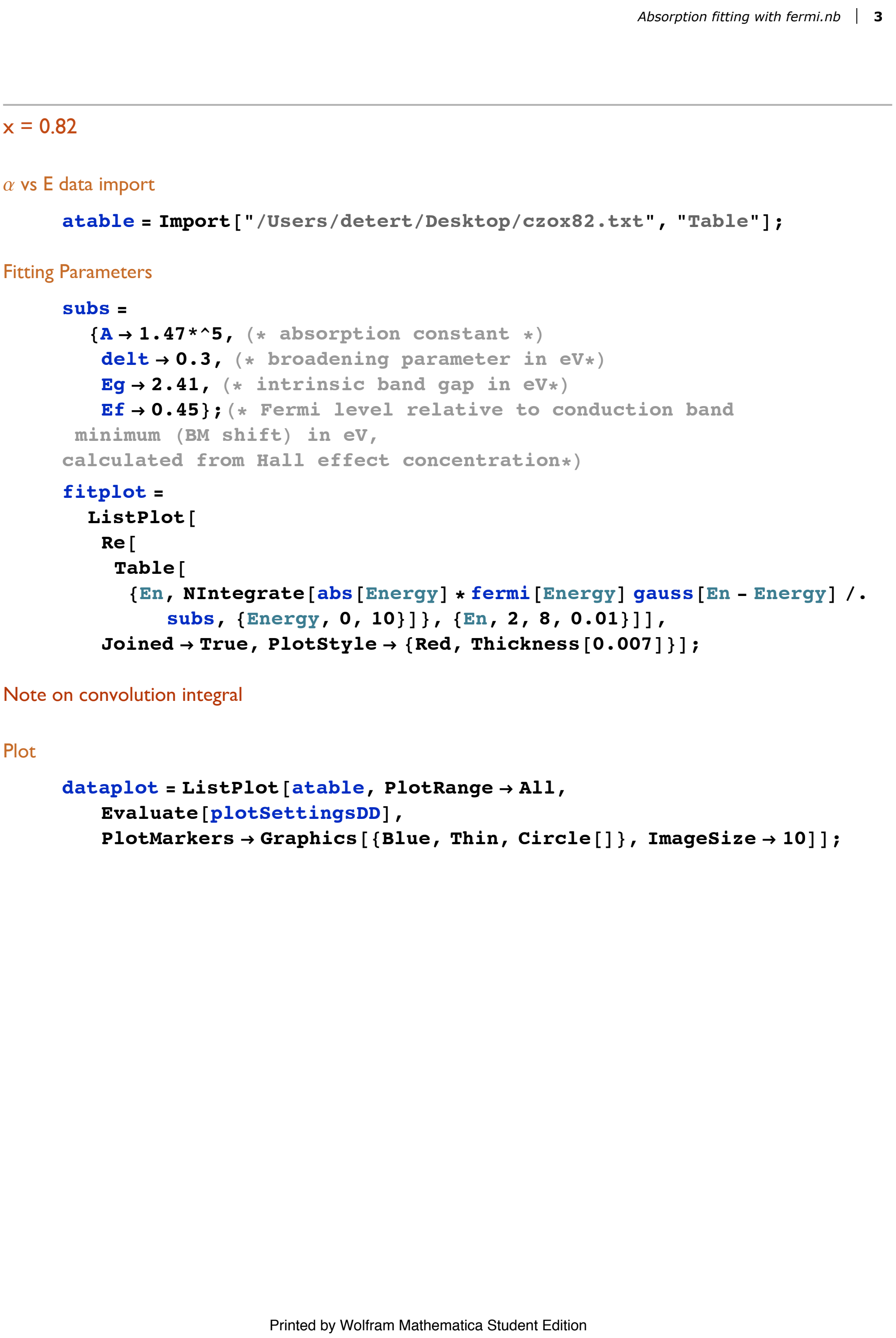

x = 0.82

α vs E data import

```
atable = Import["/Users/detert/Desktop/czox82.txt", "Table"];
```

Fitting Parameters

```
subs =
  {A → 1.47*^5, (* absorption constant *)
   delt → 0.3, (* broadening parameter in eV*)
   Eg → 2.41, (* intrinsic band gap in eV*)
   Ef → 0.45};(* Fermi level relative to conduction band
 minimum (BM shift) in eV,
calculated from Hall effect concentration*)
fitplot =
  ListPlot[
   Re[
    Table[
     {En, NIntegrate[abs[Energy] * fermi[Energy] gauss[En - Energy] /.
        subs, {Energy, 0, 10}]}, {En, 2, 8, 0.01}]],
   Joined → True, PlotStyle → {Red, Thickness[0.007]}];
```

Note on convolution integral

Plot

```
dataplot = ListPlot[atable, PlotRange → All,
   Evaluate[plotSettingsDD],
   PlotMarkers → Graphics[{Blue, Thin, Circle[]}, ImageSize → 10]];
```

```
Show[dataplot, fitplot, PlotRange → {{2, 3.5}, {0, 200 000}},
 FrameLabel → {"Energy (eV)", "Absorption [cm^-1]"}]
```

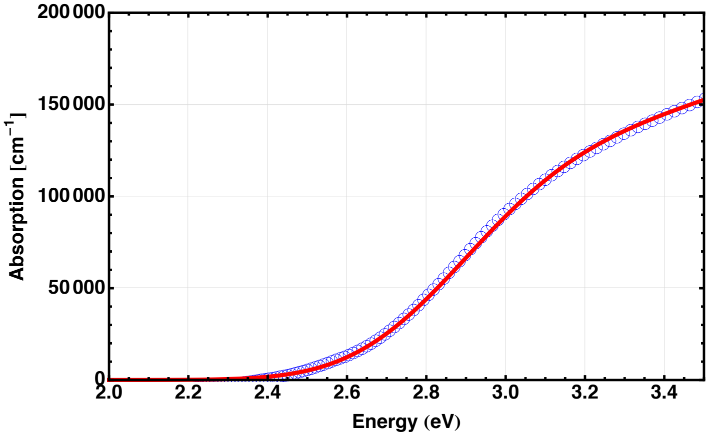

Fermi level calculation and bandgap renormalization calculations

Options

```
ClearAll["Global`*"]
<< PhysicalConstants`
plotSettingsMM =
  {ImageSize → Large,
   PlotStyle → {Red, Thickness[0.005], PointSize[0.015]},
   Frame → True, GridLines → Automatic,
   GridLinesStyle → Directive[LightGray],
   FrameStyle → Directive[Thick, 16],
   AxesStyle → Directive[Thin, 16],
   LabelStyle -> Directive[Bold, 16]};
SetOptions[Plot,
  BaseStyle → {FontFamily → "Helvetica", FontSize → 16}];
SetOptions[ListPlot,
  BaseStyle → {FontFamily → "Helvetica", FontSize → 16}];
SetOptions[ListLogPlot,
  BaseStyle → {FontFamily → "Helvetica", FontSize → 16}];
```

Constants

General

```
charge = 1.6 × 10^-19;
c = 2.997 × 10^8; (*cgs units*)
masse = 9.109 × 10^-28 (*g*);
chargeerg = 4.8 × 10^-10 (*charge on electron in ergs*);
eVerg = 1.602 × 10^-12; (*converts ev to erg.*)
hbar = 1.0546 × 10^-27 (* erg-s *);
kbeV = 8.617 × 10^-5;(*Boltzmann constant,eV/K*)
kb = 1.38 × 10^-16;(*Boltzmann constant,erg/K*)
T = 300;
(* K *)
```

Materials Parameters

```
e0CdO = 21.9;
e0ZnO = 9;
        e0CdO
abCdO = ───── 0.5 * 10^-8 (*bohr radius CdO, in cm*);
          mc
        e0ZnO
abZnO = ───── 0.5 * 10^-8 (*bohr radius CdO, in cm*);
          mc
```

Import a table of {x, Eg, n} values. The Eg - depdendent effective mass will be calculated from the value of Eg.

```
czotable =
  Transpose[
   Import[
    "/Users/detert/Dropbox/Research/TCO/CdZnO/Fermi
      calculations/Fermi calc data w eg.txt", "Table"]];
```

$$\texttt{k}[n\_] := \left(3 * \texttt{Pi}^2\, n\right)^{1/3}$$

$$\lambda[n\_] := 2\sqrt{\frac{\left(3 * \texttt{Pi}^2\, n\right)^{1/3}}{\texttt{Pi} * \texttt{ab}}}$$

$$\texttt{EErenorm}[k\_,\ \lambda\_] := \left(-\frac{2 * \texttt{chargeerg}^2 * k}{\texttt{Pi} * \epsilon 0} - \frac{\texttt{chargeerg}^2 * \lambda}{2 * \epsilon 0}\left(1 - \frac{4}{\texttt{Pi}}\texttt{ArcTan}\left[\frac{k}{\lambda}\right]\right)\right)\frac{1}{\texttt{eVerg}}$$

$$\texttt{IErenorm}[n\_] := \left(-\frac{\texttt{chargeerg} * \texttt{hbar}}{2}\sqrt{\frac{\left(\texttt{Pi}^3\, n\right)}{\epsilon 0 * \texttt{mc} * \texttt{masse}}}\right)\frac{1}{\texttt{eVerg}}$$

$$\texttt{vb}[k\_] := \frac{\texttt{hbar}^2 * k^2}{2\ (\texttt{masse})}\ \frac{1}{\texttt{eVerg}}$$

```
Etable = {};
(*Loop to adjust Ef guesses until nlow and nhigh converge
 to the electron concentration*)
For[dd = 1, dd ≤ Length[czotable[[1]]], dd++,
```

$$\left\{\texttt{n = czotable[[3, dd]], mc} = \frac{1}{1 + \frac{8.12571}{\texttt{czotable[[2,dd]]}}}\right\};$$

```
 If[czotable[[1, dd]] < 0.7, {ab = abZnO, ϵ0 = e0ZnO},
  {ab = abCdO, ϵ0 = e0CdO}];
 ee = EErenorm[k[n], λ[n]];
 ie = IErenorm[n];
 Evb = vb[k[n]];
 AppendTo[Etable, {ee, ie, Evb}]; (*total shift*)
 Print["x= ", czotable[[1, dd]], " e0: ", ϵ0 , " vb: ", Evb,
  " EErenorm: ", ee, " IErenorm: ", ie, " n: ", n];]
(*End loop to find Fermi energy from n*)
```

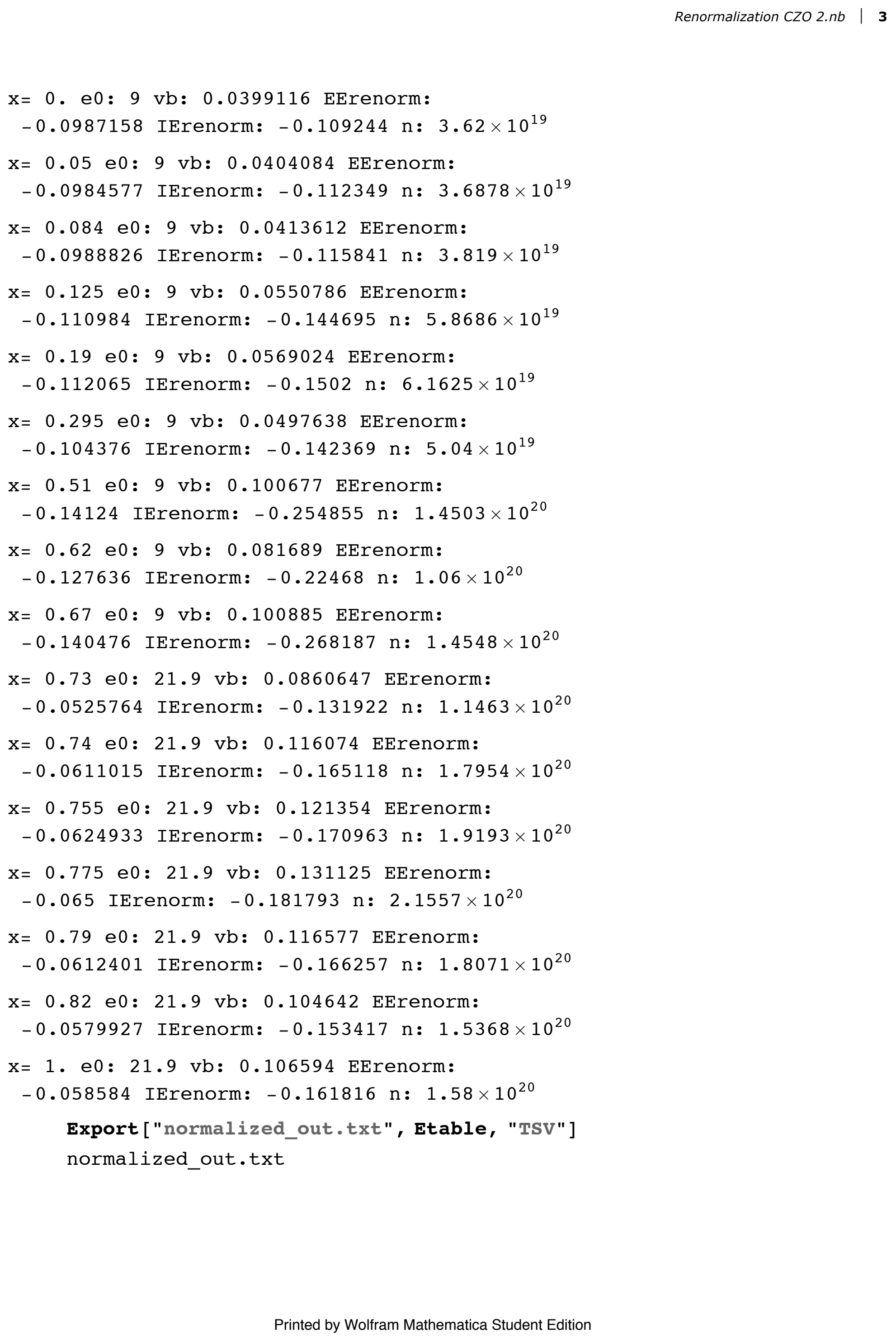

Renormalization CZO 2.nb | **3**

```
x= 0. e0: 9 vb: 0.0399116 EErenorm:
 -0.0987158 IErenorm: -0.109244 n: 3.62×10^19
x= 0.05 e0: 9 vb: 0.0404084 EErenorm:
 -0.0984577 IErenorm: -0.112349 n: 3.6878×10^19
x= 0.084 e0: 9 vb: 0.0413612 EErenorm:
 -0.0988826 IErenorm: -0.115841 n: 3.819×10^19
x= 0.125 e0: 9 vb: 0.0550786 EErenorm:
 -0.110984 IErenorm: -0.144695 n: 5.8686×10^19
x= 0.19 e0: 9 vb: 0.0569024 EErenorm:
 -0.112065 IErenorm: -0.1502 n: 6.1625×10^19
x= 0.295 e0: 9 vb: 0.0497638 EErenorm:
 -0.104376 IErenorm: -0.142369 n: 5.04×10^19
x= 0.51 e0: 9 vb: 0.100677 EErenorm:
 -0.14124 IErenorm: -0.254855 n: 1.4503×10^20
x= 0.62 e0: 9 vb: 0.081689 EErenorm:
 -0.127636 IErenorm: -0.22468 n: 1.06×10^20
x= 0.67 e0: 9 vb: 0.100885 EErenorm:
 -0.140476 IErenorm: -0.268187 n: 1.4548×10^20
x= 0.73 e0: 21.9 vb: 0.0860647 EErenorm:
 -0.0525764 IErenorm: -0.131922 n: 1.1463×10^20
x= 0.74 e0: 21.9 vb: 0.116074 EErenorm:
 -0.0611015 IErenorm: -0.165118 n: 1.7954×10^20
x= 0.755 e0: 21.9 vb: 0.121354 EErenorm:
 -0.0624933 IErenorm: -0.170963 n: 1.9193×10^20
x= 0.775 e0: 21.9 vb: 0.131125 EErenorm:
 -0.065 IErenorm: -0.181793 n: 2.1557×10^20
x= 0.79 e0: 21.9 vb: 0.116577 EErenorm:
 -0.0612401 IErenorm: -0.166257 n: 1.8071×10^20
x= 0.82 e0: 21.9 vb: 0.104642 EErenorm:
 -0.0579927 IErenorm: -0.153417 n: 1.5368×10^20
x= 1. e0: 21.9 vb: 0.106594 EErenorm:
 -0.058584 IErenorm: -0.161816 n: 1.58×10^20
```

```
     Export["normalized_out.txt", Etable, "TSV"]
     normalized_out.txt
```

Printed by Wolfram Mathematica Student Edition

Mobility calculations, Courtesy of Dr. Leon Hsu, University of Minnesota.

Calculate mobility for CdO at many different values of compensation. Can be fed into interpolating function to make a lookup function for calculating maximum mobility in doping/native defect concentrations where n, k are known.

```
ClearAll["Global`*"]


(*  Program to calculate temperature dependent mobilities *)
(*  in bulk CdCuO 11/29/10 --modified by DMD for Cd-rich CdZnO 7/2/13 *)
(*  Based on Szymanska and Dietl, J. Phys. Chem. Solids 39, 1025 (1978)  *)
(*  and Zawadzki and Szymanska, Phys. Stat. Sol. B 45, 415 (1971)  *)
(*  Takes non-parabolic shape of CB into account  *)

(*  12/15/04  version assuming n0 donors minimum, and then more donors
 and acceptors created in a fixed ratio (krad) by the irradiation  *)
(*  1/5/05 dielectric constant changed to 10.3  *)
(*  6/29/06  the lower limit in the final integrals is set to efermi/2000 *)
(*    because tpie oscillates wildly below that limit and gives *)
(*    unreasonable results  *)

(*  changeable parameters  *)
(* I looped this with a variable in the output filename such that one can let
   this run (many hours) and calculate points in steps of 0.01 in k. To calculate
   "1" change the iterator and loop limit to 9999 and make qq==.0001. k=
 1 will cause divide by 0 problems. Flatten output  - DMD 4/2014. *)
For[qq = 1, qq ≤ 1, qq++, kk = qq * 0.01;
 cstated = 1;  (* charge state of radiation generated donors  *)
 cstatea = 1;  (* charge state of radiation generated acceptors   *)

 (*  CdO parameters  *)
 epsinf = 5.3;  (*  high and low frequency dielectric constants  *)
 epsnot = 21.9;   (* could also be 10.7  *)
 egap = 2300 * 1.602 × 10^-15;   (*  bandgap of CdO in ergs (meV)  *)
 meff0 = 0.23;   (*  effective mass at band minimum  *)
elo = 55 * 1.602 × 10^-15;
 (*  longitudinal optical phonon energy in ergs (meV)  *)
 delta = 0 * 1.602 * 10^-15;  (*  spin orbit splitting for InN  *)
 e14 = 0.375 * 3 * 10^5;  (*  piezoelectric constant in esu/cm^2  (C/m^2)  *)

 defpot = 3.6 * 1.602 × 10^-12;   (* deformation potential in ergs (eV) *)
rho = 8.15;       (*  density in g/cm^3  *)
vlong = 5.9 × 10^5; (*  longitudinal acoustic phonon velocity in cm/s  *)
 vtrans = 2.9 × 10^5;  (*  transverse acoustic phonon velocity in cm/s  *)

 (*  constants  *)
(*  unless otherwise specified, all constants are in cgs units  *)
 kb = 1.38 * 10^-16;  (*  Boltzmann constant  *)
 hbar = 1.05458 * 10^-27;  (*   Planck's constant  *)
 m0 = 9.11 * 10^-28;    (*  bare electron mass  *)
e = 4.803 * 10^-10;   (*  electron charge  *)

 (*  define a lot of functions for later *)
```

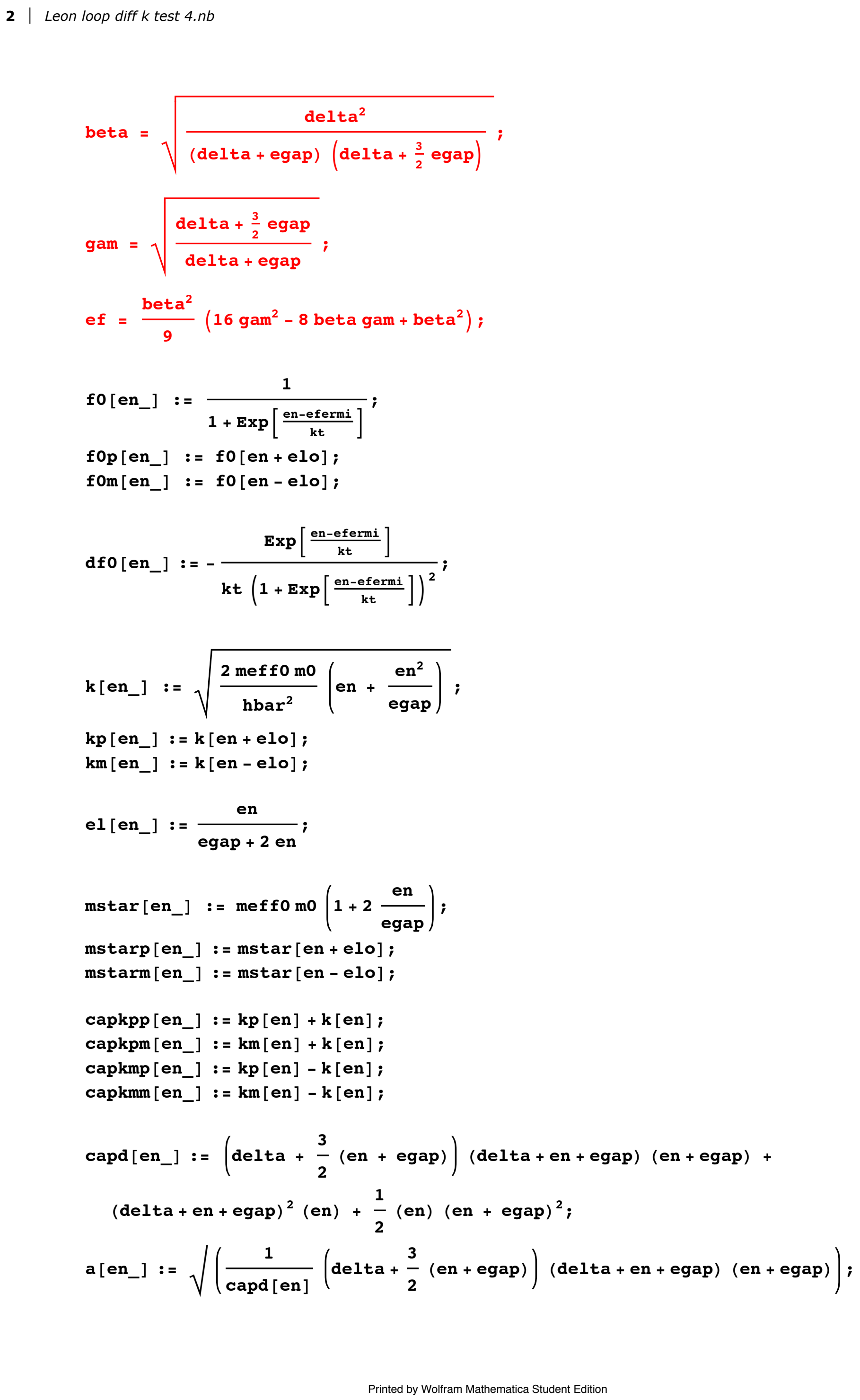

2 | *Leon loop diff k test 4.nb*

$$\mathtt{beta}\ =\ \sqrt{\frac{\mathtt{delta}^2}{(\mathtt{delta}+\mathtt{egap})\left(\mathtt{delta}+\frac{3}{2}\,\mathtt{egap}\right)}}\ ;$$

$$\mathtt{gam}\ =\ \sqrt{\frac{\mathtt{delta}+\frac{3}{2}\,\mathtt{egap}}{\mathtt{delta}+\mathtt{egap}}}\ ;$$

$$\mathtt{ef}\ =\ \frac{\mathtt{beta}^2}{9}\left(16\ \mathtt{gam}^2-8\ \mathtt{beta}\ \mathtt{gam}+\mathtt{beta}^2\right);$$

$$\mathtt{f0[en\_]}\ :=\ \frac{1}{1+\mathtt{Exp}\left[\frac{\mathtt{en-efermi}}{\mathtt{kt}}\right]};$$

$$\mathtt{f0p[en\_]}\ :=\ \mathtt{f0[en+elo]};$$
$$\mathtt{f0m[en\_]}\ :=\ \mathtt{f0[en-elo]};$$

$$\mathtt{df0[en\_]}\ :=-\frac{\mathtt{Exp}\left[\frac{\mathtt{en-efermi}}{\mathtt{kt}}\right]}{\mathtt{kt}\left(1+\mathtt{Exp}\left[\frac{\mathtt{en-efermi}}{\mathtt{kt}}\right]\right)^2};$$

$$\mathtt{k[en\_]}\ :=\ \sqrt{\frac{2\ \mathtt{meff0}\ \mathtt{m0}}{\mathtt{hbar}^2}\left(\mathtt{en}\ +\ \frac{\mathtt{en}^2}{\mathtt{egap}}\right)}\ ;$$

$$\mathtt{kp[en\_]}\ :=\mathtt{k[en+elo]};$$
$$\mathtt{km[en\_]}\ :=\mathtt{k[en-elo]};$$

$$\mathtt{el[en\_]}\ :=\ \frac{\mathtt{en}}{\mathtt{egap}+2\ \mathtt{en}};$$

$$\mathtt{mstar[en\_]}\ :=\ \mathtt{meff0}\ \mathtt{m0}\left(1+2\ \frac{\mathtt{en}}{\mathtt{egap}}\right);$$

$$\mathtt{mstarp[en\_]}\ :=\mathtt{mstar[en+elo]};$$
$$\mathtt{mstarm[en\_]}\ :=\mathtt{mstar[en-elo]};$$

$$\mathtt{capkpp[en\_]}\ :=\mathtt{kp[en]}+\mathtt{k[en]};$$
$$\mathtt{capkpm[en\_]}\ :=\mathtt{km[en]}+\mathtt{k[en]};$$
$$\mathtt{capkmp[en\_]}\ :=\mathtt{kp[en]}-\mathtt{k[en]};$$
$$\mathtt{capkmm[en\_]}\ :=\mathtt{km[en]}-\mathtt{k[en]};$$

$$\mathtt{capd[en\_]}\ :=\ \left(\mathtt{delta}\ +\ \frac{3}{2}\ (\mathtt{en}\ +\ \mathtt{egap})\right)\ (\mathtt{delta}+\mathtt{en}+\mathtt{egap})\ (\mathtt{en}+\mathtt{egap})\ +\ (\mathtt{delta}+\mathtt{en}+\mathtt{egap})^2\ (\mathtt{en})\ +\ \frac{1}{2}\ (\mathtt{en})\ (\mathtt{en}\ +\ \mathtt{egap})^2;$$

$$\mathtt{a[en\_]}\ :=\ \sqrt{\left(\frac{1}{\mathtt{capd[en]}}\left(\mathtt{delta}+\frac{3}{2}\ (\mathtt{en}+\mathtt{egap})\right)\ (\mathtt{delta}+\mathtt{en}+\mathtt{egap})\ (\mathtt{en}+\mathtt{egap})\right)};$$

Printed by Wolfram Mathematica Student Edition

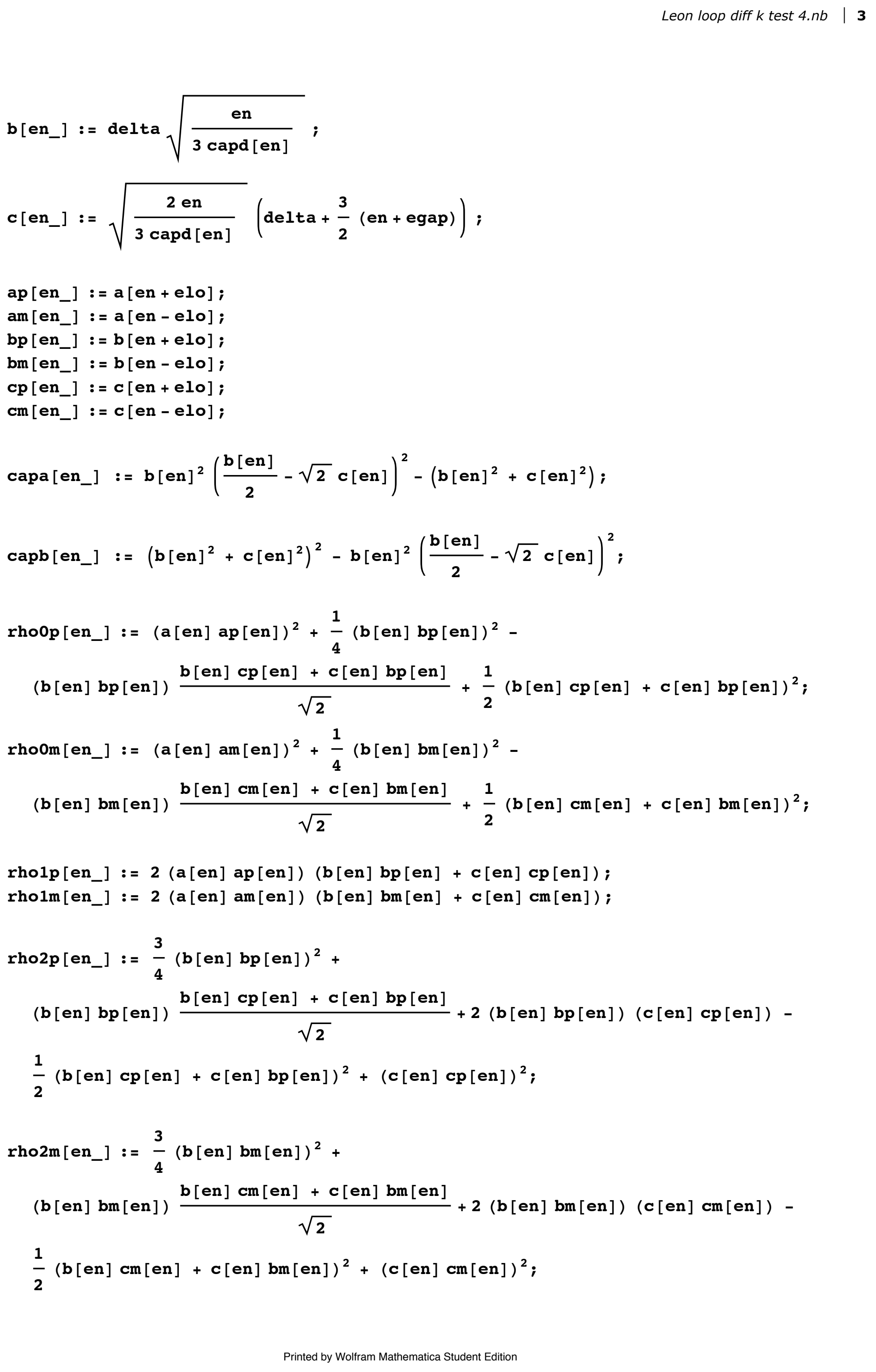

```
b[en_] := delta √(en/(3 capd[en])) ;

c[en_] := √((2 en)/(3 capd[en])) (delta + 3/2 (en + egap)) ;

ap[en_] := a[en + elo];
am[en_] := a[en - elo];
bp[en_] := b[en + elo];
bm[en_] := b[en - elo];
cp[en_] := c[en + elo];
cm[en_] := c[en - elo];

capa[en_] := b[en]^2 (b[en]/2 - √2 c[en])^2 - (b[en]^2 + c[en]^2);

capb[en_] := (b[en]^2 + c[en]^2)^2 - b[en]^2 (b[en]/2 - √2 c[en])^2;

rho0p[en_] := (a[en] ap[en])^2 + 1/4 (b[en] bp[en])^2 -
  (b[en] bp[en]) (b[en] cp[en] + c[en] bp[en])/√2 + 1/2 (b[en] cp[en] + c[en] bp[en])^2;
rho0m[en_] := (a[en] am[en])^2 + 1/4 (b[en] bm[en])^2 -
  (b[en] bm[en]) (b[en] cm[en] + c[en] bm[en])/√2 + 1/2 (b[en] cm[en] + c[en] bm[en])^2;

rho1p[en_] := 2 (a[en] ap[en]) (b[en] bp[en] + c[en] cp[en]);
rho1m[en_] := 2 (a[en] am[en]) (b[en] bm[en] + c[en] cm[en]);

rho2p[en_] := 3/4 (b[en] bp[en])^2 +
  (b[en] bp[en]) (b[en] cp[en] + c[en] bp[en])/√2 + 2 (b[en] bp[en]) (c[en] cp[en]) -
  1/2 (b[en] cp[en] + c[en] bp[en])^2 + (c[en] cp[en])^2;

rho2m[en_] := 3/4 (b[en] bm[en])^2 +
  (b[en] bm[en]) (b[en] cm[en] + c[en] bm[en])/√2 + 2 (b[en] bm[en]) (c[en] cm[en]) -
  1/2 (b[en] cm[en] + c[en] bm[en])^2 + (c[en] cm[en])^2;
```

```
               1
nq := ─────────────────;
      Exp[elo / kt] - 1

(*  Set up a loop for each individual scattering mechanism  *)
For[mech = 1, mech ≤ 1, mech++,
 If[mech == 1,
  opcon = 1;
  accon = 1;
  coulcon = 1;
  picon = 1;
  srcon = 0;
  discon  = 0;
  diskette = OpenWrite["cdo_totk" <> IntegerString[qq, 10, 4] <> ".txt"];
  SetOptions[diskette, FormatType → StandardForm];
 ];
 If[mech == 3,
  opcon = 1;
  accon = 0;
  coulcon = 0;
  picon = 0;
  srcon = 0;
  discon  = 0;
  diskette = OpenWrite["cdo_op.dat"];
  SetOptions[diskette, FormatType → CForm];
 ];
 If[mech == 2,
  opcon = 0;
  accon = 0;
  coulcon = 1;
  picon = 0;
  srcon = 0;
  discon  = 0;
  diskette = OpenWrite["cdo_coul.dat"];
  SetOptions[diskette, FormatType → CForm];
 ];
 If[mech == 4,
  opcon = 0;
  accon = 1;
  coulcon = 0;
  picon = 1;
  srcon = 0;
  discon  = 0;
  diskette = OpenWrite["cdo_ac.dat"];
  SetOptions[diskette, FormatType → CForm];
 ];
 If[mech == 5,
  opcon = 0;
  accon = 0;
  coulcon = 0;
  picon = 1;
  srcon = 0;
```

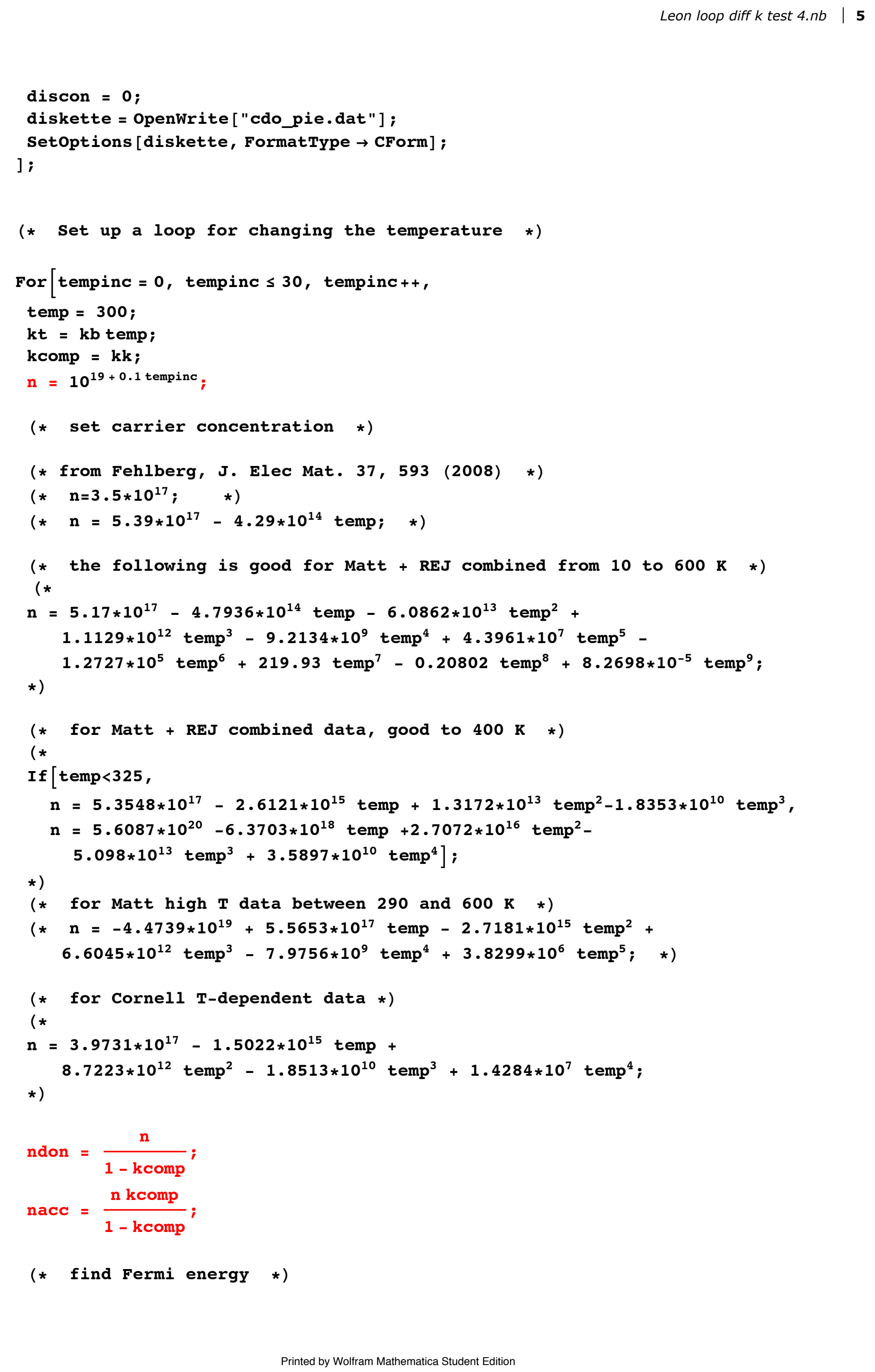

Leon loop diff k test 4.nb | 5

```
 discon = 0;
 diskette = OpenWrite["cdo_pie.dat"];
 SetOptions[diskette, FormatType → CForm];
];


(*  Set up a loop for changing the temperature  *)

For[tempinc = 0, tempinc ≤ 30, tempinc++,
 temp = 300;
 kt  = kb temp;
 kcomp = kk;
 n = 10^(19 + 0.1 tempinc);

 (*  set carrier concentration  *)

 (* from Fehlberg, J. Elec Mat. 37, 593 (2008)  *)
 (*  n=3.5*10^17;    *)
 (*  n = 5.39*10^17 - 4.29*10^14 temp;  *)

 (*  the following is good for Matt + REJ combined from 10 to 600 K  *)
  (*
 n = 5.17*10^17 - 4.7936*10^14 temp - 6.0862*10^13 temp^2 +
    1.1129*10^12 temp^3 - 9.2134*10^9 temp^4 + 4.3961*10^7 temp^5 -
    1.2727*10^5 temp^6 + 219.93 temp^7 - 0.20802 temp^8 + 8.2698*10^-5 temp^9;
 *)

 (*  for Matt + REJ combined data, good to 400 K  *)
 (*
 If[temp<325,
   n = 5.3548*10^17 - 2.6121*10^15 temp + 1.3172*10^13 temp^2-1.8353*10^10 temp^3,
   n = 5.6087*10^20 -6.3703*10^18 temp +2.7072*10^16 temp^2-
     5.098*10^13 temp^3 + 3.5897*10^10 temp^4];
 *)
 (*  for Matt high T data between 290 and 600 K  *)
 (*  n = -4.4739*10^19 + 5.5653*10^17 temp - 2.7181*10^15 temp^2 +
    6.6045*10^12 temp^3 - 7.9756*10^9 temp^4 + 3.8299*10^6 temp^5;  *)

 (*  for Cornell T-dependent data *)
 (*
 n = 3.9731*10^17 - 1.5022*10^15 temp +
    8.7223*10^12 temp^2 - 1.8513*10^10 temp^3 + 1.4284*10^7 temp^4;
 *)

 ndon = n / (1 - kcomp);

 nacc = n kcomp / (1 - kcomp);

 (*  find Fermi energy  *)
```

Printed by Wolfram Mathematica Student Edition

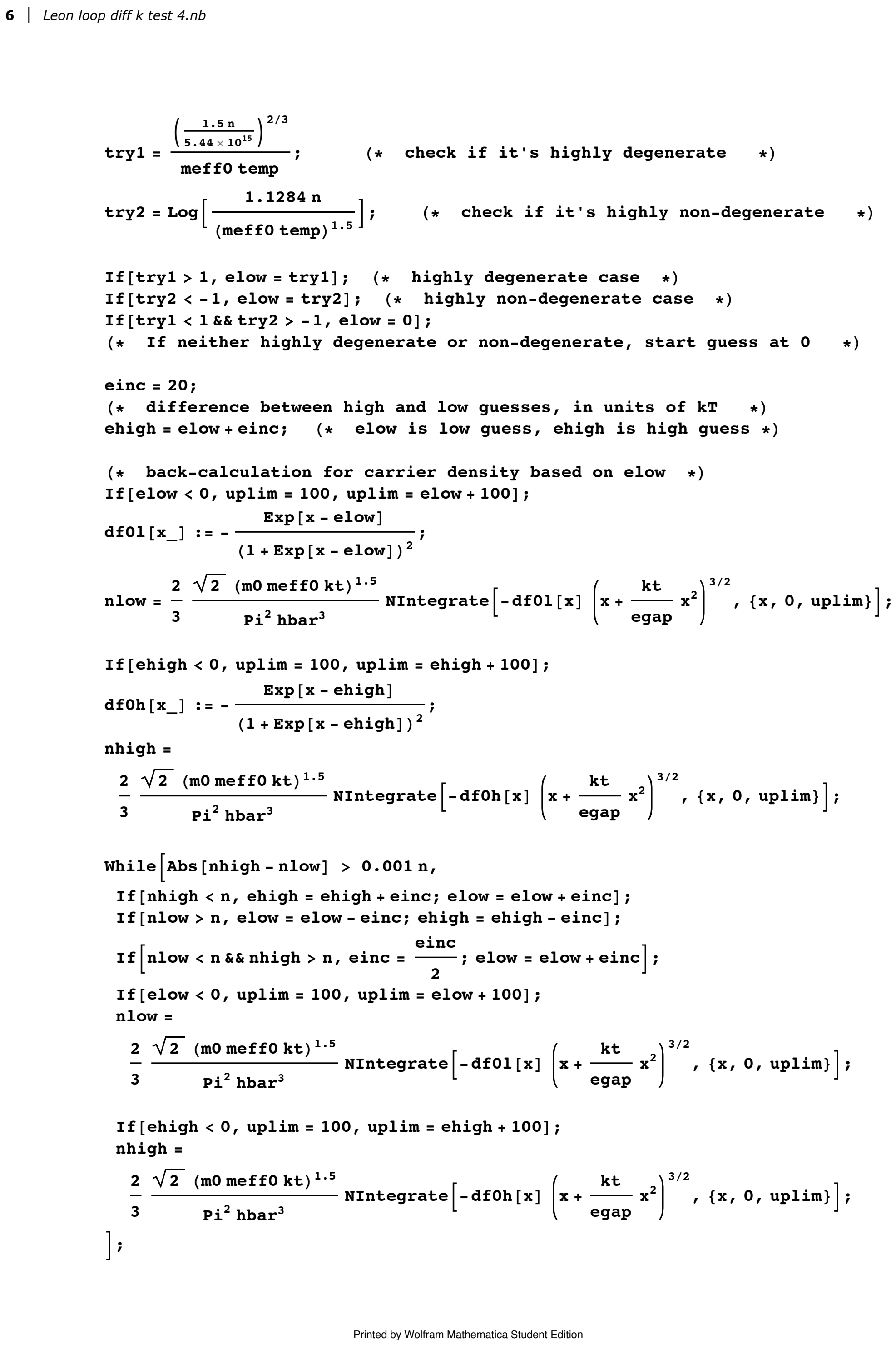

6 | *Leon loop diff k test 4.nb*

```
try1 = (1.5 n/(5.44 × 10^15))^(2/3)/(meff0 temp);      (*  check if it's highly degenerate   *)

try2 = Log[1.1284 n/(meff0 temp)^1.5];     (*  check if it's highly non-degenerate   *)

If[try1 > 1, elow = try1];  (*  highly degenerate case  *)
If[try2 < -1, elow = try2];  (*  highly non-degenerate case  *)
If[try1 < 1 && try2 > -1, elow = 0];
(*  If neither highly degenerate or non-degenerate, start guess at 0   *)

einc = 20;
(*  difference between high and low guesses, in units of kT   *)
ehigh = elow + einc;  (*  elow is low guess, ehigh is high guess *)

(*  back-calculation for carrier density based on elow  *)
If[elow < 0, uplim = 100, uplim = elow + 100];
df0l[x_] := -Exp[x - elow]/(1 + Exp[x - elow])^2;
nlow = 2/3 (√2 (m0 meff0 kt)^1.5)/(Pi^2 hbar^3) NIntegrate[-df0l[x] (x + kt/egap x^2)^(3/2), {x, 0, uplim}];

If[ehigh < 0, uplim = 100, uplim = ehigh + 100];
df0h[x_] := -Exp[x - ehigh]/(1 + Exp[x - ehigh])^2;
nhigh =
  2/3 (√2 (m0 meff0 kt)^1.5)/(Pi^2 hbar^3) NIntegrate[-df0h[x] (x + kt/egap x^2)^(3/2), {x, 0, uplim}];

While[Abs[nhigh - nlow] > 0.001 n,
 If[nhigh < n, ehigh = ehigh + einc; elow = elow + einc];
 If[nlow > n, elow = elow - einc; ehigh = ehigh - einc];
 If[nlow < n && nhigh > n, einc = einc/2; elow = elow + einc];
 If[elow < 0, uplim = 100, uplim = elow + 100];
 nlow =
   2/3 (√2 (m0 meff0 kt)^1.5)/(Pi^2 hbar^3) NIntegrate[-df0l[x] (x + kt/egap x^2)^(3/2), {x, 0, uplim}];

 If[ehigh < 0, uplim = 100, uplim = ehigh + 100];
 nhigh =
   2/3 (√2 (m0 meff0 kt)^1.5)/(Pi^2 hbar^3) NIntegrate[-df0h[x] (x + kt/egap x^2)^(3/2), {x, 0, uplim}];
];
```

Printed by Wolfram Mathematica Student Edition

Leon loop diff k test 4.nb | **7**

```
eta = (elow + ehigh)/2;
efermi = eta kt;

If[eta < 0, uplim = 100, uplim = eta + 100];

(*  calculate thomas fermi momentum (used in screening)  *)
ketf = Sqrt[((4 e^2)/(Pi hbar^2) NIntegrate[-df0[en] mstar[en] k[en], {en, 0, uplim kt}])];

If[efermi ≥ 0, phi[en_] := (en - efermi)/kt;, phi[en_] := en/kt;];
phip[en_] := phi[en + elo];
phim[en_] := phi[en - elo];


(*  find scattering time due to Coulomb interaction  *)

(*  figure out # of donors and acceptors from radiation damage  *)


lamcoul = Sqrt[epsnot]/ketf;
ksi[en_] := 4 k[e n]^2 lamcoul^2;
fimp[en_] := Log[ksi[en] + 1] - ksi[en]/(ksi[en] + 1) +
   4 capa[en] (1 + 1/(ksi[en] + 1) - 2/ksi[en] Log[ksi[en] + 1]) +
   2 capb[en] (1 - 4/ksi[en] + 6/ksi[en]^2 Log[ksi[en] + 1] - 2/(ksi[en] (ksi[en] + 1)));

tcoul[en_] := (1/(2 Pi) (epsnot^2 hbar^3)/(mstar[en] e^4) 1/fimp[en] k[en]^3) 1/(ndon cstated^2 + nacc cstatea^2);

(*  find scattering time due to deformation potential acoustic phonons *)

phi1 = (8 gam^2 - beta^2)/7;
phi2 = (4 gam^2 + beta^2)/5;
phi3 = (3 beta^4 + 32 beta^2 gam^2 + 16 gam^4)/51;
faclong[en_] := (1 - el[en] (1 + 7/18 29/40 phi1 + 5/18 3/40 phi2))^2;
```

Printed by Wolfram Mathematica Student Edition

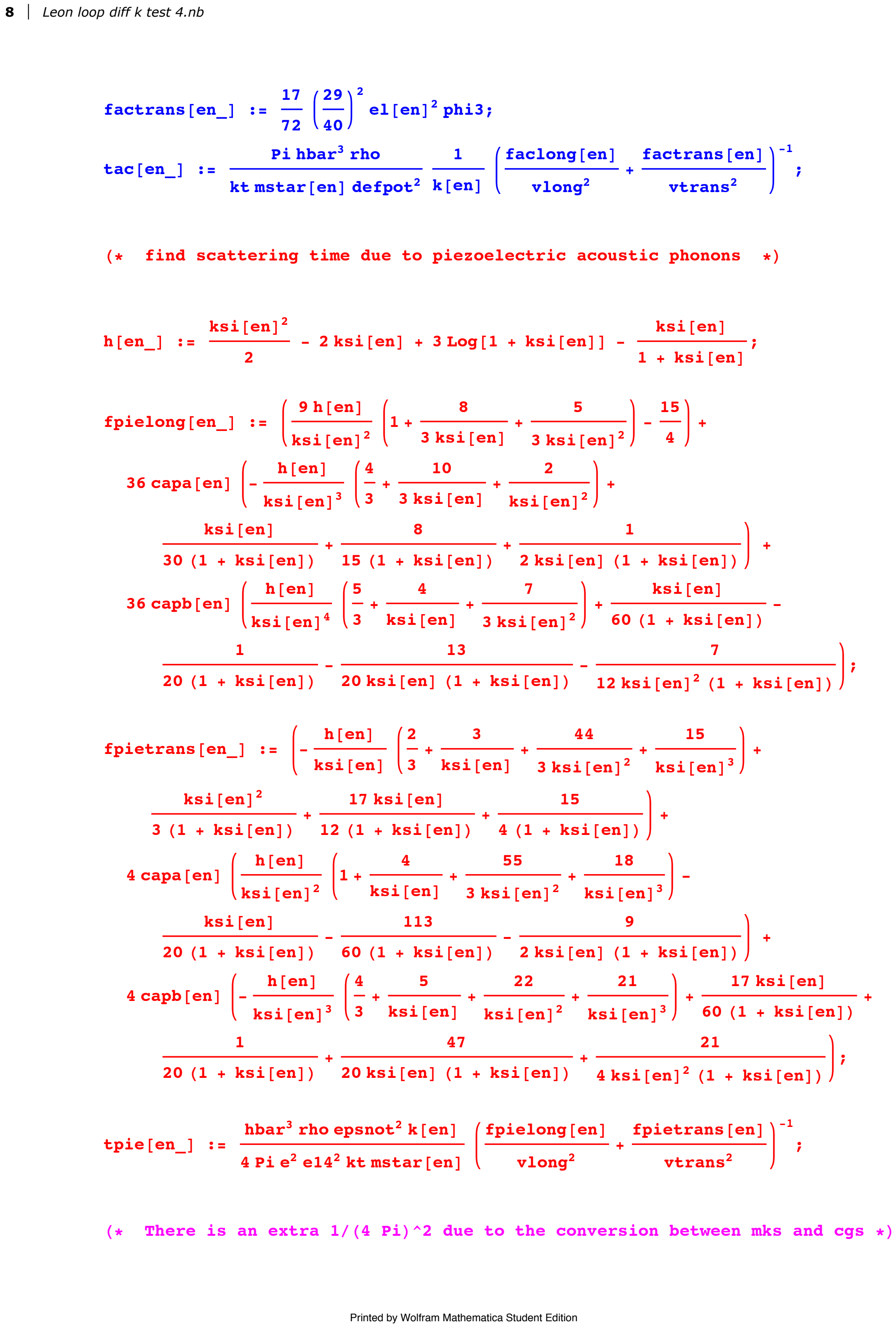

8 | *Leon loop diff k test 4.nb*

$$\mathtt{factrans[en\_]} := \frac{17}{72}\left(\frac{29}{40}\right)^{2} \mathtt{el[en]}^{2}\,\mathtt{phi3};$$

$$\mathtt{tac[en\_]} := \frac{\mathtt{Pi}\,\mathtt{hbar}^{3}\,\mathtt{rho}}{\mathtt{kt}\,\mathtt{mstar[en]}\,\mathtt{defpot}^{2}}\,\frac{1}{\mathtt{k[en]}}\left(\frac{\mathtt{faclong[en]}}{\mathtt{vlong}^{2}}+\frac{\mathtt{factrans[en]}}{\mathtt{vtrans}^{2}}\right)^{-1};$$

`(*  find scattering time due to piezoelectric acoustic phonons  *)`

$$\mathtt{h[en\_]} := \frac{\mathtt{ksi[en]}^{2}}{2} - 2\,\mathtt{ksi[en]} + 3\,\mathtt{Log[1 + ksi[en]]} - \frac{\mathtt{ksi[en]}}{1+\mathtt{ksi[en]}};$$

$$\begin{aligned}\mathtt{fpielong[en\_]} := {} & \Bigg(\frac{9\,\mathtt{h[en]}}{\mathtt{ksi[en]}^{2}}\Bigg(1+\frac{8}{3\,\mathtt{ksi[en]}}+\frac{5}{3\,\mathtt{ksi[en]}^{2}}\Bigg)-\frac{15}{4}\Bigg) + \\ & 36\,\mathtt{capa[en]}\Bigg(-\frac{\mathtt{h[en]}}{\mathtt{ksi[en]}^{3}}\Bigg(\frac{4}{3}+\frac{10}{3\,\mathtt{ksi[en]}}+\frac{2}{\mathtt{ksi[en]}^{2}}\Bigg) + \\ & \quad \frac{\mathtt{ksi[en]}}{30\,(1+\mathtt{ksi[en]})}+\frac{8}{15\,(1+\mathtt{ksi[en]})}+\frac{1}{2\,\mathtt{ksi[en]}\,(1+\mathtt{ksi[en]})}\Bigg) + \\ & 36\,\mathtt{capb[en]}\Bigg(\frac{\mathtt{h[en]}}{\mathtt{ksi[en]}^{4}}\Bigg(\frac{5}{3}+\frac{4}{\mathtt{ksi[en]}}+\frac{7}{3\,\mathtt{ksi[en]}^{2}}\Bigg)+\frac{\mathtt{ksi[en]}}{60\,(1+\mathtt{ksi[en]})} - \\ & \quad \frac{1}{20\,(1+\mathtt{ksi[en]})}-\frac{13}{20\,\mathtt{ksi[en]}\,(1+\mathtt{ksi[en]})}-\frac{7}{12\,\mathtt{ksi[en]}^{2}\,(1+\mathtt{ksi[en]})}\Bigg);\end{aligned}$$

$$\begin{aligned}\mathtt{fpietrans[en\_]} := {} & \Bigg(-\frac{\mathtt{h[en]}}{\mathtt{ksi[en]}}\Bigg(\frac{2}{3}+\frac{3}{\mathtt{ksi[en]}}+\frac{44}{3\,\mathtt{ksi[en]}^{2}}+\frac{15}{\mathtt{ksi[en]}^{3}}\Bigg) + \\ & \quad \frac{\mathtt{ksi[en]}^{2}}{3\,(1+\mathtt{ksi[en]})}+\frac{17\,\mathtt{ksi[en]}}{12\,(1+\mathtt{ksi[en]})}+\frac{15}{4\,(1+\mathtt{ksi[en]})}\Bigg) + \\ & 4\,\mathtt{capa[en]}\Bigg(\frac{\mathtt{h[en]}}{\mathtt{ksi[en]}^{2}}\Bigg(1+\frac{4}{\mathtt{ksi[en]}}+\frac{55}{3\,\mathtt{ksi[en]}^{2}}+\frac{18}{\mathtt{ksi[en]}^{3}}\Bigg) - \\ & \quad \frac{\mathtt{ksi[en]}}{20\,(1+\mathtt{ksi[en]})}-\frac{113}{60\,(1+\mathtt{ksi[en]})}-\frac{9}{2\,\mathtt{ksi[en]}\,(1+\mathtt{ksi[en]})}\Bigg) + \\ & 4\,\mathtt{capb[en]}\Bigg(-\frac{\mathtt{h[en]}}{\mathtt{ksi[en]}^{3}}\Bigg(\frac{4}{3}+\frac{5}{\mathtt{ksi[en]}}+\frac{22}{\mathtt{ksi[en]}^{2}}+\frac{21}{\mathtt{ksi[en]}^{3}}\Bigg)+\frac{17\,\mathtt{ksi[en]}}{60\,(1+\mathtt{ksi[en]})} + \\ & \quad \frac{1}{20\,(1+\mathtt{ksi[en]})}+\frac{47}{20\,\mathtt{ksi[en]}\,(1+\mathtt{ksi[en]})}+\frac{21}{4\,\mathtt{ksi[en]}^{2}\,(1+\mathtt{ksi[en]})}\Bigg);\end{aligned}$$

$$\mathtt{tpie[en\_]} := \frac{\mathtt{hbar}^{3}\,\mathtt{rho}\,\mathtt{epsnot}^{2}\,\mathtt{k[en]}}{4\,\mathtt{Pi}\,\mathtt{e}^{2}\,\mathtt{e14}^{2}\,\mathtt{kt}\,\mathtt{mstar[en]}}\left(\frac{\mathtt{fpielong[en]}}{\mathtt{vlong}^{2}}+\frac{\mathtt{fpietrans[en]}}{\mathtt{vtrans}^{2}}\right)^{-1};$$

`(*  There is an extra 1/(4 Pi)^2 due to the conversion between mks and cgs *)`

Printed by Wolfram Mathematica Student Edition

```
(*  calculate optical phonon contribution to scattering  *)

(*  screening length for optical phonons  *)
```

$$\text{lamb} = \frac{\sqrt{\text{epsinf}}}{\text{ketf}};$$

```
(*  Calculate dij matrix elements  *)
(*  iloop and jloop variables run 1 to 3, but i and j run 0 to 2  *)
For[iloop = 1, iloop ≤ 3, iloop++,
 i = iloop - 1;
 For[jloop = 1, jloop ≤ iloop, jloop++,
  j = jloop - 1;
```

$$\text{capvp[en\_]} = \frac{1}{2}\left(\text{phi[en]}^{j} - \frac{\text{kp[en]}^{2} + \text{k[en]}^{2}}{2\ \text{k[en]}^{2}}\ \text{phip[en]}^{j}\right)$$

$$\left(\text{rho0p[en]} + \text{rho1p[en]}\ \frac{\text{kp[en]}^{2} + \text{k[en]}^{2}}{2\ \text{k[en]}\ \text{kp[en]}} + \text{rho2p[en]}\ \left(\frac{\text{kp[en]}^{2} + \text{k[en]}^{2}}{2\ \text{k[en]}\ \text{kp[en]}}\right)^{2}\right)$$

$$\left(\text{Log}\left[\frac{1 + \text{lamb}^{2}\ \text{capkpp[en]}^{2}}{1 + \text{lamb}^{2}\ \text{capkmp[en]}^{2}}\right] - \frac{4\ \text{lamb}^{2}\ \text{kp[en]}\ \text{k[en]}}{\left(1 + \text{lamb}^{2}\ \text{capkpp[en]}^{2}\right)\ \left(1 + \text{lamb}^{2}\ \text{capkmp[en]}^{2}\right)}\right) +$$

$$\Biggl(-\left(\text{phi[en]}^{j} - \frac{\text{kp[en]}^{2} + \text{k[en]}^{2}}{2\ \text{k[en]}^{2}}\ \text{phip[en]}^{j}\right)\ \Biggl(\text{rho1p[en]}\ \frac{1}{4\ \text{lamb}^{2}\ \text{kp[en]}\ \text{k[en]}} +$$

$$\text{rho2p[en]}\ \frac{\text{kp[en]}^{2} + \text{k[en]}^{2}}{4\ \text{lamb}^{2}\ \text{kp[en]}^{2}\ \text{k[en]}^{2}}\Biggr) + \text{phip[en]}^{j}\ \frac{1}{4\ \text{lamb}^{2}\ \text{k[en]}^{2}}$$

$$\Biggl(\text{rho0p[en]} + \text{rho1p[en]}\ \frac{\text{kp[en]}^{2} + \text{k[en]}^{2}}{2\ \text{k[en]}\ \text{kp[en]}} + \text{rho2p[en]}\ \left(\frac{\text{kp[en]}^{2} + \text{k[en]}^{2}}{2\ \text{k[en]}\ \text{kp[en]}}\right)^{2}\Biggr)\Biggr)$$

$$\Biggl(4\ \text{lamb}^{2}\ \text{kp[en]}\ \text{k[en]} - 2\ \text{Log}\left[\frac{1 + \text{lamb}^{2}\ \text{capkpp[en]}^{2}}{1 + \text{lamb}^{2}\ \text{capkmp[en]}^{2}}\right] +$$

$$\frac{4\ \text{lamb}^{2}\ \text{kp[en]}\ \text{k[en]}}{\left(1 + \text{lamb}^{2}\ \text{capkpp[en]}^{2}\right)\ \left(1 + \text{lamb}^{2}\ \text{capkmp[en]}^{2}\right)}\Biggr) + \Biggl(\text{rho2p[en]}$$

$$\frac{1}{8\ \text{lamb}^{4}\ \text{kp[en]}^{2}\ \text{k[en]}^{2}}\ \left(\text{phi[en]}^{j} - \frac{\text{kp[en]}^{2} + \text{k[en]}^{2}}{2\ \text{k[en]}^{2}}\ \text{phip[en]}^{j}\right) - \text{phip[en]}^{j}$$

$$\left(\text{rho1p[en]}\ \frac{1}{8\ \text{lamb}^{4}\ \text{kp[en]}\ \text{k[en]}^{3}} + \text{rho2p[en]}\ \frac{\text{kp[en]}^{2} + \text{k[en]}^{2}}{8\ \text{lamb}^{4}\ \text{kp[en]}^{2}\ \text{k[en]}^{4}}\right)\Biggr)$$

$$\Biggl(4\ \text{lamb}^{4}\ \text{k[en]}\ \text{kp[en]}\ \left(\text{kp[en]}^{2} + \text{k[en]}^{2}\right) - 8\ \text{lamb}^{2}\ \text{k[en]}\ \text{kp[en]} + 3\ \text{Log}\Biggl[$$

$$\frac{1 + \text{lamb}^{2}\ \text{capkpp[en]}^{2}}{1 + \text{lamb}^{2}\ \text{capkmp[en]}^{2}}\Biggr] - \frac{4\ \text{lamb}^{2}\ \text{kp[en]}\ \text{k[en]}}{\left(1 + \text{lamb}^{2}\ \text{capkpp[en]}^{2}\right)\ \left(1 + \text{lamb}^{2}\ \text{capkmp[en]}^{2}\right)}\Biggr) +$$

$$\mathtt{phip[en]^{j}\ rho2p[en]}\ \frac{\mathtt{1}}{\mathtt{16\ lamb^{6}\ kp[en]^{2}\ k[en]^{4}}}$$

$$\Bigg(\mathtt{3\ lamb^{2}}\ \big(\mathtt{capkpp[en]^{2}-capkmp[en]^{2}}\big)\ -\ \mathtt{lamb^{4}}\ \big(\mathtt{capkpp[en]^{4}-capkmp[en]^{4}}\big)\ +$$

$$\frac{\mathtt{1}}{\mathtt{3}}\ \mathtt{lamb^{6}}\ \big(\mathtt{capkpp[en]^{6}-capkmp[en]^{6}}\big)\ -\ \mathtt{4\ Log}\Big[\frac{\mathtt{1+lamb^{2}\ capkpp[en]^{2}}}{\mathtt{1+lamb^{2}\ capkmp[en]^{2}}}\Big]\ +$$

$$\frac{\mathtt{4\ lamb^{2}\ kp[en]\ k[en]}}{\big(\mathtt{1+lamb^{2}\ capkpp[en]^{2}}\big)\ \big(\mathtt{1+lamb^{2}\ capkmp[en]^{2}}\big)}\Bigg);$$

$$\mathtt{capvm[en\_]}\ =\ \frac{\mathtt{1}}{\mathtt{2}}\ \Bigg(\mathtt{phi[en]^{j}}-\frac{\mathtt{km[en]^{2}+k[en]^{2}}}{\mathtt{2\ k[en]^{2}}}\ \mathtt{phim[en]^{j}}\Bigg)$$

$$\Bigg(\mathtt{rho0m[en]+rho1m[en]}\ \frac{\mathtt{km[en]^{2}+k[en]^{2}}}{\mathtt{2\ k[en]\ km[en]}}+\mathtt{rho2m[en]}\ \Bigg(\frac{\mathtt{km[en]^{2}+k[en]^{2}}}{\mathtt{2\ k[en]\ km[en]}}\Bigg)^{2}\Bigg)$$

$$\Bigg(\mathtt{Log}\Big[\frac{\mathtt{1+lamb^{2}\ capkpm[en]^{2}}}{\mathtt{1+lamb^{2}\ capkmm[en]^{2}}}\Big]-\frac{\mathtt{4\ lamb^{2}\ km[en]\ k[en]}}{\big(\mathtt{1+lamb^{2}\ capkpm[en]^{2}}\big)\ \big(\mathtt{1+lamb^{2}\ capkmm[en]^{2}}\big)}\Bigg)\ +$$

$$\Bigg(-\Bigg(\mathtt{phi[en]^{j}}-\frac{\mathtt{km[en]^{2}+k[en]^{2}}}{\mathtt{2\ k[en]^{2}}}\ \mathtt{phim[en]^{j}}\Bigg)\ \Bigg(\mathtt{rho1m[en]}\ \frac{\mathtt{1}}{\mathtt{4\ lamb^{2}\ km[en]\ k[en]}}\ +$$

$$\mathtt{rho2m[en]}\ \frac{\mathtt{km[en]^{2}+k[en]^{2}}}{\mathtt{4\ lamb^{2}\ km[en]^{2}\ k[en]^{2}}}\Bigg)\ +\ \mathtt{phim[en]^{j}}\ \frac{\mathtt{1}}{\mathtt{4\ lamb^{2}\ k[en]^{2}}}$$

$$\Bigg(\mathtt{rho0m[en]+rho1m[en]}\ \frac{\mathtt{km[en]^{2}+k[en]^{2}}}{\mathtt{2\ k[en]\ km[en]}}+\mathtt{rho2m[en]}\ \Bigg(\frac{\mathtt{km[en]^{2}+k[en]^{2}}}{\mathtt{2\ k[en]\ km[en]}}\Bigg)^{2}\Bigg)\Bigg)$$

$$\Bigg(\mathtt{4\ lamb^{2}\ km[en]\ k[en]-2\ Log}\Big[\frac{\mathtt{1+lamb^{2}\ capkpm[en]^{2}}}{\mathtt{1+lamb^{2}\ capkmm[en]^{2}}}\Big]\ +$$

$$\frac{\mathtt{4\ lamb^{2}\ km[en]\ k[en]}}{\big(\mathtt{1+lamb^{2}\ capkpm[en]^{2}}\big)\ \big(\mathtt{1+lamb^{2}\ capkmm[en]^{2}}\big)}\Bigg)\ +\ \Bigg(\mathtt{rho2m[en]}$$

$$\frac{\mathtt{1}}{\mathtt{8\ lamb^{4}\ km[en]^{2}\ k[en]^{2}}}\ \Bigg(\mathtt{phi[en]^{j}}-\frac{\mathtt{km[en]^{2}+k[en]^{2}}}{\mathtt{2\ k[en]^{2}}}\ \mathtt{phim[en]^{j}}\Bigg)\ -\ \mathtt{phim[en]^{j}}$$

$$\Bigg(\mathtt{rho1m[en]}\ \frac{\mathtt{1}}{\mathtt{8\ lamb^{4}\ km[en]\ k[en]^{3}}}+\mathtt{rho2m[en]}\ \frac{\mathtt{km[en]^{2}+k[en]^{2}}}{\mathtt{8\ lamb^{4}\ km[en]^{2}\ k[en]^{4}}}\Bigg)\Bigg)$$

$$\Bigg(\mathtt{4\ lamb^{4}\ k[en]\ km[en]}\ \big(\mathtt{km[en]^{2}+k[en]^{2}}\big)-\mathtt{8\ lamb^{2}\ k[en]\ km[en]\ +\ 3\ Log}\Big[$$

$$\frac{\mathtt{1+lamb^{2}\ capkpm[en]^{2}}}{\mathtt{1+lamb^{2}\ capkmm[en]^{2}}}\Big]\ -\ \frac{\mathtt{4\ lamb^{2}\ km[en]\ k[en]}}{\big(\mathtt{1+lamb^{2}\ capkpm[en]^{2}}\big)\ \big(\mathtt{1+lamb^{2}\ capkmm[en]^{2}}\big)}\Bigg)\ +$$

$$\mathtt{phim[en]^{j}\ rho2m[en]}\ \frac{\mathtt{1}}{\mathtt{16\ lamb^{6}\ km[en]^{2}\ k[en]^{4}}}$$

```
      (3 lamb^2 (capkpm[en]^2 - capkmm[en]^2) - lamb^4 (capkpm[en]^4 - capkmm[en]^4) +

        1                                            1 + lamb^2 capkpm[en]^2
        - lamb^6 (capkpm[en]^6 - capkmm[en]^6) - 4 Log[-----------------------] +
        3                                            1 + lamb^2 capkmm[en]^2

                     4 lamb^2 km[en] k[en]
        ----------------------------------------------------- );
        (1 + lamb^2 capkpm[en]^2) (1 + lamb^2 capkmm[en]^2)


    (*  I'm using op phonon
     energies instead of freqs. so extra hbar in denom *)
                           e^2 elo           1        1
    opfunc[en_] = ----------------------- (------- - -------) (mstarp[en] f0p[en]
                  hbar^3 f0[en] k[en]      epsinf    epsnot
         capvp[en] (nq + 1) + mstarm[en] f0m[en] capvm[en] nq UnitStep[en - elo]);

    capl[en_] =
     mstar[en]                             accon      picon      coulcon
     --------- (opcon opfunc[en] + phi[en]^j (-------  + -------- + ----------));
         e                                 tac[en]    tpie[en]   tcoul[en]
    dd[iloop, jloop] = NIntegrate[-df0[en] phi[en]^i capl[en] k[en]^3,
      {en, Abs[efermi / 2000], uplim kt}];
    dd[jloop, iloop] = dd[iloop, jloop];
   ];
  ];

  beta0 = NIntegrate[-df0[en] k[en]^3, {en, Abs[efermi / 2000], uplim kt}];
  beta1 = NIntegrate[-df0[en] phi[en] k[en]^3, {en, Abs[efermi / 2000], uplim kt}];
  beta2 = NIntegrate[-df0[en] phi[en]^2 k[en]^3, {en, Abs[efermi / 2000], uplim kt}];
  dd33[1, 1] = 0;
  dd33[1, 2] = beta0;
  dd33[1, 3] = beta1;
  dd33[1, 4] = beta2;
  dd33[2, 1] = beta0;
  dd33[2, 2] = dd[1, 1];
  dd33[2, 3] = dd[1, 2];
  dd33[2, 4] = dd[1, 3];
  dd33[3, 1] = beta1;
  dd33[3, 2] = dd[2, 1];
  dd33[3, 3] = dd[2, 2];
  dd33[3, 4] = dd[2, 3];
  dd33[4, 1] = beta2;
  dd33[4, 2] = dd[3, 1];
  dd33[4, 3] = dd[3, 2];
  dd33[4, 4] = dd[3, 3];
  d33 = Array[dd33, {4, 4}];
  d = Array[dd, {3, 3}];
  detd33 = Det[d33];
  detd = Det[d];
```

```
              -e   detd33
   sigma = ─────── ──────;
             3 Pi^2  detd
         sigma
   mu = ──────;
          e n
               mu
   muconv  = ────;
              300
   Write[diskette, kcomp, "\t" , NumberForm[n,
     NumberFormat -> (SequenceForm[#1, "e", #3] &)], "\t" , Re[muconv]];
   Print["temp  :  ", temp, "   Conc  :  ", n, "   Mob  :  ", Re[muconv]];

  ];
  (*  end of temperature loop  *)


  Close[diskette];
 ];]

(*  end of scattering mechanism loop  *)
```

```
temp : 300   Conc : 1. × 10^19   Mob : 24.0531
$Aborted
```

Bring all of the exported files together in to a large arrage of (x, y, z)

```
SetDirectory["/Users/detert/Dropbox/Research/Conc calc/mobility300/"];
fileNames = FileNames["*.txt"];
```

```
allFiles =
  Table[Import[FindFile[fileNames[[i]]], "TSV"], {i, 1, Length[fileNames]}];
```

```
Dimensions[allFiles]
```

```
{101, 31, 3}
```

```
allFilesFlat = Flatten[allFiles, 1];
Dimensions[allFilesFlat]
```

```
{3131, 3}
```

```
Export["/Users/detert/Dropbox/Research/Conc
    calc/mobility300/Combined/mobility300flat.txt", allFilesFlat, "TSV"];
```

Native defects and doping calculations

Mobility vs Compensation vs Concentration Import

```
Tmeas = 300.;(*Measurement temp, K *)
If[Tmeas == 300.,
  SetDirectory[
   "/Users/detert/Dropbox/Research/Conc
     calc/Mobility_raw_data/Compmobilitydata300/"],
  SetDirectory[
   "/Users/detert/Dropbox/Research/Conc
     calc/Mobility_raw_data/Compmobilitydata77/"]];
fileNames = FileNames["*.txt"];
allFiles  = Table[Import[FindFile[fileNames[[i]]], "TSV"],
    {i, 1, Length[fileNames]}];
allFilesFlat = Flatten[allFiles, 1];
cdomobiltyinterp = Interpolation[allFilesFlat];
cdomobiltyinterp[0.5, 4*^19];
(*check typical as-grown CdO value*)
Export["combined/allFilesFlat.txt", allFilesFlat];
```

Calculation (looped)

```
directory =
  "/Users/detert/Dropbox/Research/Conc calc/Doping
    Calculation Loops/loops/efs/";
SetDirectory[directory];
loopp = "EFS";
looptable = {};
For[dd = 0, dd ≤ 10, dd++;
 charge  = 1.6 × 10^-19;
 c  =  2.997 × 10^8; (*cgs units*)
 hbar = 6.58 × 10^-16 (*eVs*);
 masse = 9.109 × 10^-28 (*g*);
 chargeerg = 4.8 × 10^-10 (*charge on electron in ergs*);
 eVerg = 1.602 × 10^-12; (*converts ev to erg.*)
 hbar =  1.0546 × 10^-27 (* erg-s *);
 kbeV = 8.617 × 10^-5; (*Boltzmann constant,eV/K*)
 kb = 1.38 × 10^-16; (*Boltzmann constant,erg/K*)
 Anneal = False; (*determines whether to use growth or
  anneal temp in defect formation equations*)
 Tgrowth = 273. + 270.; (* growth temp in K *)
 Tanneal = 273. + 500.; (*anneal temp in K*)
 EFS = 0.1 + 0.1 dd; (*Energy of EFS relative to c.b. minimum
  for CdO*)
 mc = .23; (*conduction band effective mass, CdO*)
 Eg = 2.3; (*band gap, eV*)
```

```
cdodensity = 8.150 * (0.5 (112.41 + 16. ))^-1 6.02214179`*^23;
nsites = cdodensity/2.;
enFormationInitialVal = 1;
(*dopeactivenergy=2;
(*dopant deactivation energy in eV*)
dopeprefactor=1;(*uniform dopant deactivation at all
 dopant concentrations, non-equilibrium growth?*)*)
nbackgroundacceptors = 0;
tempdefect = If[Anneal == True, Tanneal, Tgrowth];
subs = {eFermi → eff, enFormationInit → enFormationInitialVal};
(*common substituions that will get used a lot*)
(*dopantactivationfunc=dopeprefactor(1+Exp[(eFermi-dopeactiv)/(kbeV tempdefect)])^-1;*)
dopantactivationfunc = 1;
ndopants = 1./dopantactivationfunc
  (n - 2. ndonordefects + 2. nacceptordefects +
    nbackgroundacceptors);
(*will plot Ndopants vs n eventually,
so this arrangement is easier to use*)
enFormationDonor = enFormationInit - 2 (EFS - eFermi);
enFormationAcceptor = enFormationInit + 2 (EFS - eFermi);
(*formation energy as a function of Fermi level. Fermi
 level relative to c.b. minimum*)
ndonordefects = nsites Exp[-enFormationDonor/(kbeV tempdefect)];
nacceptordefects = nsites Exp[-enFormationAcceptor/(kbeV tempdefect)];
kdisp[z_] :=
 Sqrt[(Eg eVerg masse)/hbar^2 + ((Eg eVerg masse)/(hbar^2 mc)) + ((2. kb masse Tmeas z)/hbar^2) -
   1./(hbar^4 mc)
    Sqrt[Eg eVerg hbar^4 masse^2
      (Eg eVerg + 2. Eg eVerg mc + Eg eVerg mc^2 + 4. kb mc Tmeas z)]];
(*z is reduced energy*)
nconc[k_] := 1/(3. Pi^2) k^3 (*simplified case,
good for degenerately doped cases,
otherwise need integral form*);
```

Doped concentration export loop efs w mob.nb | **3**

```
ef = eFermi /. Solve[n == nconc[kdisp[eFermi/(kbeV Tmeas)]], eFermi];
(*Find Fermi energy as function of n*)
eff = ef[[2]]; (*Second root is positive solution*)
comptable = Table[{
   ndopants /. subs,
   n,
   ndonordefects /. subs,
   nacceptordefects /. subs}, {n, 1. * 10^19, 1. * 10^22, 5.*^17}];
curvedata = Table[{comptable[[i, 1]], comptable[[i, 2]]},
  {i, Length[comptable]}];
invcurvedata = Table[{curvedata[[i, 2]], curvedata[[i, 1]]},
  {i, Length[curvedata]}];
invcurve = Interpolation[invcurvedata];
donorsconc = Table[{comptable[[i, 1]], comptable[[i, 3]]},
  {i, Length[comptable]}];
acceptorsconc = Table[{comptable[[i, 1]], comptable[[i, 4]]},
  {i, Length[comptable]}];
(*Compute compensation as a function of *dopant*
 concentration N_D*);
comptablend =
 Table[{comptable[[i, 1]],
    (comptable[[i, 1]] + 4 comptable[[i, 3]] + 4 comptable[[i, 4]] +
       nbackgroundacceptors - comptable[[i, 2]]) /
     (comptable[[i, 1]] + 4 comptable[[i, 3]] + 4 comptable[[i, 4]] +
       nbackgroundacceptors + comptable[[i, 2]])},
  {i, Length[comptable]}];
(*Compute compensation as a function of *electron*
 concentration n for use in Leon's calculation*);
comptablen =
 Table[{comptable[[i, 2]],
    (comptable[[i, 1]] + 4 comptable[[i, 3]] + 4 comptable[[i, 4]] +
       nbackgroundacceptors - comptable[[i, 2]]) /
     (comptable[[i, 1]] + 4 comptable[[i, 3]] + 4 comptable[[i, 4]] +
       nbackgroundacceptors + comptable[[i, 2]])},
  {i, Length[comptable]}];
AppendTo[looptable, {dd, EFS}];
Export["conc/" <> "conc_" <> loopp <> IntegerString[dd, 10, 2] <>
  ".txt", curvedata, "TSV"];
Export["defects/" <> "nd_" <> loopp <> IntegerString[dd, 10, 2] <>
  ".txt", donorsconc, "TSV"];
Export["defects/" <> "na_" <> loopp <> IntegerString[dd, 10, 2] <>
  ".txt", acceptorsconc, "TSV"];
Export["comp_nd/" <> "comp_nd_" <> loopp <>
  IntegerString[dd, 10, 2] <> ".txt", comptablend, "TSV"];
Export["comp_n/" <> "comp_n_" <> loopp <> IntegerString[dd, 10, 2] <>
```

Printed by Wolfram Mathematica Student Edition

```
    ".txt", comptablen, "TSV"];
  Print[dd, ",", EFS](*check progress*);

  (*Mobility*)
  Quiet[
   mobvsn =
    Table[{comptablen[[i, 1]],
      cdomobiltyinterp[comptablen[[i, 2]], comptablen[[i, 1]]]},
     {i, Length[comptablen]}]];
  Quiet[mobvsnd = Table[{invcurve[mobvsn[[i, 1]]], mobvsn[[i, 2]]},
     {i, Length[mobvsn]}]];
  Export["mob_n/" <> "mob_n_" <> loopp <> IntegerString[dd, 10, 2] <>
    ".txt", mobvsn, "TSV"];
  Export["mob_nd/" <> "mob_nd_" <> loopp <> IntegerString[dd, 10, 2] <>
    ".txt", mobvsnd, "TSV"];
 ]
stats = Join[looptable,
    {{"Loop", loopp},
     {"EFS:", "loop"},
     {"Dopant Activation", dopantactivationfunc},
     {"Formation Energy at EFS:", enFormationInitialVal},
     {"Background accept conc", nbackgroundacceptors},
     {"T:", Tmeas "K"},
     {"Tgrowth:", Tgrowth "K"},
     {"Annealing:", If[Anneal ⩵ True, Tanneal "K", "No"]}}];
Export["stats/stats.txt", stats, "TSV"];
```

Bibliography

[1] M. C. Tamargo. *II-VI semiconductor materials and their applications.* Vol. 12. CRC Press, 2002.

[2] S. Nakamura, S. Pearton, and G. Fasol. *The blue laser diode: the complete story.* Springer, 2000.

[3] P. Norton. "HgCdTe infrared detectors". *Optoelectronics review* 10 (2002), pp. 159–174.

[4] H. Morkoç et al. "Large-band-gap SiC, III-V nitride, and II-VI ZnSe-based semiconductor device technologies". *Journal of Applied Physics* 76 (1994), pp. 1363–1398.

[5] M. Afzaal and P. O'Brien. "Recent developments in II-VI and III-VI semiconductors and their applications in solar cells". *Journal of Materials Chemistry* 16 (17 2006), pp. 1597–1602.

[6] H. Morkoç and Ü. Özgür. *Zinc Oxide: Fundamentals, Materials and Device Technology.* Weinheim: John Wiley & Sons, 2008, p. 500.

[7] Ü. Özgür et al. "A comprehensive review of ZnO materials and devices". *Journal of Applied Physics* 98 (2005), pp. 041301–041301.

[8] A. Janotti and C. G. Van de Walle. "Fundamentals of zinc oxide as a semiconductor". *Reports on Progress in Physics* 72 (2009), p. 126501.

[9] E. Fortunato, P. Barquinha, and R. Martins. "Oxide semiconductor thin-film transistors: a review of recent advances". *Advanced Materials* 24 (2012), pp. 2945–86.

[10] D. Scaife. "Oxide semiconductors in photoelectrochemical conversion of solar energy". *Solar Energy* 25 (1980), pp. 41–54.

[11] R. G. Gordon. "Criteria for choosing transparent conductors". *MRS Bulletin* 25 (2000), pp. 52–57.

[12] C. G. Granqvist. "Transparent conductors as solar energy materials: A panoramic review". *Solar Energy Materials and Solar Cells* 91 (2007), pp. 1529–1598.

[13] E. Fortunato et al. "Transparent conducting oxides for photovoltaics". *MRS bulletin* 32 (2007), pp. 242–247.

[14] D. S. Ginley and J. D. Perkins. “Transparent Conductors”. In: *Handbook of Transparent Conductors*. Ed. by D. S. Ginley, H. Hosono, and D. C. Paine. Boston, MA: Springer US, 2010. Chap. Transparent Conductors, pp. 1–25.

[15] M. Grundmann. *The Physics of Semiconductors*. 2nd ed. Graduate Texts in Physics. Springer-Verlag Berlin Heidelberg, 2010.

[16] D. S. Ghosh, T. L. Chen, and V. Pruneri. “High figure-of-merit ultrathin metal transparent electrodes incorporating a conductive grid”. *Applied Physics Letters* 96 (2010), p. 041109.

[17] H. Wu et al. “Electrospun metal nanofiber webs as high-performance transparent electrode.” *Nano Letters* 10 (2010), pp. 4242–8.

[18] J. Robertson and B. Falabretti. “Electronic Structure of Transparent Conducting Oxides”. In: *Handbook of Transparent Conductors*. Ed. by D. S. Ginley, H. Hosono, and D. C. Paine. Boston, MA: Springer US, 2010, pp. 27–50.

[19] K. M. Yu et al. “Ideal transparent conductors for full spectrum photovoltaics”. *Journal of Applied Physics* 111 (2012), pp. 123505–123505.

[20] A. Burgers. “How to design optimal metallization patterns for solar cells”. *Progress in Photovoltaics Research and Applications* 7 (1999), pp. 457–461.

[21] S. Calnan and A. N. Tiwari. “High mobility transparent conducting oxides for thin film solar cells”. *Thin Solid Films* 518 (2010), pp. 1839–1849.

[22] X.-Y. Zeng et al. “A new transparent conductor: silver nanowire film buried at the surface of a transparent polymer”. *Advanced Materials* 22 (2010), pp. 4484–8.

[23] Y. C. Jung et al. “Robust, Conducting, and Transparent Polymer Composites Using Surface-Modified and Individualized Double-Walled Carbon Nanotubes”. *Advanced Materials* 20 (2008), pp. 4509–4512.

[24] F. Bonaccorso et al. “Graphene photonics and optoelectronics”. *Nature Photonics* 4 (2010), pp. 611–622.

[25] Z. Wu et al. “Transparent, Conductive Carbon Nanotube Films”. *Science* 305 (2004), pp. 1273–1276.

[26] H. Kawazoe et al. “P-type electrical conduction in transparent thin films of CuAlO2”. *Nature* 389 (1997), pp. 939–942.

[27] H. Sato et al. “Transparent conducting p-type NiO thin films prepared by magnetron sputtering”. *Thin Solid Films* 236 (1993), pp. 27–31.

[28] A. Janotti et al. “Controlling the Conductivity in Oxide Semiconductors”. In: *Functional Metal Oxide Nanostructures*. Ed. by J. Wu et al. Springer, 2012, pp. 23–35.

[29] K. Seeger. *Semiconductor Physics: An Introduction*. Springer, 2004.

[30] A. Tsukazaki, A. Ohtomo, and M. Kawasaki. “High-mobility electronic transport in ZnO thin films”. *Applied Physics Letters* 88 (2006), pp. 152106–152106.

[31] P. D. C. King and T. D. Veal. “Conductivity in transparent oxide semiconductors”. *Journal of Physics: Condensed Matter* 23 (2011), p. 334214.

[32] J. Y. Seto. “The electrical properties of polycrystalline silicon films”. *Journal of Applied Physics* 46 (2008), pp. 5247–5254.

[33] D. C. Paine, B. Yaglioglu, and J. Berry. “Characterization of TCO Materials”. In: *Handbook of Transparent Conductors*. Ed. by D. S. Ginley, H. Hosono, and D. C. Paine. Boston, MA: Springer US, 2010, pp. 111–148.

[34] M. Chen et al. “Intrinsic limit of electrical properties of transparent conductive oxide films”. *Journal of Physics D: Applied Physics* 33 (2000), p. 2538.

[35] K. Ellmer and R. Mientus. “Carrier transport in polycrystalline ITO and ZnO:Al II: The influence of grain barriers and boundaries”. *Thin Solid Films* 516 (2008), pp. 5829–5835.

[36] K. Ellmer and R. Mientus. “Carrier transport in polycrystalline transparent conductive oxides: A comparative study of zinc oxide and indium oxide”. *Thin Solid Films* 516 (2008), pp. 4620–4627.

[37] B. J. Ingram et al. “Chemical and Structural Factors Governing Transparent Conductivity in Oxides”. 13 (2004), pp. 167–175.

[38] R. Shannon, J. Gillson, and R. Bouchard. “Single crystal synthesis and electrical properties of $CdSnO_3$, Cd_2SnO_4, In_2TeO_6 and $Cdln_2O_4$”. *Journal of Physics and Chemistry of Solids* 38 (1977), pp. 877–881.

[39] T. Mason et al. “Defect chemistry and physical properties of transparent conducting oxides in the CdO-In_2O_3-SnO_2 system”. *Thin Solid Films* 411 (2002), pp. 106–114.

[40] T. Minami. “Transparent conducting oxide semiconductors for transparent electrodes”. *Semiconductor Science and Technology* 20 (2005), S35–S44.

[41] M. Yan et al. “Highly conductive epitaxial CdO thin films prepared by pulsed laser deposition”. *Applied Physics Letters* 78 (2001), p. 2342.

[42] Y. Yang et al. “CdO as the archetypical transparent conducting oxide. Systematics of dopant ionic radius and electronic structure effects on charge transport and band structure”. *Journal of American Chemical Society* 127 (2005), pp. 8796–804.

[43] S. Jin et al. “Tuning the properties of transparent oxide conductors. Dopant ion size and electronic structure effects on CdO-based transparent conducting oxides. Ga-and In-doped CdO thin films grown by MOCVD”. *Chemistry of Materials* 20 (2007), pp. 220–230.

[44] P. Ghosh, R. Maity, and K. K. Chattopadhyay. “Electrical and optical properties of highly conducting CdO:F thin film deposited by sol-gel dip coating technique”. *Solar Energy Materials and Solar Cells* 81 (2004), pp. 279–289.

[45] D. S. Ginley and C. Bright. “Transparent Conducting Oxides”. *MRS Bulletin* 25 (08 2000), pp. 15–18.

[46] M. D. McCluskey, M. C. Tarun, and S. T. Teklemichael. “Hydrogen in oxide semiconductors”. *Journal of Materials Research* 27 (2012), pp. 2190–2198.

[47] A. Janotti, D. Segev, and C. G. Van de Walle. “Effects of cation d states on the structural and electronic properties of III-nitride and II-oxide wide-band-gap semiconductors”. *Physical Review B* 74 (2006), p. 045202.

[48] E. Burstein. “Anomalous optical absorption limit in InSb”. *Physical Review* 93 (1954), p. 632.

[49] T. Moss. “The interpretation of the properties of indium antimonide”. *Proceedings of the Physical Society. Section B* 67 (1954), p. 775.

[50] W. Walukiewicz. “Carrier scattering by native defects in heavily doped semiconductors”. *Physical Review B* 41 (1990), p. 10218.

[51] D. T. Speaks et al. “Fermi level stabilization energy in cadmium oxide”. *Journal of Applied Physics* 107 (2010), pp. 113706–113706.

[52] K.-F. Berggren and B. E. Sernelius. “Band-gap narrowing in heavily doped many-valley semiconductors”. *Physical Review B* 24 (1981), p. 1971.

[53] A. Walsh, J. L. F. Da Silva, and S.-H. Wei. “Origins of band-gap renormalization in degenerately doped semiconductors”. *Physical Review B* 78 (7 2008), p. 075211.

[54] T. Pisarkiewicz and A. Kolodziej. “Nonparabolicity of the Conduction Band Structure in Degenerate Tin Dioxide”. *physica status solidi (b)* 158 (1990), K5–K8.

[55] T. J. Coutts, D. L. Young, and T. A. Gessert. “Modeling, Characterization, and Properties of Transparent Conducting Oxides”. In: *Handbook of Transparent Conductors.* Ed. by D. S. Ginley, H. Hosono, and D. C. Paine. Boston, MA: Springer US, 2010, pp. 51–110.

[56] I. Hamberg and C. G. Granqvist. “Evaporated Sn-doped In_2O_3 films: basic optical properties and applications to energy-efficient windows”. *Journal of Applied Physics* 60 (1986), R123–R160.

[57] R. J. Mendelsberg, Y. Zhu, and A. Anders. “Determining the nonparabolicity factor of the CdO conduction band using indium doping and the Drude theory”. *Journal of Physics D: Applied Physics* 45 (2012), p. 425302.

[58] E. D. Palik. *Handbook of Optical Constants of Solids.* Vol. 3. Academic press, 1998.

[59] W. Walukiewicz et al. “Electron mobility and free-carrier absorption in GaAs: Determination of the compensation ratio”. *Journal of Applied Physics* 50 (1979), pp. 899–908.

[60] E. Haga and H. Kimura. “Free-Carrier Infrared Absorption in III-V Semiconductors III. GaAs, InP, GaP and GaSb”. *Journal of the Physical Society of Japan* 19 (1964), pp. 658–669.

[61] H. Peelaers, E. Kioupakis, and C. G. Van de Walle. “Fundamental limits on optical transparency of transparent conducting oxides: Free-carrier absorption in SnO_2”. *Applied Physics Letters* 100 (2012), p. 011914.

[62] K. Badeker. “Concerning the electricity conductibility and the thermoelectric energy of several heavy metal bonds”. *Annalen der Physik* 22 (1907), pp. 749–766.

[63] M. Burbano, D. O. Scanlon, and G. W. Watson. “Sources of conductivity and doping limits in CdO from hybrid density functional theory”. *Journal of the American Chemical Society* 113 (2011), p. 15065.

[64] S. K. . K. Vasheghani Farahani et al. “Electron mobility in CdO films”. *Journal of Applied Physics* 109 (2011), p. 073712.

[65] W. Walukiewicz. “Mechanism of Fermi-level stabilization in semiconductors”. *Physical Review B* 37 (1988), p. 4760.

[66] W. Walukiewicz. “Amphoteric native defects in semiconductors”. *Applied Physics Letters* 54 (1989), pp. 2094–2096.

[67] W. Walukiewicz. “Intrinsic limitations to the doping of wide-gap semiconductors”. *Physica B: Condensed Matter* 302 (2001), pp. 123–134.

[68] P. King et al. “Unification of the electrical behavior of defects, impurities, and surface states in semiconductors: Virtual gap states in CdO”. *Physical Review B* 79 (2009).

[69] K. Wang et al. “Mg doped InN and confirmation of free holes in InN”. *Applied Physics Letters* 98 (2011), p. 042104.

[70] N. Miller et al. “Hole transport and photoluminescence in Mg-doped InN”. *Journal of Applied Physics* 107 (2010), p. 113712.

[71] R. E. Jones et al. “Evidence for p-Type Doping of InN”. *Physical Review Letters* 96 (12 2006), p. 125505.

[72] L. Piper et al. “Observation of quantized subband states and evidence for surface electron accumulation in CdO from angle-resolved photoemission spectroscopy”. *Physical Review B* 78 (2008).

[73] P. D. C. King et al. “Surface band-gap narrowing in quantized electron accumulation layers”. *Physical Review Letters* 104 (2010), p. 256803.

[74] L. F. J. Piper et al. “Origin of the n-type conductivity of InN: The role of positively charged dislocations”. *Applied Physics Letters* 88 (2006), pp. 252109–252109.

[75] C. G. Van de Walle and J. Neugebauer. “Universal alignment of hydrogen levels in semiconductors, insulators and solutions”. *Nature* 423 (2003), pp. 626–628.

[76] K. Maschke and U. Rössler. “The Electronic Structure of CdO I. The Energy-Band Structure (APW Method)”. *physica status solidi (b)* 28 (1968), pp. 577–581.

[77] C. McGuinness et al. "Influence of shallow core-level hybridization on the electronic structure of post-transition-metal oxides studied using soft X-ray emission and absorption". *Physical Review B* 68 (2003), p. 165104.

[78] J. E. Jaffe, R. Pandey, and A. B. Kunz. "Electronic structure of the rocksalt-structure semiconductors ZnO and CdO". *Physical Review B* 43 (1991), p. 14030.

[79] S.-H. Wei and A. Zunger. "Calculated natural band offsets of all II–VI and III–V semiconductors: Chemical trends and the role of cation d orbitals". *Applied Physics Letters* 72 (1998), p. 2011.

[80] L. Piper et al. "Electronic structure of single-crystal rocksalt CdO studied by soft X-ray spectroscopies and ab initio calculations". *Physical Review B* 77 (2008), p. 125204.

[81] A. Schleife et al. "First-principles study of ground- and excited-state properties of MgO, ZnO, and CdO polymorphs". *Physical Review B* 73 (24 2006), p. 245212.

[82] Y. Dou et al. "An experimental and theoretical investigation of the electronic structure of CdO". *Journal of Physics: Condensed Matter* 10 (1998), p. 8447.

[83] I. N. Demchenko et al. "Electronic structure of CdO studied by soft X-ray spectroscopy". *Journal of Electron Spectroscopy and Related Phenomena* 184 (2011), pp. 249–253.

[84] S. K. Vasheghani Farahani et al. "Temperature dependence of the direct bandgap and transport properties of CdO". *Applied Physics Letters* 102 (2013), pp. 022102–022102.

[85] J. G. Lu et al. "Carrier concentration dependence of band gap shift in n-type ZnO:Al films". *Journal of Applied Physics* 101 (2007), p. 083705.

[86] A. V. Singh et al. "Doping mechanism in aluminum doped zinc oxide films". *Journal of Applied Physics* 95 (2004), pp. 3640–3643.

[87] P. H. Jefferson et al. "Bandgap and effective mass of epitaxial cadmium oxide". *Applied Physics Letters* 92 (2008), pp. 022101–022101.

[88] W. A. Harrison. "Elementary theory of heterojunctions". *Journal of Vacuum Science and Technology* 14 (1977), pp. 1016–1021.

[89] T. D. Veal, P. D. C. King, and C. F. McConville. "Electronic Properties of Post-transition Metal Oxide Semiconductor Surfaces". In: *Functional Metal Oxide Nanostructures.* Ed. by J. Wu et al. Springer Series in Materials Science. Springer, 2012, pp. 127–145.

[90] C. Vesely and D. Langer. "Electronic Core Levels of the II B-VI A Compounds". *Physical Review B* 4 (1971), p. 451.

[91] F. P. Koffyberg. "Electronic conduction and defect equilibria in CdO single crystals". *Journal of Solid State Chemistry* 2 (1970), pp. 176–181.

[92] F. A. Benko and F. P. Koffyberg. "Quantum efficiency and optical transitions of CdO photoanodes". *Solid state communications* 57 (1986), pp. 901–903.

[93] N. Ueda et al. "Band-gap widening of CdO thin films". *Journal of Applied Physics* 84 (1998), pp. 6174–6177.

[94] Y. Zhu et al. "Structural, optical, and electrical properties of indium-doped cadmium oxide films prepared by pulsed filtered cathodic arc deposition". *Journal of Materials Science* 48 (2013), pp. 3789–3797.

[95] Y. Zhu et al. "Transparent and conductive indium doped cadmium oxide thin films prepared by pulsed filtered cathodic arc deposition". *Applied Surface Science* 265 (2013), pp. 738–744.

[96] A. Rockett. *The Materials Science of Semiconductors*. Springer, 2007.

[97] S. Adachi. *Properties of semiconductor alloys: group-IV, III-V and II-VI semiconductors*. Vol. 28. John Wiley & Sons, 2009.

[98] W. Walukiewicz et al. "Nitrogen-induced modification of the electronic structure of group III-N-V alloys". *Electrochemical Society Proceedings* 99-11 (1999), p. 190.

[99] J. Ishihara et al. "Growth and characterization of $Zn_{1-x}Cd_xO$ films using remote plasma MOCVD". *Applied Surface Science* 244 (2005), pp. 381–384.

[100] J. Ishihara et al. "$Zn_{1-x}Cd_xO$ systems with visible band gaps". *Applied Physics Letters* 89 (2006), p. 091914.

[101] G. Chen et al. "Material properties of $Cd_{1-x}Mg_xO$ alloys synthesized by radio frequency sputtering". *Applied Physics Letters* 103 (2013), pp. 041902–041902.

[102] M. A. Mayer et al. "Band Gap Engineering of Oxide Photoelectrodes: Characterization of $ZnO_{1-x}Se_x$". *The Journal of Physical Chemistry C* 116 (2012), p. 15281.

[103] M. Rohlfing et al. "Image States and Excitons at Insulator Surfaces with Negative Electron Affinity". *Physical Review Letters* 91 (25 2003), p. 256802.

[104] I.-S. Choi, Y.-J. Kim, and E.-G. Heo. "Characterization of Negative Electron Affinity for MgO Film by Ultraviolet Photoelectron Spectroscopy". In: *SID Symposium Digest of Technical Papers*. Vol. 41. Wiley Online Library. 2010, pp. 408–411.

[105] Y. F. Li et al. "Realization of p-type conduction in undoped $Mg_xZn_{1-x}O$ thin films by controlling Mg content". *Applied Physics Letters* 91, 232115 (2007), pages.

[106] Z. Wei et al. "Formation of p-type MgZnO by nitrogen doping". *Applied Physics Letters* 89 (2006), p. 102104.

[107] F. Atay et al. "Optical, structural and surface characterization of CdO:Mg films". *Journal of Materials Science: Materials in Electronics* 22 (2011), pp. 492–498.

[108] U. Paliwal, T. Bredow, and K. B. Joshi. "Structural properties of MgCdO alloys". In: *AIP Conference Proceedings*. Vol. 1447. 2012, p. 1037.

[109] Y.-S. Choi, C.-G. Lee, and S. M. Cho. “Transparent conducting $Zn_xCd_{1-x}O$ thin films prepared by the sol-gel process”. *Thin Solid Films* 289 (1996), pp. 153–158.

[110] T. Makino et al. “Band gap engineering based on MgZnO and CdZnO ternary alloy films”. *Applied Physics Letters* 78 (2001), p. 1237.

[111] S. Sadofev et al. “Visible band-gap ZnCdO heterostructures grown by molecular beam epitaxy”. *Applied Physics Letters* 89 (2006), p. 201907.

[112] X. J. Wang et al. “Band gap properties of ZnCdO alloys grown by molecular-beam epitaxy”. *Applied Physics Letters* 89 (2006), p. 151909.

[113] V. Venkatachalapathy et al. “Tuning light absorption by band gap engineering in ZnCdO as a function of MOVPE-synthesis conditions and annealing”. *Journal of Crystal Growth* 315 (2011), pp. 301–304.

[114] X. Ma et al. “Optical properties of sputtered hexagonal CdZnO films with band gap energies from 1.8 to 3.3 eV”. *Journal of Alloys and Compounds* 509 (2011), p. 6599.

[115] T. Makino et al. “Radiative and nonradiative recombination processes in lattice-matched (Cd,Zn)O/(Mg,Zn)O multiquantum wells”. *Applied Physics Letters* 77 (2000), pp. 1632–1634.

[116] A. V. Thompson et al. “Thermal stability of CdZnO/ZnO multi-quantum-wells”. *Applied Physics Letters* 91, 201921 (2007), p. 201921.

[117] D. W. Ma et al. “Sputtering deposited ternary $Zn_{1-x}Cd_xO$ crystal films on Si(111) substrates”. *Thin Solid Films* 461 (2004), p. 250.

[118] A. Schleife et al. “Ab initio description of heterostructural alloys: Thermodynamic and structural properties of $Mg_xZn_{1-x}O$ and $Cd_xZn_{1-x}O$”. *Physical Review B* 81 (2010).

[119] A. Schleife et al. “Electronic and optical properties of $Mg_xZn_{1-x}O$ and $Cd_xZn_{1-x}O$ from ab initio calculations”. *New Journal of Physics* 13 (2011), p. 085012.

[120] V. M. Fthenakis. “Life cycle impact analysis of cadmium in CdTe PV production”. *Renewable and Sustainable Energy Reviews* 8 (2004), pp. 303–334.

[121] V. M. Fthenakis. “End-of-life management and recycling of PV modules”. *Energy Policy* 28 (2000), pp. 1051–1058.

[122] N. McDonald and J. M. Pearce. “Producer responsibility and recycling solar photovoltaic modules”. *Energy Policy* 38 (2010), pp. 7041–7047.

[123] Y. Houari et al. “A system dynamics model of tellurium availability for CdTe PV”. *Progress in Photovoltaics: Research and Applications* 22 (2014), pp. 129–146.

[124] M. Lorenz et al. “Optical and electrical properties of epitaxial $(Mg,Cd)_xZn_{1-x}O$, ZnO, and ZnO:(Ga,Al) thin films on c-plane sapphire grown by pulsed laser deposition”. *Solid-State Electronics* 47 (2003), pp. 2205–2209.

[125] H. H.-C. Lai et al. “Electronic structure of ternary $Cd_xZn_{1-x}O$ ($\leq x \leq 0.075$) alloys”. *Applied Physics Letters* 100 (2012), p. 072106.

[126] Y. Tian et al. “Electrically pumped wavelength-tunable blue random lasing from CdZnO films on silicon”. *Applied Physics Letters* 100 (2012), pp. 231101–231101.

[127] Z. Ye et al. “Structural and photoluminescent properties of ternary $Zn_{1\text{-}x}Cd_xO$ crystal films grown on Si(111) substrates”. *Journal of Crystal Growth* 256 (2003), pp. 78–82.

[128] T. Gruber et al. “Optical and structural analysis of ZnCdO layers grown by metalorganic vapor-phase epitaxy”. *Applied Physics Letters* 83 (2003), p. 3290.

[129] K. Sakurai et al. “Spatial composition fluctuations in blue-luminescent ZnCdO semiconductor films grown by molecular beam epitaxy”. *Journal of Crystal Growth* 237 (2002), pp. 514–517.

[130] T. A. Edison. *Process of Duplicating Phonograms*. US Patent 484,582. 1892.

[131] B. K. Tay, Z. W. Zhao, and D. H. C. Chua. “Review of metal oxide films deposited by filtered cathodic vacuum arc technique”. *Materials Science and Engineering: R: Reports* 52 (2006), pp. 1–48.

[132] D. M. Sanders and A. Anders. “Review of cathodic arc deposition technology at the start of the new millennium”. *Surface and Coatings Technology* 133 (2000), pp. 78–90.

[133] A. Anders. *Cathodic arcs: From Fractal Spots to Energetic Condensation*. Springer, 2009.

[134] A. Anders et al. “Measurements of the total ion flux from vacuum arc cathode spots”. *IEEE Transactions on Plasma Science* 33 (2005), pp. 1532–1536.

[135] A. Anders, E. M. Oks, and G. Y. Yushkov. “Cathodic arcs: Fractal voltage and cohesive energy rule”. *Applied Physics Letters* 86 (2005), p. 211503.

[136] R. J. Mendelsberg et al. “Achieving high mobility ZnO:Al at very high growth rates by dc filtered cathodic arc deposition”. *Journal of Physics D: Applied Physics* 44 (2011), p. 232003.

[137] A. Anders, N. Pasaja, and S. Sansongsiri. “Filtered cathodic arc deposition with ion-species-selective bias”. *Review of Scientific Instruments* 78 (2007), pp. 063901–063901.

[138] A. Anders, R. A. MacGill, and T. A. McVeigh. “Efficient, compact power supply for repetitively pulsed, triggerless cathodic arcs”. *Review of Scientific Instruments* 70 (1999), pp. 4532–4535.

[139] A. Anders et al. “High quality ZnO: Al transparent conducting oxide films synthesized by pulsed filtered cathodic arc deposition”. *Thin Solid Films* 518 (2010), pp. 3313–3319.

[140] M. Mayer. “SIMNRA, a simulation program for the analysis of NRA, RBS and ERDA”. In: *AIP conference proceedings*. Vol. 475. 1999, p. 541.

[141] J. Colaux. *SIMTarget*. `http://webapps.fundp.ac.be/physique/simtarget/index.php`. Accessed: 04-17-2014.

[142] A. L. Patterson. “The Scherrer Formula for X-Ray Particle Size Determination”. *Physical Review* 56 (10 1939), pp. 978–982.

[143] L. Van der Pauw. “A method of measuring the resistivity and Hall coefficient on lamellae of arbitrary shape”. *Philips Technical Review* 20 (1958), pp. 220–224.

[144] J. I. Pankove. *Optical Processes in Semiconductors*. Courier Dover Publications, 2012.

[145] O. Heavens. *Optical Properties of Thin Solid Films*. Courier Dover Publications, 1991.

[146] A. Segura et al. “Current underestimation of the optical gap and Burstein-Moss shift in CdO thin films: A consequence of extended misuse of α^2-versus-$h\nu$ plots”. *Applied Physics Letters* 99 (2011), p. 151907.

[147] W. Walukiewicz et al. “Structure and electronic properties of InN and In-rich group III-nitride alloys”. *Journal of Physics D: Applied Physics* 39 (2006), R83–R99.

[148] R. E. Jones et al. “Band gap bowing parameter of $In_xAl_{1-x}N$”. *Journal of Applied Physics* 104 (2008), pp. 123501–123501.

[149] E. O. Kane. “Band structure of indium antimonide”. *Journal of Physics and Chemistry of Solids* 1 (1957), pp. 249–261.

[150] J. Wu and W. Walukiewicz. “Band gaps of InN and group III nitride alloys”. *Superlattices and Microstructures* 34 (2003), pp. 63–75.

[151] W. S. Baer. “Faraday rotation in ZnO: Determination of the electron effective mass”. *Physical Review* 154 (1967), p. 785.

[152] M. Yoshikawa et al. “Band-gap renormalization and band filling in Si-doped GaN films studied by photoluminescence spectroscopy”. *Journal of Applied Physics* 86 (1999), pp. 4400–4402.

[153] R. J. Guerrero-Moreno and N. Takeuchi. “First principles calculations of the ground-state properties and structural phase transformation in CdO”. *Physical Review B* 66 (2002), p. 205205.

[154] X. D. Zhang et al. “First-principles study of electronic and optical properties in wurtzite $Zn_{1-x}Cd_xO$”. *Journal of Applied Physics* 103 (2008), pp. 063721–063721.

[155] S. X. Li et al. “Fermi-level stabilization energy in group III nitrides”. *Physical Review B* 71 (2005), p. 161201.

[156] D. Briggs and M. P. Seah. *Practical surface analysis: by auger and X-ray photoelectron spectroscopy*. Wiley New York, 1983.

[157] M. Repoux. “Comparison of background removal methods for XPS”. *Surface and Interface Analysis* 18 (1992), pp. 567–570.

[158] P. King et al. “Valence-band electronic structure of CdO, ZnO, and MgO from X-ray photoemission spectroscopy and quasi-particle-corrected density-functional theory calculations”. *Physical Review B* 79 (2009), p. 205205.

[159] B. K. Agarwal et al. *X-ray Spectroscopy.* Vol. 2. Springer Berlin, 1979.

[160] D. Koningsberger and R. Prins. "X-ray absorption: principles, applications, techniques of EXAFS, SEXAFS, and XANES" (1988).

[161] A. Preston et al. "Band structure of ZnO from resonant x-ray emission spectroscopy". *Physical Review B* 78 (2008), p. 155114.

[162] Y. Zhu et al. "Electronic structure and phase stability of MgO, ZnO, CdO, and related ternary alloys". *Physical Review B* 77 (2008), p. 245209.

[163] A. Walsh et al. "Nature of the band gap of I_2O_3 revealed by first-principles calculations and X-ray spectroscopy". *Physical Review Letters* 100 (2008), p. 167402.

[164] R. van de Krol. "Principles of photoelectrochemical cells". In: *Photoelectrochemical Hydrogen Production.* Springer, 2012, pp. 13–67.

[165] T. Bak et al. "Photo-electrochemical hydrogen generation from water using solar energy. Materials-related aspects." *International Journal of Hydrogen Energy* 27 (2002), pp. 991–1022.

[166] J. Holladay et al. "An overview of hydrogen production technologies". *Catalysis Today* 139 (2009), pp. 244–260.

[167] J. W. Erisman et al. "How a century of ammonia synthesis changed the world". *Nature Geoscience* 1 (2008), pp. 636–639.

[168] L. Hsu and W. Walukiewicz. "Modeling of InGaN/Si tandem solar cells". *Journal of Applied Physics* 104, 024507 (2008), pages.

[169] M. Grätzel. "Photoelectrochemical cells". *Nature* 414 (2001), pp. 338–344.

[170] G. Brown et al. "Finite element simulations of compositionally graded InGaN solar cells". *Solar Energy Materials and Solar Cells* 94 (2010), pp. 478–483.

[171] W. Faschinger, S. Ferreira, and H. Sitter. "Doping limitations in wide gap II–VI compounds by Fermi level pinning". *Journal of Crystal Growth* 151 (1995), pp. 267–272.

[172] W. Faschinger. "Fundamental doping limits in wide gap II–VI compounds". *Journal of Crystal Growth* 159 (1996). Proceedings of the seventh international conference on II-VI compouds and devices, pp. 221–228.

[173] W. Szymańska and T. Dietl. "Electron scattering and transport phenomena in small-gap zinc-blende semiconductors". *Journal of Physics and Chemistry of Solids* 39 (1978), pp. 1025–1040.

[174] L. Hsu et al. "Electron mobility in InN and III-N alloys". *Journal of Applied Physics* 102 (2007), p. 073705.

[175] A. W. Metz et al. “Transparent conducting oxides: Texture and microstructure effects on charge carrier mobility in MOCVD-derived CdO thin films grown with a thermally stable, low-melting precursor”. *Journal of the American Chemical Society* 126 (2004), pp. 8477–8492.

[176] J. R. Tesmer et al. *Handbook of Modern Ion Beam Materials Analysis*. Materials Research Society Pittsburgh, PA, 1995.

[177] T. Makino et al. “Gallium concentration dependence of room-temperature near-band-edge luminescence in n-type ZnO:Ga”. *Applied Physics Letters* 85 (2004), p. 759.